

112

THE PRODUCTION OF BOSON RESONANCES OF  
ZERO HYPERCHARGE IN  $K^-$ -PROTON INTERACTIONS

by

Stanley Lionel Baker

A Thesis presented for the degree of Doctor of Philosophy  
of the University of London

Department of Physics,  
Imperial College of Science and Technology,  
London, S.W.7.

October, 1965

ABSTRACT

A study of the zero hypercharge boson resonances, produced in a hydrogen bubble chamber by the collisions of 3.5 Gev/c negative kaons with protons, is presented in this thesis. Most of the emphasis is on a comparison of the  $\omega$  and  $\phi$  meson production.

The consequences of SU(3) and SU(6) are discussed in chapter 1, where the mixing of the  $\omega$  and  $\phi$  is considered in some detail. A brief discussion of the single meson exchange model is also included in this chapter.

Chapters 2,3 and 4 are concerned with the techniques which were employed to obtain and analyse the bubble chamber photographs. Total cross sections are presented in chapter 5. The  $\rho^0$ ,  $\omega^0$  and  $\phi^0$  mesons are discussed in chapter 6, and the remaining non-strange boson resonances observed in the present experiment, in chapter 7.

In the final chapter various comparisons with the predictions of SU(3) are made and the striking differences between the  $\omega$  and  $\phi$  differential cross sections are discussed in detail.

CONTENTS

<u>Abstract</u>	page	2
<u>Preface</u>		6
<u>Chapter 1 - Symmetry Theories and the</u>		
<u>Zero Hypercharge Mesons</u>		7
1.1 Charge Independence and the Definition of Hypercharge		7
1.2 Consequences of SU(2) Invariance for Pions and Nucleons		9
1.3 The Development of SU(3)		12
1.4 Experimental Consequences of SU(3)		16
1.5 Peripheral Interactions		19
1.6 SU(6) and its Relativistic Extension $\tilde{U}(12)$		24
<u>Chapter 2 - The Bubble Chamber, Beam and</u>		
<u>Measuring Machines</u>		31
2.1 Introduction		31
2.2 Design of the Separated Kaon Beam		32
2.3 Layout of the Beam		34
2.4 Beam Tuning Procedure		36
2.5 General Description of the Imperial College Measuring Machines		38
2.6 Automatic Track Following		40

<u>Chapter 3 - The Data Processing System</u>	page 47
3.1 Introduction	47
3.2 Scanning, Measuring and Book-keeping	47
3.3 The Geometry Programme	49
3.4 Errors on Track Variables	51
3.5 The Kinematic Fitting Programme	53
3.6 The Statistics Programme	58
3.7 Maximum Likelihood and the Determination of Density Matrix Parameters	59
<u>Chapter 4 - Biases and Background</u>	63
4.1 The General Approach to Event Classification	63
4.2 Estimation of the Pion Background	65
4.3 Biases in the Lambda Hyperon Events	66
4.4 Missing Mass Considerations	69
<u>Chapter 5 - Total Cross Sections</u>	79
5.1 Detection Efficiency	79
5.2 Cross Section Calculations	80
5.3 Single Strange Particle Channels	82
5.4 Associated Production Channels	82

<u>Chapter 6 - Production of the <math>\rho^0, \omega^0</math> and <math>\phi^0</math> Mesons</u>	page
6.1 Introduction	92
6.2 Production in Association with a $\Lambda$ Hyperon	93
6.3 Production in Association with a $\Sigma$ Hyperon	98
6.4 Production in the KN and $\Xi$ K Channels	102
<u>Chapter 7 - Production of the <math>\rho^\pm</math> and Other Resonances</u>	122
7.1 Introduction	122
7.2 Charged $\rho$ Production in Association with a $\Lambda$ Hyperon	123
7.3 Charged $\phi$ Production in Association with a $\Sigma$ Hyperon	125
7.4 Production of the $\eta^0$ and $X^0$ Resonances	126
7.5 Other Zero Hypercharge Boson Resonance Production	128
<u>Chapter 8 - Summary and Comparisons with Theory</u>	143
8.1 Resonance Parameters	143
8.2 Energy Dependence of Cross Sections	145
8.3 The SU(3) Cross Section Relationships	146
8.4 Exchange Mechanisms and the Absorption Model	151
8.5 Future Investigations	157
Acknowledgements	165
References	166

PREFACE

The author joined the High Energy Nuclear Physics Group at Imperial College in October 1961, and was initially involved in an experiment designed to search for evidence for high energy neutron-proton charge exchange scattering using the Nuclear Emulsion technique.

In October–November 1962 the author assisted in the construction and tuning of the CERN M2 beam, and was present at each of the exposures of the Saclay Hydrogen Bubble Chamber to K mesons which took place in the interval up until December 1963. The track following device described in chapter 2 of this thesis was also developed during this period, under the direction of Dr. S.J. Goldsack.

The analysis of the 3.5 GeV/c  $K^-$  film from the above exposures was undertaken by a collaboration between the Universities of Glasgow, Oxford and Birmingham, the Rutherford High Energy Laboratory, Harwell, and Imperial College.

The author was responsible for the compilation and analysis of the data for all the reactions in which the incident kaons produced three strange particles.

CHAPTER 1

SYMMETRY THEORIES AND THE ZERO HYPERCHARGE MESONS

1.1 Charge Independence and the Definition of Hypercharge

Many of the symmetries occurring in low energy nuclear physics can be accounted for by assuming that the proton and neutron represent, to a first approximation, two states of a single particle, the nucleon. The nucleon can therefore be considered as possessing an additional quantum number, the isotopic spin, the third component of which takes on the values  $+\frac{1}{2}$  and  $-\frac{1}{2}$  for the proton and neutron respectively. The charge independence of nuclear forces can be explained by assigning an isotopic spin to the pions, and assuming that the Lagrangian describing the pion-nucleon interaction is a scalar in isotopic spin space. A further consequence of this hypothesis is the triangle inequality relating the pion-proton elastic and charge exchange scattering cross sections.

The charge  $Q$  (in units of the proton charge  $e$ ) carried by a pion or nucleon is related to the third component of the isotopic spin  $I_3$  as follows,

$$Q = I_3 + B/2$$

where  $B$ , the baryon number, is zero for the pions and one for the nucleons.

In 1953 Gell-Mann (1) and Nishijima (2) succeeded in giving a semi-phenomenological explanation of the strong production - weak decay paradox which existed for the strange particles. They did this by extending the charge independence concept to include the processes in which the strange particles are produced, but not those via which they decay. Once the strange particles have been assigned an isotopic spin, it is possible to explain their observed associated production in terms of the conservation of this quantum number. The necessary violation of this conservation law in the decay processes provides an explanation for their long lifetimes.

In order that the expression for  $Q$  should hold for both strange and non-strange particles, it must be modified by the introduction of another quantum number  $S$ , the strangeness, such that

$$Q = I_3 + B/2 + S/2.$$

$S$  is different from zero for the strange particles only. Since both  $Q$  and  $I_3$  are assumed to be conserved in strong interactions, so also is the hypercharge  $Y$ , defined as the sum of  $B$  and  $S$ .  $Q$  may now be written,

$$Q = I_3 + Y/2$$

The boson resonances for which detailed discussion will be presented in this thesis all have  $Y$ , and of course  $B$ , equal to zero.

### 1.2 Consequences of SU(2) Invariance for Pions and Nucleons

If the Lagrangian describing the pion-nucleon interaction is to be an invariant in isotopic spin space, the pion and nucleon wave functions in this space must both belong to irreducible representations of the three-dimensional rotation group <sup>3)</sup>. One such representation is obtained by considering the action of all unitary, unimodular, two-dimensional matrices, with complex coefficients, on the two component spinor  $\psi$  describing the nucleon. In other words, the rotation invariance is equivalent to invariance under all the linear transformations  $U$ , with the above properties, which mix the proton and neutron wave functions.

$$\psi_i \rightarrow \psi'_i = U_i^k \psi_k$$

$$\psi_i = \begin{pmatrix} p \\ n \end{pmatrix} \quad U^\dagger = U^{-1} \quad \det U = 1$$

By considering the transformation properties of spin tensors consisting of outer products of the basic spinors, further irreducible representations of the rotation group may be obtained; these may in turn be associated with the

various isotopic spin multiplets. Since the pion has three charge states, the pion wave function is a vector in isotopic spin space, and transforms by means of the usual three-dimensional rotation matrices. The wave functions ( $\tau_k$ ) provide the basis for a three-dimensional representation of the rotation group.

The actual form of the interaction Lagrangian between pions and nucleons,

$$L_I = ig\bar{\psi}\gamma_5\tau_k\psi\pi_k$$

shows that  $\tau_k$  transforms in the same way as the product  $\bar{\psi}\gamma_5\tau_k\psi$ , and suggests that the pions might be considered, in some senses at least, as bound states of the nucleon-antinucleon system. It is easy to show that a vector having the required transformation properties can be constructed from the product  $\psi\bar{\psi}$ .

Expressing  $\psi\bar{\psi}$  as the sum of two tensors  $\pi$  and  $\eta$  as follows,

$$\psi_i\psi^j = \pi_i^j + \eta_i^j$$

$$\text{with } \pi_i^j = \psi_i\psi^j - \frac{1}{2}\delta_i^j\psi_k\psi^k \quad \text{and} \quad \eta_i^j = \frac{1}{2}\delta_i^j\psi_k\psi^k$$

then both  $\pi$  and  $\eta$  form irreducible representations of the group SU(2), with dimensions of 3 and 1 respectively.  $\pi$  when written as a matrix has the form

$$\pi_i^j = \begin{bmatrix} (p\bar{p} - n\bar{n})/2 & p\bar{n} \\ n\bar{p} & -(p\bar{p} - n\bar{n})/2 \end{bmatrix}$$

Linear combinations of the three distinct components of this tensor possess the same transformation properties as a three component vector,  $\vec{\pi}$ . Any traceless two-dimensional matrix may be expanded in terms of the matrices  $\tau_k$ , the isotopic spin equivalents of the Pauli matrices.

$$\pi_i^j = \vec{\pi} \cdot \vec{\tau}_i^j$$

$$\pi_i^j = \sqrt{2} \begin{bmatrix} \pi_3/\sqrt{2} & (\pi_1 - i\pi_2)/\sqrt{2} \\ (\pi_1 + i\pi_2)/\sqrt{2} & -\pi_3/\sqrt{2} \end{bmatrix} = \sqrt{2} \begin{bmatrix} \pi^0/\sqrt{2} & \pi^+ \\ \pi^- & -\pi^0/\sqrt{2} \end{bmatrix}$$

From these two expansions of the matrix  $\pi$  it is possible to see that the product wave functions,

$$\pi^+ \Rightarrow p\bar{n}, \quad \pi^0 \Rightarrow (p\bar{p} - n\bar{n})/\sqrt{2} \quad \text{and} \quad \pi^- \Rightarrow n\bar{p}$$

have  $l_3 = +1, 0$  and  $-1$  respectively, and are therefore suitable for describing the pions.

In exactly the same way, the  $N^*$  (1238) can be accommodated in a multiplet obtained from the expansion of the product  $\psi\psi\bar{\psi}$ , the deuteron in a multiplet obtained from  $\psi\psi$ , and so on, for all nuclei and pion-nucleon resonances

Zero hypercharge mesons belong to irreducible representations for which  $B = 0$ , which is equivalent to requiring that there are as many  $\psi$ 's as  $\bar{\psi}$ 's in the product. At this stage it must be observed, however, that the scheme is not complete, since non-strange particles could equally well be built up from hyperon-antihyperon pairs.

### 1.3 The Development of SU(3)

Using the two component nucleon spinor as the fundamental multiplet, it is impossible to construct wave functions describing particles carrying strangeness. To do this it is necessary to introduce at least one additional "fundamental" particle. The simplest extension of the scheme described previously was first suggested by Sakata <sup>4)</sup>. He proposed that the basic object should be supplemented by the addition of the  $\Lambda$  hyperon.

$$\psi_i = \begin{pmatrix} p \\ n \\ \Lambda \end{pmatrix}$$

It was then postulated that the strong interactions might be invariant under those transformations of this basic multiplet which could be brought about by the application of unitary, unimodular, three-dimensional matrices. All the pseudoscalar mesons can be assigned, within this scheme,

to the eight-dimensional representation of the group  $SU(3)$  constructed from the product  $\psi\bar{\psi}$ . The particles belonging to a multiplet obtained in this way should have the same mass; consequently, the principle symmetry breaking mechanism is far stronger than for the  $SU(2)$  group discussed in section 2. In the Sakata model the baryons must be constructed from a triple product of the form  $\psi\psi\bar{\psi}$ . It is at this point that the model fails, since the eight and tenfold multiplets in which the baryons are observed to occur cannot be constructed from this product.

Gell-Mann <sup>5)</sup> and Ne'eman <sup>6)</sup> suggested that the group  $SU(3)$  could be retained as a possible symmetry under which the strong interactions are approximately invariant, by assigning the eight  $J = \frac{1}{2}$  baryons to the same representation as that to which the mesons are assigned in the Sakata model. Requiring the invariance to be  $SU(3)$ , and not  $SU(8)$ , led them to predict the existence of the eight vector mesons which were subsequently discovered experimentally. This meant that, for a time at least, the possibility of considering all the particles and resonances as bound states of a single three component object was abandoned.

Recently, Gell-Mann <sup>7)</sup> and Zweig <sup>8)</sup> have demonstrated that the original Sakata approach can also be retained if

the interpretation of  $\psi$  is changed. In this new "quark" or "ace" model,  $\psi$  is assumed to have exactly the same isotopic spin content as the original "Sakaton", the difference being that it no longer carries unit charge and baryon number. It is possible to construct a product  $\psi\psi\psi$  having  $B = 1$ , which contains both the eight and ten-dimensional representations of  $SU(3)$ , as long as the fundamental fields have  $B = 1/3$ .

Denoting the quark by

$$q_i = \begin{pmatrix} p' \\ n' \\ \Lambda' \end{pmatrix}$$

the mesons belonging to the eight-dimensional irreducible representation of  $SU(3)$  can be constructed as follows,

$$M_i^j = q_i q^j - \frac{1}{3} \delta_i^j q_k q^k$$

The components of this tensor behave like the components of an eight-dimensional vector under the transformations of  $SU(3)$ .  $M_i^j$  can be expressed in terms of the generators ( $\bar{\lambda}$ ) of  $SU(3)$ , just as  $\pi_i^j$  was expressed in terms of the generators ( $\bar{\tau}$ ) of  $SU(2)$ .

$$M_i^j = \bar{M} \cdot \bar{\lambda}_i^j, \quad \bar{M} = (\pi_1, \pi_2, \dots, \pi_8)$$

$$M_i^j = \sqrt{2} \begin{bmatrix} \frac{\pi_3}{\sqrt{2}} + \frac{\pi_8}{\sqrt{6}} & \frac{\pi_1 - i\pi_2}{\sqrt{2}} & \frac{\pi_4 - i\pi_5}{\sqrt{2}} \\ \frac{\pi_1 + i\pi_2}{\sqrt{2}} & -\frac{\pi_3}{\sqrt{2}} + \frac{\pi_8}{\sqrt{6}} & \frac{\pi_6 - i\pi_7}{\sqrt{2}} \\ \frac{\pi_4 + i\pi_5}{\sqrt{2}} & \frac{\pi_6 + i\pi_7}{\sqrt{2}} & -\frac{2}{\sqrt{6}} \pi_8 \end{bmatrix}$$

As before, the isotopic spin content can be obtained immediately by writing  $M$  in terms of  $q$  and  $\bar{q}$ .

$$M_i^j = \begin{bmatrix} \frac{1}{3}(2p'\bar{p}' - n'\bar{n}' - \Lambda'\bar{\Lambda}') & p'\bar{n}' & p'\bar{\Lambda}' \\ n'\bar{p}' & -\frac{1}{3}(p'\bar{p}' - 2n'\bar{n}' + \Lambda'\bar{\Lambda}') & n'\bar{\Lambda}' \\ p'\bar{\Lambda}' & \Lambda'\bar{n}' & -\frac{1}{3}(p'\bar{p}' + n'\bar{n}' - 2\Lambda'\bar{\Lambda}') \end{bmatrix}$$

The matrix describing the mesons can then be expressed

$$M_i^j = \sqrt{2} \begin{bmatrix} \frac{\pi^0}{\sqrt{2}} + \frac{\eta^0}{\sqrt{6}} & \pi^+ & K^+ \\ \pi^- & -\frac{\pi^0}{\sqrt{2}} - \frac{\eta^0}{\sqrt{6}} & K^0 \\ K^- & \bar{K}^0 & -\frac{2}{\sqrt{6}} \eta^0 \end{bmatrix}$$

where the  $\pi, K$  and  $\eta^0$  stand for the familiar pseudoscalar mesons, and one sees that, apart from the addition of the term  $-\pi^0/\sqrt{6}$ , the leading  $2 \times 2$  matrix is exactly the same as before. In the same way the matrix describing the vector mesons can be written,

$$V_i^j = \sqrt{2} \begin{bmatrix} \frac{\rho}{\sqrt{2}} - \frac{\phi_8}{\sqrt{6}} & \rho^+ & K^{*+} \\ \rho^- & -\frac{\rho^0}{\sqrt{2}} - \frac{\phi_8}{\sqrt{6}} & K^{*0} \\ K^{*-} & \bar{K}^{*0} & \frac{2}{\sqrt{6}} \phi_8 \end{bmatrix}$$

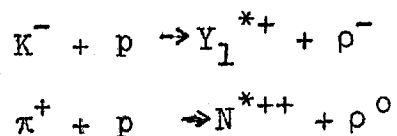
where  $\phi_8$ , the octet isoscalar meson, is discussed in more detail in the next section. The treatment of the baryons is similar but slightly more complicated, since they are built from triple products. Weight diagrams indicating the isotopic spin and hypercharge contents of the various multiplets are presented in Fig. 1.1.

#### 1.4 Experimental Consequences of SU(3).

If the strong interactions are invariant under SU(3), many cross section relationships can be derived in addition to these obtained by invoking the charge independence

hypothesis, but the more approximate nature of this higher symmetry is expected to give rise to larger discrepancies when comparisons are made with the experimental cross sections.

The proton and the negative kaon both belong to eight-dimensional representations of  $SU(3)$ , consequently, the state  $|K^-p\rangle$  can be expanded in terms of a Clebsch-Gordan series involving the irreducible representations contained in the product  $8 \otimes 8$ . This is analogous to the expansion of  $|K^-p\rangle$  in terms of the eigenstates of the total isotopic spin. Final states involving two particles belonging to eight or ten-dimensional representations can similarly be expanded in terms of the irreducible representations contained in  $8 \otimes 8$ ,  $8 \otimes 10$  etc. Considering the reactions



for example, it is observed that the cross sections for these processes can be expressed in terms of the four amplitudes describing the transition from  $8 \otimes 8$  to  $8 \otimes 10^9$ ). In this way one can calculate many relationships between cross sections for the associated production of decuplet baryon resonances and octet vector mesons. The case of  $8 \otimes 8 \rightarrow 8 \otimes 8$  is not quite so severely restricted, since both initial and final

states can be expanded in terms of the same irreducible representations; in this case there are 8 independent amplitudes. Some of the consequences of SU(3) are compared with the experimental results in chapter 8. The large mass differences within the multiplets can be compensated, to a certain extent, by comparing the cross sections at the same energy above threshold in the centre of mass. This approach has been considered in detail in the literature<sup>10)</sup>.

By making assumptions about the way in which SU(3) is broken, Gell-Mann<sup>5)</sup> and Okubo<sup>11)</sup> were able to derive mass relationships within the multiplets. A list of these has been given by Zweig<sup>12)</sup>. One of the most important of these relationships, as far as the present discussion is concerned, is the following

$$3m(\text{singlet})^2 + m(\text{triplet})^2 = 4m(\text{doublet})^2,$$

which relates the masses of the bosons belonging to eight-dimensional representations. This equality is found to be correct to within a few per-cent for the pseudoscalar mesons. However, in the case of the vector mesons it predicts an isoscalar meson mass,  $m(\phi_8) = 927$  Mev, when the masses of the well established isodoublet ( $K^*(891)$ ) and isovector ( $\rho(763)$ ) are inserted. Gell-Mann suggested that this disagreement could be accounted for if another isoscalar

of approximately the same mass, but belonging to a singlet representation, existed, which mixed with the octet isoscalar and caused a mass splitting to occur. Subsequently, another isoscalar vector meson was observed ( $\phi(1020)$ ). The mixing angle can be obtained, since with  $\phi_1$  and  $\phi_8$  given by

$$|\phi_1\rangle = \cos\lambda|\omega\rangle + \sin\lambda|\phi\rangle$$

$$|\phi_8\rangle = \sin\lambda|\omega\rangle - \cos\lambda|\phi\rangle$$

the angle  $\lambda$  has to be such that  $M_{(\phi_8)} = 927$ . By diagonalising the mass matrix Sakurai<sup>13)</sup> and others have shown that  $\lambda=38^\circ$ , i.e.  $\sin\lambda \approx 1/3$  and  $\cos\lambda \approx 2/3$ . This leads to additional predictions concerning the relative  $\omega$  and  $\phi$  cross sections in channels such as

$$K^- + p \rightarrow \Lambda + \omega$$

$$K^- + p \rightarrow \Lambda + \phi$$

if, for example, pure K exchange happens to dominate in the production mechanism<sup>14)</sup>. The experimental results for these channels are compared in chapter 8. Other effects of fixing the angle  $\lambda$  are to limit the magnitudes of certain couplings and to determine the relative rates of decay into lepton pairs.

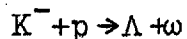
### 1.5 Peripheral Interactions.

In the region above 2 GeV/c incident momentum the

boson resonances produced in K-proton collisions frequently exhibit the strong forward collimation characteristic of peripheral interactions. It is generally considered that the forward peaking is a result of production mechanisms in which mesons are exchanged between the colliding particles. These exchanged mesons represent single particle intermediate states in the crossed ( $t$ ) channel. (The crossed channels are defined in Fig.1.2.)

Since very few of the more massive boson resonances belonging to the higher dimensional representations of  $SU(3)$  have so far been observed (candidates, the  $f^0$  (1250),  $A_2$  (1310) and the recently discovered  $K^*$  (1400)) the effect of neglecting the exchange of these particles is worth considering. More restrictions may be placed on the cross sections using  $SU(3)$ , if the only single particle exchange processes which are important are pseudoscalar and vector meson exchange. Under these conditions the cross sections can be calculated explicitly in terms of the constants  $g_f$  and  $g_d$  associated with the F and D couplings of Gell-Mann<sup>5)</sup>. The experimental consequences of these assumptions, on the behaviour of the differential cross sections and decay angular distributions, are easily determined.

To take a specific example, in the process



the simple Born approximation, using pure K exchange as the dominant production mechanism, predicts a backward peak for the  $\omega$  in the centre of mass system, Fig. 8.4. Experience with this model has shown that the predicted centre of mass angular distributions are nearly always less peaked in the forward direction than the experimental distributions. Gottfried and Jackson<sup>15)</sup> have pointed out that, before comparing the results of the single particle exchange model with experiment, one should attempt to take into account the absorption of the low angular momentum partial waves resulting from the presence, at high energies, of many competing inelastic processes. These authors have studied the consequences of a "Distorted Wave Born Approximation", in which such an attempt is made. The agreement between the calculated and observed distributions is almost completely satisfactory in this model.

In discussing the decay of a vector meson in its rest frame, it is convenient to consider the population of the states described by the spherical harmonics  $Y_1^0$  and  $Y_1^{\pm 1}$  (16). Usually the decay is characterised by two angles

$\theta$  and  $\varphi$ . These locate the unit vector in the direction of one of the decay products, in a two body decay, or the normal to the decay plane, in a three body decay.  $\theta$  is a polar angle and  $\varphi$  an azimuthal angle (cf. Fig. 1.3) in a frame of reference such that the normal to the production plane ( $\underline{n}$ ) is taken as the y-axis, the incident  $K^-$  direction ( $\underline{I}$ ) as the z-axis, and the direction orthogonal to these two ( $\underline{n} \times \underline{I}$ ) as the x-axis. The production plane is defined by the directions of the incoming  $K^-$  and outgoing vector meson. Conservation of parity and angular momentum require that pseudoscalar exchange lead to a population of the state  $|Y_1^0\rangle$  only, and vector exchange to a population of the  $|Y_1^{\pm 1}\rangle$  states. This means that the density matrix  $\rho_{ij}$  describing the decay has  $\rho_{00} = 1$  for pure pseudoscalar exchange, and  $\rho_{00} = 0$  for pure vector exchange.

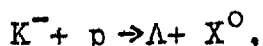
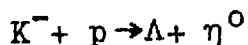
Once the effects of absorption are included it is found that the density matrix element  $\rho_{00}$  may be considerably different from unity and yet still be consistent with pure pseudoscalar exchange. There is one other important test which may be applied when pure scalar exchange is suspected. Since a scalar particle can carry no angular information the distribution of the angle  $\varphi$  should be flat (this is shown

in a paper by Treiman and Yang<sup>17)</sup> - the angle discussed by these authors is related to the  $\phi$  defined above - Jackson<sup>18)</sup> ). This result implies that  $\rho_{1-1}$  should be zero for pure pseudo-scalar exchange, and is not substantially modified by the inclusion of absorption. The remaining term which may also be computed from the experimental distributions is  $\text{Re } \rho_{10}$ . Unless there is interference between the various natural parity exchange processes this term should also be zero. A non-zero value for  $\text{Re } \rho_{10}$  is observed as a rather curious correlation between the angles  $\theta$  and  $\phi$ . It is to be noted that there are many processes for which the absorption model predicts a non vanishing  $\text{Re } \rho_{10}$ ; the determination of this quantity provides another means of testing the model. These considerations are taken up again in chapter 8, where the density matrix elements for the  $\rho, \omega$  and  $\phi$  mesons observed in the present experiment, are discussed in detail.

In the single meson exchange model it is assumed that the t-channel singularities nearest to the physical region dominate the scattering amplitude. For high energy processes<sup>S</sup> involving  $\pi, \eta, K, \rho$  and  $\omega$  exchange this is reasonable, since the nearest singularity in the u-channel usually corresponds to the nucleon or lightest hyperon and, apart from the question of branching ratios, unitarity limits the contribution from

any pole in the direct or s-channel, corresponding to the formation of an intermediate  $Y^*$ . When  $K^*$  is demanded the approximation becomes less reasonable. Baryon exchange in the u-channel might alter significantly both the differential and total cross sections, especially if the associated coupling constants are large.

Finally, in the cases of  $\eta^0$  and  $X^0$  production in the channels



$K^*$  exchange is the only allowed single meson exchange process and yields a total cross section which increases with energy, even when absorption is taken into account. This is a familiar feature of vector exchange calculations. The experimental cross sections are falling fairly rapidly in the region from 2.3 - 3.5 Gev/c. A more realistic treatment is required, which includes the effects of the channels that are opening up as the energy increases. A K-matrix approach designed to take these into account is being developed<sup>19)</sup>.

### 1.6 SU(6) and its Relativistic Extension $\tilde{U}(12)$ .

A static theory which includes the effects of spin has recently been proposed. It considers a basic quark

having six rather than three components

$$q_i = \begin{pmatrix} p' \uparrow \\ p' \downarrow \\ n' \uparrow \\ n' \downarrow \\ \Lambda' \uparrow \\ \Lambda' \downarrow \end{pmatrix}$$

where the symbols indicate that a  $p'$  with spin up ( $\uparrow$ ) and a  $p'$  with spin down ( $\downarrow$ ) are considered as two separate components. This approach was suggested by Radicati and Gurse<sup>20)</sup> and Sakita<sup>61)</sup> (cf. also Zweig<sup>12)</sup>), as a direct extension of the static SU(4) considered by Wigner<sup>62)</sup> in nuclear physics. The mesons and baryons are constructed exactly as before in terms of products such as  $q_i q^k$  and  $q_i q_j q_k$  respectively. The mesons can be very conveniently accommodated in a 35-dimensional representation of SU(6) which has the following SU(3) - unitary spin- and SU(2) - physical spin - contents

SU(3)	SU(2)
Octet	Singlet
Octet	Triplet
Singlet	Triplet

i.e. the  $\pi, \eta, K, \rho, \phi, K^*$  and  $\omega$  mesons all belong to the same SU(6) multiplet. In addition there is room for an isoscalar belonging to a one-dimensional representation, and it has been suggested that the recently discovered  $X^0$  fills just this position. Two of the most important consequences of SU(6) are that the F/D coupling ratio discussed by Gell-Mann is fixed uniquely (thus more cross section relationships), and furthermore, the  $\omega$ - $\phi$  mixing angle is completely determined. The physical  $\omega$  and  $\phi$  can be expressed in terms of the isoscalar vector meson belonging to the SU(3) octet ( $\phi_8$ ) and the singlet ( $\phi_1$ ) as follows

$$\begin{aligned} |\omega\rangle &= \sqrt{\frac{2}{3}} |\phi_1\rangle + \sqrt{\frac{1}{3}} |\phi_8\rangle \\ |\phi\rangle &= \sqrt{\frac{1}{3}} |\phi_1\rangle - \sqrt{\frac{2}{3}} |\phi_8\rangle, \end{aligned}$$

in complete agreement with the calculations mentioned previously in connection with the mass splitting.

Since the theory does not include the effects of angular momentum other than the intrinsic spin carried by the particles, very few of the cross section relationships unique to SU(6) are worth considering.

Recently many attempts have been made to generalize the static SU(6), that is, to make it into a relativistically covariant theory. Probably the most important of these is

the  $\tilde{U}(12)$  theory of Salam, Delbourgo and Strathdee<sup>63)</sup>, in which the basic object is a 12 component quark, each of the p', n' and  $\Lambda'$  being described by a four component Dirac like spinor. Invariance under the most general unitary transformations which can be performed on this basic spinor can be shown to include invariance under both the homogeneous Lorentz group  $L_4$  and  $SU(3)$ . Since in this case the space-time transformation properties of the basic quark are being considered it is necessary to ensure that the products, e.g.  $q_i q^k$ , can be associated with particles of definite mass and spin also. This requirement is fulfilled if the irreducible representations obtained from these spinor products obey the Bargmann-Wigner equations of motion. Once these equations are applied one finds that the spin and unitary spin contents of the low dimension representations are exactly the same as in  $SU(6)$ . In fact it is found that the theory can account in a very simple fashion for a 35-fold multiplet of mesons having negative parity and a 56-fold multiplet of baryons with positive parity. Probably the most important feature of  $\tilde{U}(12)$  is that the various form factors used in cross section calculations are related.

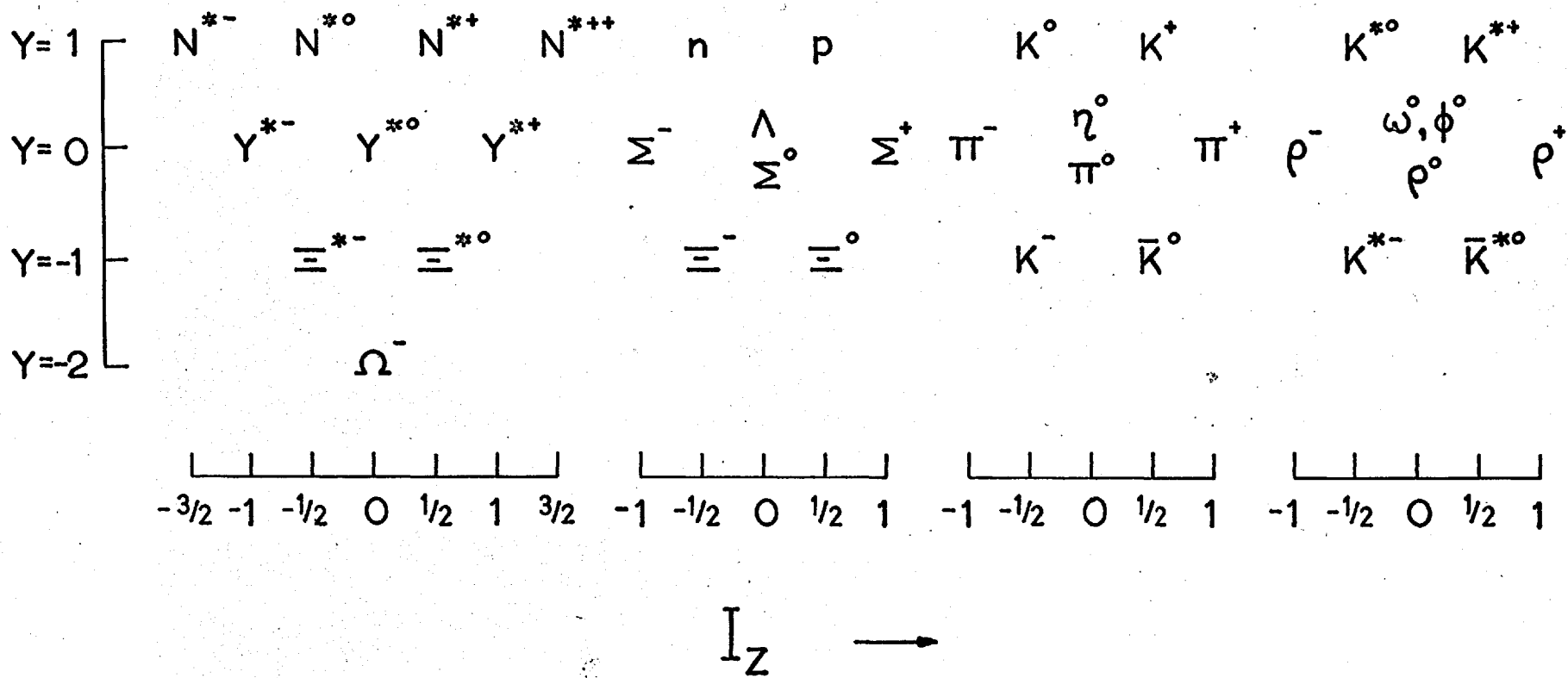
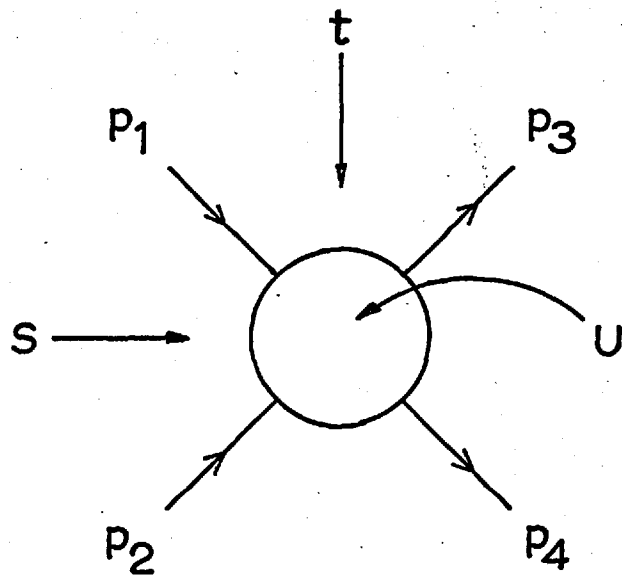


Fig.11 SU(3) Multiplets



$$s = (p_1 + p_2)^2$$

$$t = (p_1 - p_3)^2$$

$$u = (p_1 - p_4)^2$$

Possible Single Particle Intermediate States for

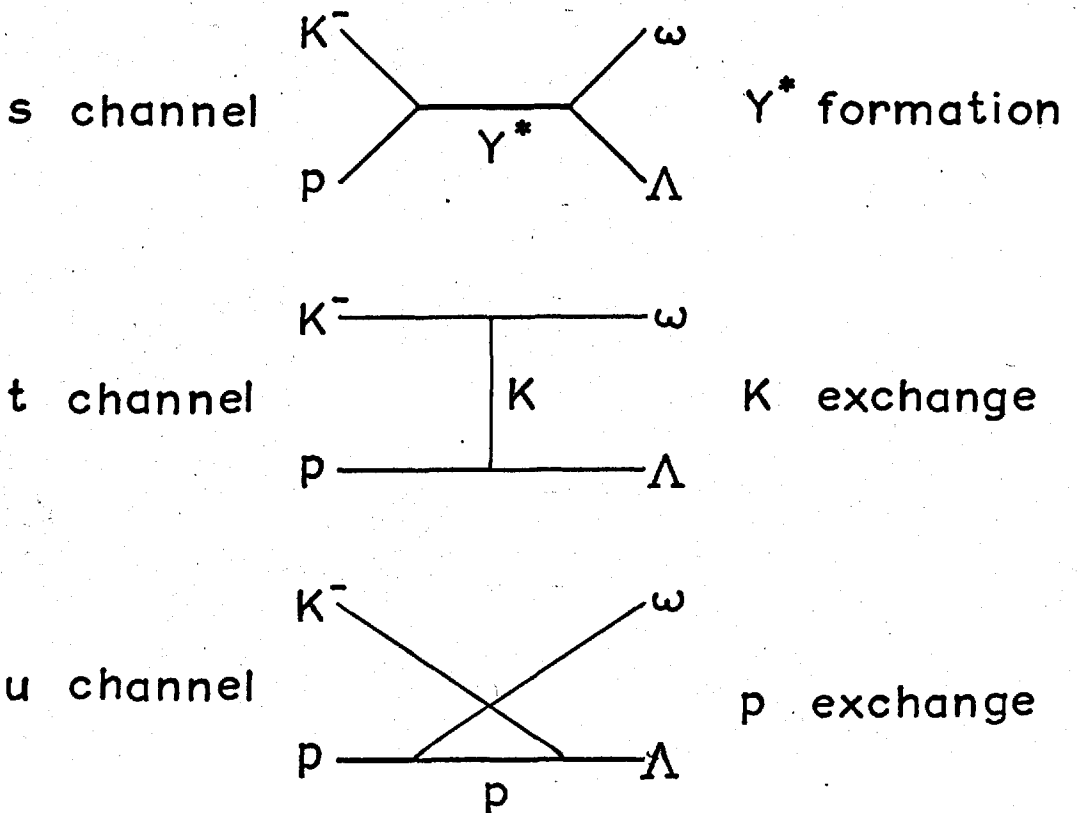
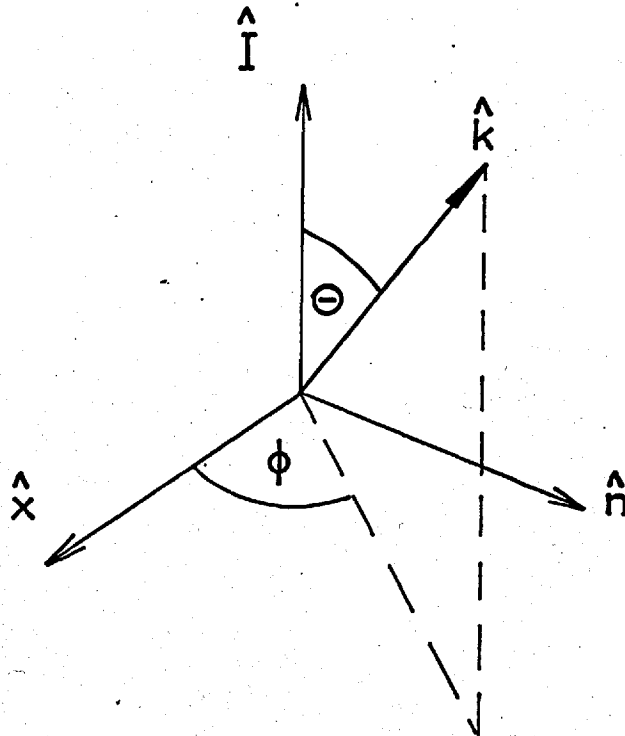


Fig. 1.2

## Vector Meson Rest Frame



$\hat{I}$  : Direction of Incident K Meson

$\hat{n}$  : Normal to Production Plane

$\hat{k}$  : Direction of Decay Product

$\hat{x}$  :  $(\hat{n} \wedge \hat{I}) / |\hat{n} \wedge \hat{I}|$

$\phi$  :  $\equiv$  Treiman-Yang Angle

Fig. 1.3 Decay Angles for the Vector Mesons

CHAPTER 2THE BUBBLE CHAMBER, BEAM AND MEASURING MACHINES2.1 Introduction.

In October 1962 a beam was laid down at the CERN proton synchrotron (CPS) which was capable of providing high momentum separated kaons; details of the design and construction of this beam are given in sections 2.2-2.4 below. The Saclay 81 cm. hydrogen bubble chamber was exposed to 3.5 Gev/c negative kaons from this beam, and a total of approximately 310,000 useful photographs were obtained, containing, on average, about 10 kaons per picture. The bubble chamber has been described in detail elsewhere <sup>21)</sup> and only a few of its salient parameters are given here.

The chamber is 81 cm. in length and has a height of 40 cm. and a depth of 31.6 cm. Three flash tubes are used to illuminate a volume of approximately 90 litres of the liquid. The tracks caused by the passage of ionising particles through the hydrogen in this illuminated region, are photographed by means of three cameras arranged on a triangular base of side 30.7 cm. situated 97.3 cm. from the front glass window of the chamber. The fiducial crosses required for stereo-reconstruction

are inscribed on the inner surfaces of the front and back windows. A magnetic field of 20.7 kilogauss is superimposed on the liquid in the chamber.

The film from the three exposures needed to obtain the photographs, was distributed amongst five bubble chamber film analysis groups working in the United Kingdom. Most of it was measured on machines of comparable accuracy, enabling the final data to be combined without the necessity for any complex weighting procedure. Section 2.5 of this chapter contains a brief description of these machines, whereas in section 2.6 an account is given of a track following device which was incorporated into one of them.

## 2.2 Design of the Separated Kaon Beam.

Apart from the separation problem, the CERN M1 beam <sup>22)</sup> was not capable of providing kaons of sufficient intensity for a bubble chamber exposure, primarily because of its great length (113 metres). The beam which replaced it, the M2, provided a fairly pure K-meson beam up to a momentum of 3.5 Gev/c, this being achieved by doubling the separation and decreasing the over-all length to approximately 80 metres.

A single stage beam consisting of two CERN electrostatic separators and the associated quadrupoles would have occupied

a distance of at least 55 metres. Such a single stage could not have been constructed inside the CPS shielding wall in the target area. If it had been placed in the South Hall of the CPS it would have resulted in a beam of at least 95 metres length. The possibility of constructing a two stage beam was therefore considered, in which one of the separators was placed in the target area and the other in the South Hall. The preliminary design studies showed that such a beam would also have considerable advantages, from the point of view of contamination, over a single stage beam of the M1 variety <sup>23)</sup>.

The available space in the target area was still not sufficient to allow a conventional first stage, consisting of a quadrupole doublet followed by the separator followed by a further doublet, to be included there; consequently, the second doublet was removed and the separator was operated with a converging beam. (Placing a second doublet outside the shielding wall would have given rise to an increase of 11 metres in the total length.) This arrangement results in a slightly decreased separation ratio  $\eta$  - defined as the spatial separation of the  $\pi$  and K images divided by the image width - compared to that obtained with a conventional stage of the same length operated with the same acceptance.

J. Goldberg <sup>24)</sup> demonstrated that if the usual doublet in front of the separator were replaced by a triplet, it would be possible to adjust the acceptance and magnification to suit the beam momentum. For a high beam momentum a given separation ratio (of 2 for example -  $\eta > 2$  does not result in a significant decrease in the number of transmitted contaminating particles) could be obtained using a small vertical acceptance and consequently lower magnification, whereas for a lower momentum, where the loss of kaons through disintegration becomes more important, larger acceptance and increased magnification would result in approximately the same separation ratio and transmission factor.

### 2.3 Layout of the Beam.

The layout of the beam is shown in Fig. 2.1 and beam envelopes in the horizontal and vertical planes are shown in Fig. 2.2. Mass separation occurs in the vertical plane and momentum analysis in the horizontal plane. An angle of  $8\frac{1}{2}^\circ$  with the circulating proton beam in the synchrotron was chosen in order that the intensity of kaons at the bubble chamber would be sufficiently high, with a primary momentum of 19 Gev/c, to operate with only a fraction of the primary beam striking the target. If a smaller angle had been used the virtual target position as seen through the PS fringe

field would have been a function of the secondary momentum.

In the horizontal plane quadrupoles Q1 - Q3 focus the beam at F1 where momentum analysis occurs as a result of the dispersive action of bending magnet BM1. A second horizontal focus occurs at F3 and is achieved by means of quadrupole Q4. Two horizontal foci are necessary before bending magnets BM2 and BM3 in order that the dispersion of the latter, which bend the beam in the opposite sense to BM1, may be compensated at the final horizontal image F4. The functions of quadrupoles Q5, Q6 and Q7, Q8 can be seen from Fig. 2.2a. The first vertical focus occurs at F2, 11 metres beyond F1 on the other side of the shielding wall. From this point to the final focus F4 the beam is of conventional design in the vertical plane as can be seen from the beam envelope of Fig. 2.2b.

The collimator C1 was used to limit the horizontal and vertical acceptance of the beam, whilst the mass slits at MS1 and MS2 served to remove the unwanted pions. The last stage of the beam between MS2 and the bubble chamber consisted of a bending magnet to remove off-momentum background particles and a quadrupole to spread the beam vertically before entrance into the bubble chamber. The only mylar windows in the beam were situated in the regions of F2 and F4. It was necessary to have breaks in the vacuum pipe at these positions in order

that the scintillation counters used for tuning could be inserted.

#### 2.4 Beam Tuning Procedure.

All images were studied by means of scintillation counters inserted in the beam before the first mass slit and on either side of the final mass slit. Vertical images were examined, either by closing the corresponding mass slit to 1 mm. and measuring the transmitted intensity as the image was swept across the slit using the separator compensation magnets CM1-2 or CM3-4 (Fig. 2.1), or by moving a thin scintillation counter across the stationary image using a suitably placed motor driven carriage. The first horizontal image could not be examined directly but the second was studied once by means of a movable counter.

Images were improved by making the following adjustments: CM1-2 (or CM3-4, depending on the stage being tuned) was altered until the intensity was reduced by a factor of 20, i.e. the image was set off-centre. The quadrupole currents were then changed until the transmitted intensity went through a minimum. This corresponded to a condition in which the image had its smallest dimensions and was located in the best position with respect to the mass slit, which was not necessarily the centre of the slit. When the size of the

image - defined as twice the full width at half maximum intensity - was of the same order of magnitude as had been expected from the ray tracing, the beam was considered suitably adjusted.

Next the separation in the vertical plane was investigated for the first stage. As soon as the pion and antiproton images were visible on the separation curves the expected kaon image position was calculated. Occasionally this image showed up as a shoulder on the pion peak. The compensation magnets on the first separator were adjusted until the calculated kaon peak was centred in the first mass slit and the separation curve for the second stage was measured. Usually a fairly prominent kaon peak was found at this point. After this image had been centred in MS2 the adjustments of the first stage were repeated. In this way the best operating conditions were found by what was essentially an iterative procedure.

Separation curves for the second stage are shown in Fig. 2.3. Also shown is a curve obtained with a Cerenkov counter placed behind the second mass slit in coincidence with the scintillation counters. This counter was arranged so that it only responded to the pions, and therefore the

difference between the two separation curves clearly indicates the presence of the kaons. Unfortunately, the high pressure gas Cerenkov counter used to obtain this curve developed a serious leak before the start of the exposure, resulting in the impossibility of counting directly the number of contaminating particles entering the chamber. A facility whereby such information could be recorded on each photographic frame had been provided, and subsequent analysis showed that it would have been invaluable in providing a means of reducing the amount of almost pure pion film which was actually measured.

## 2.5 General Description of the Imperial College Measuring Machines.

The purpose of a measuring machine of the type used in bubble chamber physics is to provide accurate measurements of points on bubble chamber film relative to an origin such as a fiducial cross. The co-ordinates of these points are usually recorded by means of Moire fringe digitizers. On the main Imperial College machines these are attached to the stage on which the film is mounted -x motion, and the carriage carrying the projection lenses -y motion. Co-ordinates are punched as binary coded octal numbers on paper tape, along with other information necessary to identify the item being

measured.

To make full use of the small - two  $\mu$ m - bit size of the digitizers, optical arrangements are provided in order that the region surrounding the point to be measured may be examined in detail. The machines have either a high magnification screen on which the film may be studied visually, or a special line scanning system such as a Sambatron.

The Sambatron consists of an eight sided glass prism mounted in front of a photo-multiplier onto which a magnified image of a small area of the film is projected. The prism is set up so that it may be rotated about two orthogonal axes as shown in Fig. 2.4. A mechanical coupling ensures that the axis AA' is always parallel to the direction of motion of the projected image. A rotation of the prism about this axis causes the image to move in the direction shown in the diagram. By placing a narrow slit between the photo-multiplier and the prism and rotating the latter at a frequency  $f$  (revs/sec), it is possible to scan the image in the direction perpendicular to AA' at a frequency  $8f$  (c/sec). As can be seen from the diagram, the bevelled edges of the prism are blackened in order to provide well defined limits to the scans from the adjacent faces. The form of the signal from the photo-multiplier, as displayed on an oscilloscope, is

shown in Fig. 2.5a. The rounded pulse between the two rectangular 'dark' pulses represents a slightly off-centre track. A fiducial pulse, obtained by reflecting light from a silvered strip on the block (Fig. 2.4), is used to indicate the moment at which a prism face is parallel to the film plane. With this orientation of the prism, light reaching the photo-multiplier originates from a point on the optic axis. The inverse of this pulse is combined with the 'track' signal from the photo-multiplier, Fig. 2.5b. A track is regarded as centred when the track pulse straddles the fiducial pulse which therefore serves to mark the zero-error position.

## 2.6 Automatic Track Following.

To maintain a track in the zero-error position as the projected image is moved in a direction parallel to the track an additional servo-loop has been introduced. This makes it possible to punch out the co-ordinates of points along the track with the image in motion.

Two gate pulses are generated, the first of which, the 'early gate', is switched off by the fiducial pulse at the same time as the second, the 'late gate', is switched on. The two gates are of equal length and together provide a signal of about the same duration as an average track pulse Fig. 2.5c.

Each of these gates is 'ANDED' with the track pulse and the resultant signals are fed into opposite sides of a difference amplifier. The integrated output of this amplifier is fed via a phase advance network and sine-cosine resolver to the servos controlling the motion of the film stage and lens carriage. The output is arranged so that when a track is centred no net signal is supplied to the servos. If the image is off-centre a signal is provided which corrects the deviation and returns the system to the central position.

In practice it was impossible to completely damp out the oscillations which occurred about the zero-error position; this has resulted in slightly increased track measurement errors. Fig. 2.6 shows histograms of these measurement errors (as defined in chapter 3) for two machines, one with and one without track following. Before making a comparison it must be remarked that the machine without track following was inherently capable of slightly greater accuracy. The factor gained in speed using this system was considered more important than the slight loss of accuracy.

TABLE 1M2 Beam Parameters

Angle made with circulating proton beam	8.5°
Length to first mass slit	39.2m
Length to second mass slit	77.1m
Length to bubble chamber	87.0m

## Target

1 x 4 x 25 mm. at 0° Aluminium (80% eff.)

Solid Angle at 3.5 Gev/c

$$\alpha_V = 1.54 \text{ mrad.}$$

$$\alpha_H = 8.80 \text{ mrad.}$$

$$\Omega = 4 \alpha_V \alpha_H = 0.55 \times 10^{-4} \text{ sterad.}$$

Momentum Bite  $\frac{\Delta p}{p} = \pm \frac{1}{4}\%$

Separation between 3.5 Gev/c K<sup>-</sup> and  $\pi^-$

$$\theta = 0.134 \text{ mrad. at 55 kv/cm}$$

$$S = F\theta = 2.37 \text{ mm. at mass slit 1.}$$

$$= 2.65 \text{ mm. at mass slit 2.}$$

Intensities at 3.5 Gev/c (at chamber)

3000  $\pi^-$ , 30  $\bar{p}$ , 8 K<sup>-</sup> per 10<sup>11</sup> protons at 19.4 Gev/c

1. Collimator
2. Quadrupole 1
3. " 2
4. Bending Magnet 1
5. Quadrupole 3
6. Compensating Magnet
7. Separator
8. Momentum Slit
9. Sextupole
10. Mass Slit 1
11. Quadrupole 4
12. Bending Magnet 2
13. Quadrupole 5
14. Bending Magnet 3
15. Quadrupole 6
16. " 7
17. " 8
18. Mass Slit 2
19. Bending Magnet 4
20. Quadrupole 9
21. Magnet
22. Bubble Chamber

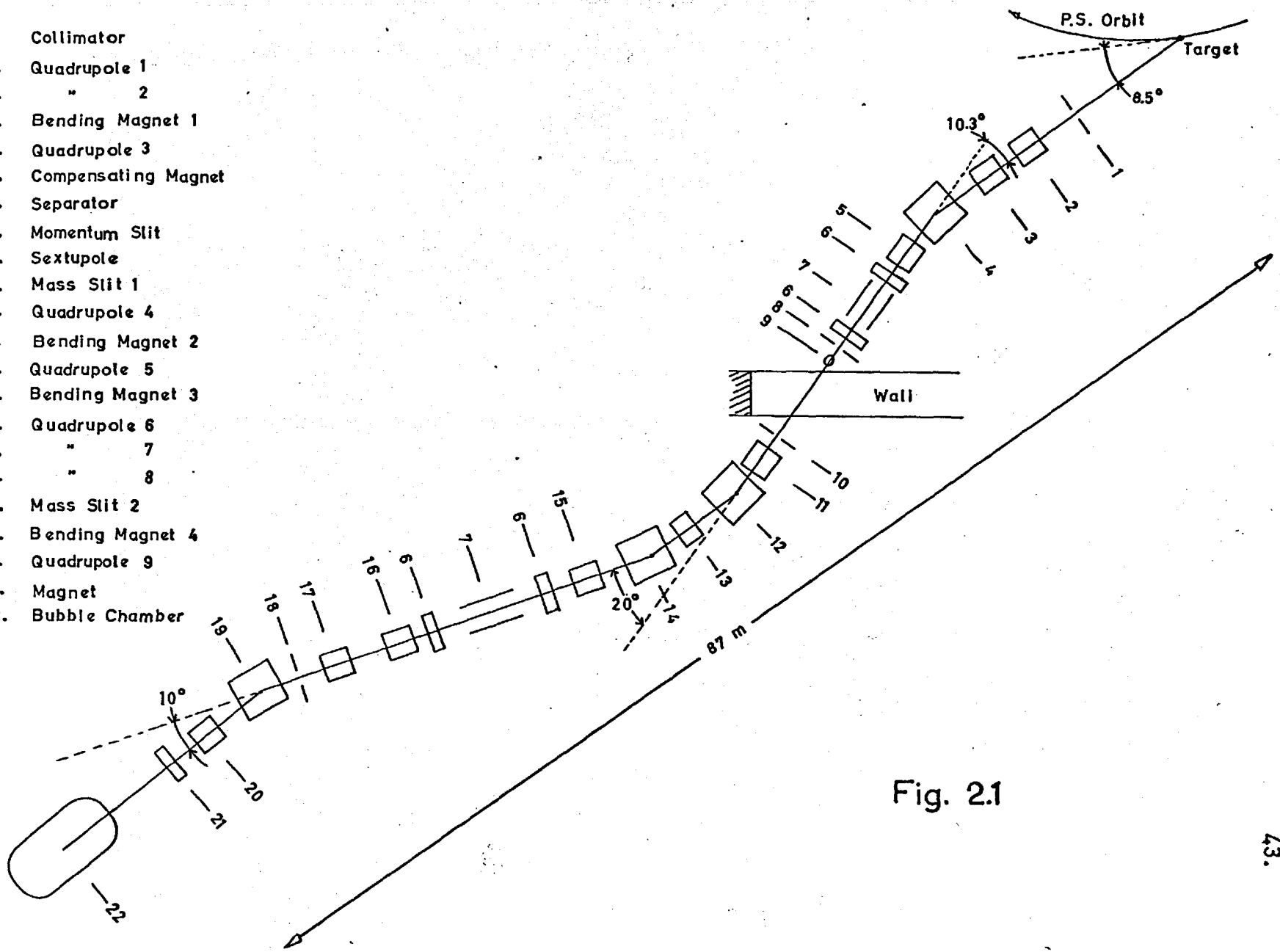


Fig. 2.1

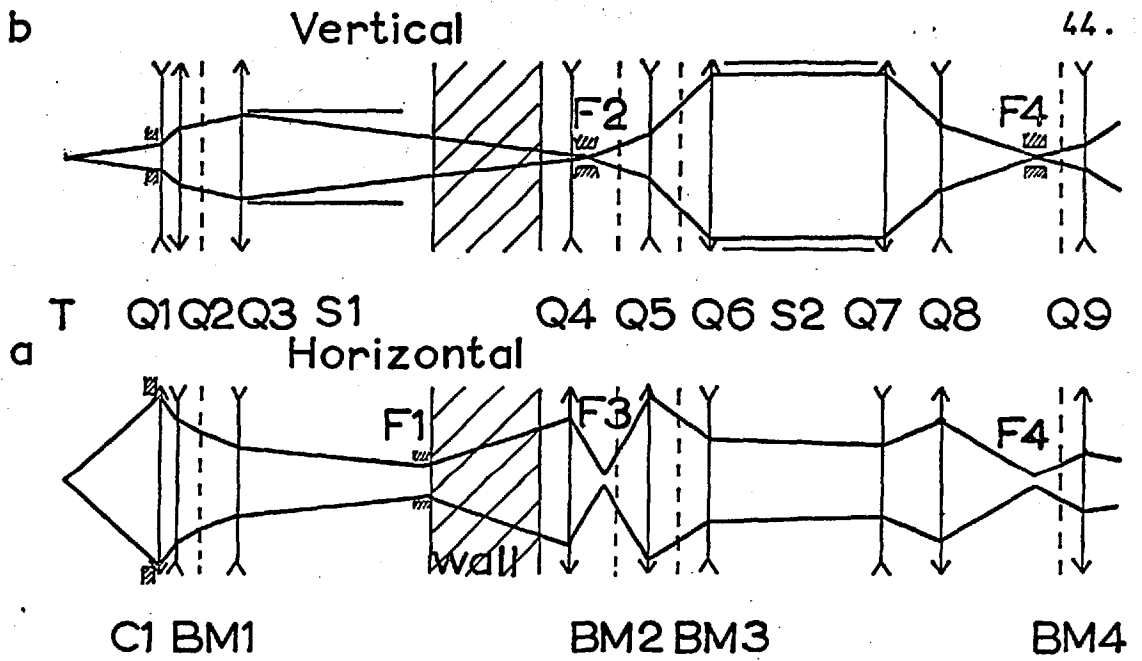


Fig. 2.2 Beam Envelopes

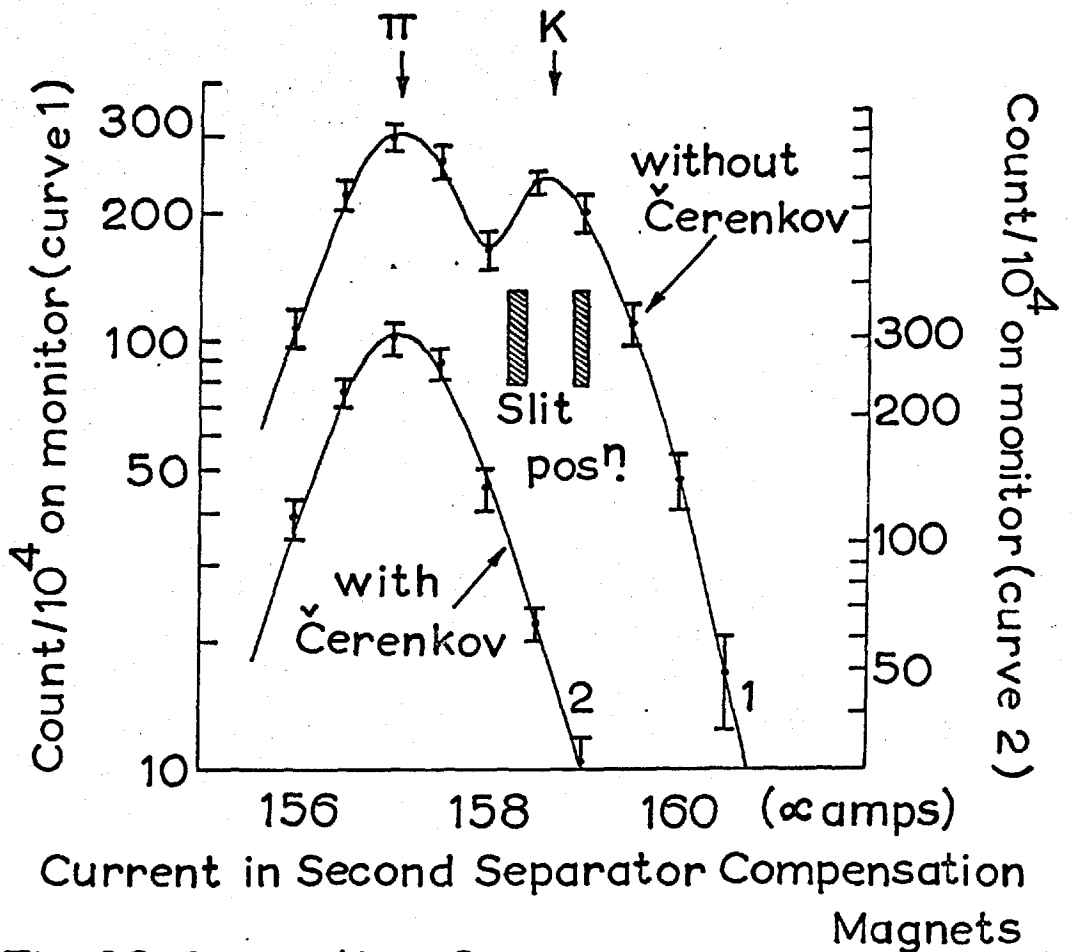


Fig. 2.3 Separation Curves

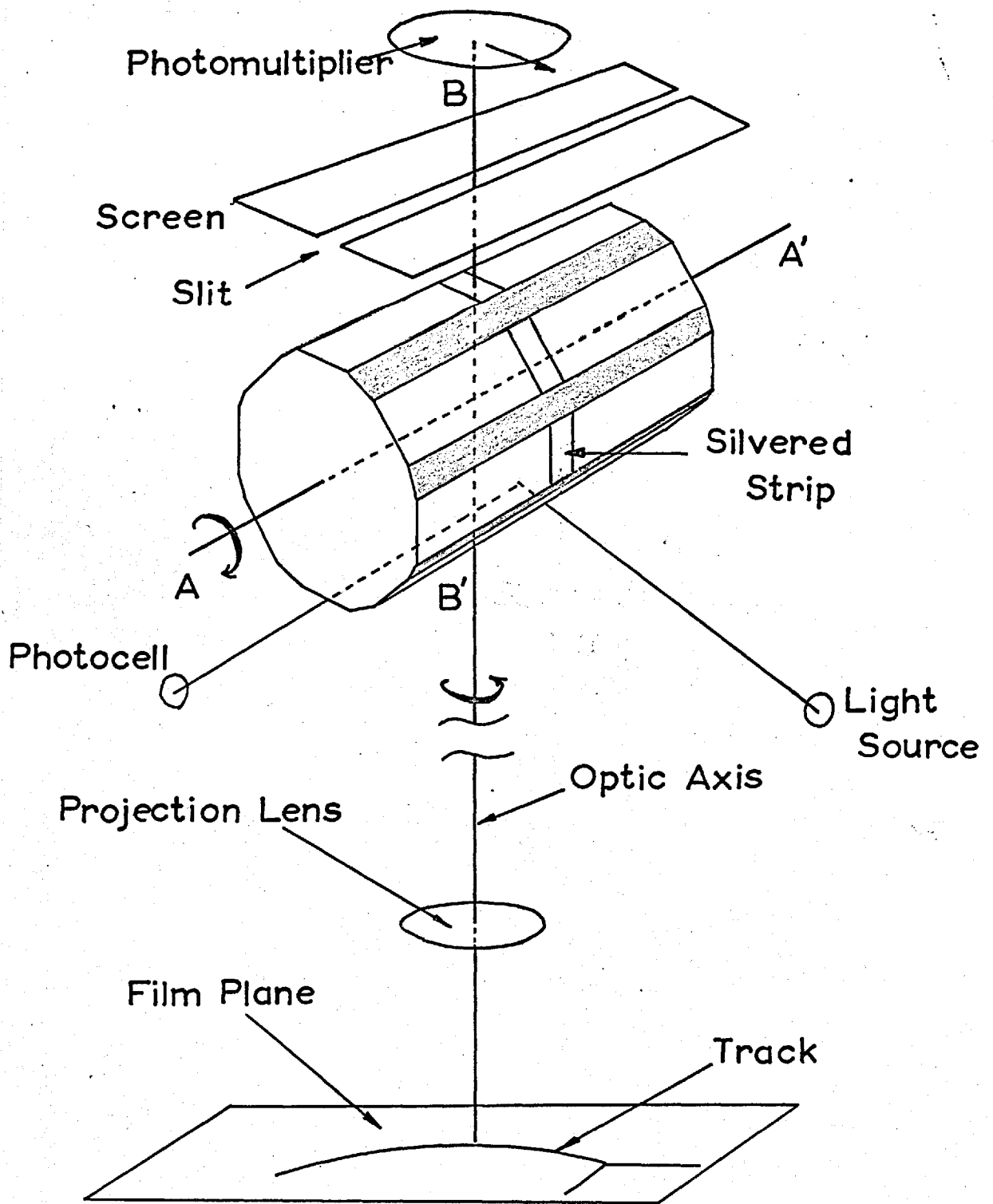


Fig. 2.4 Sambatron (schematic)

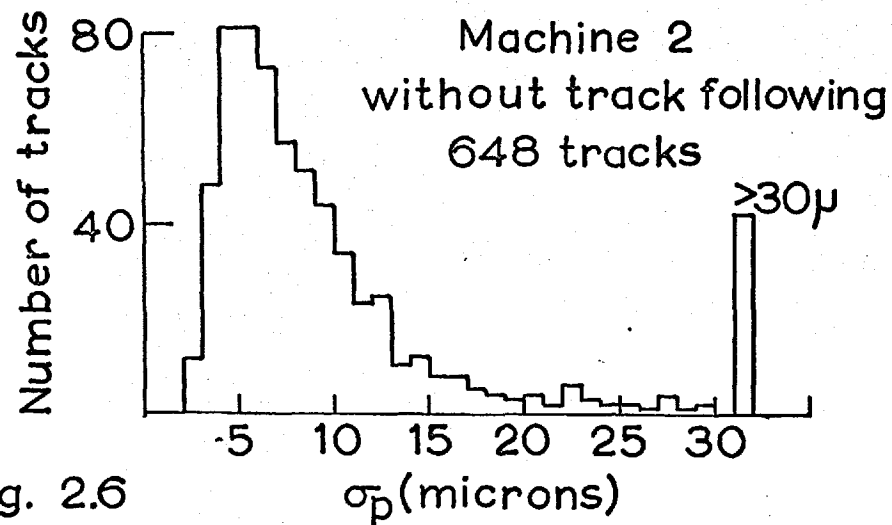
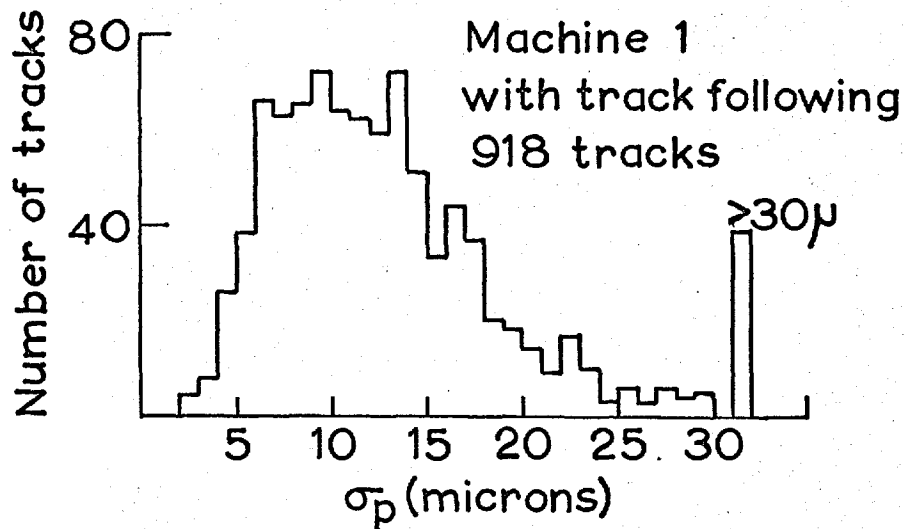


Fig. 2.6

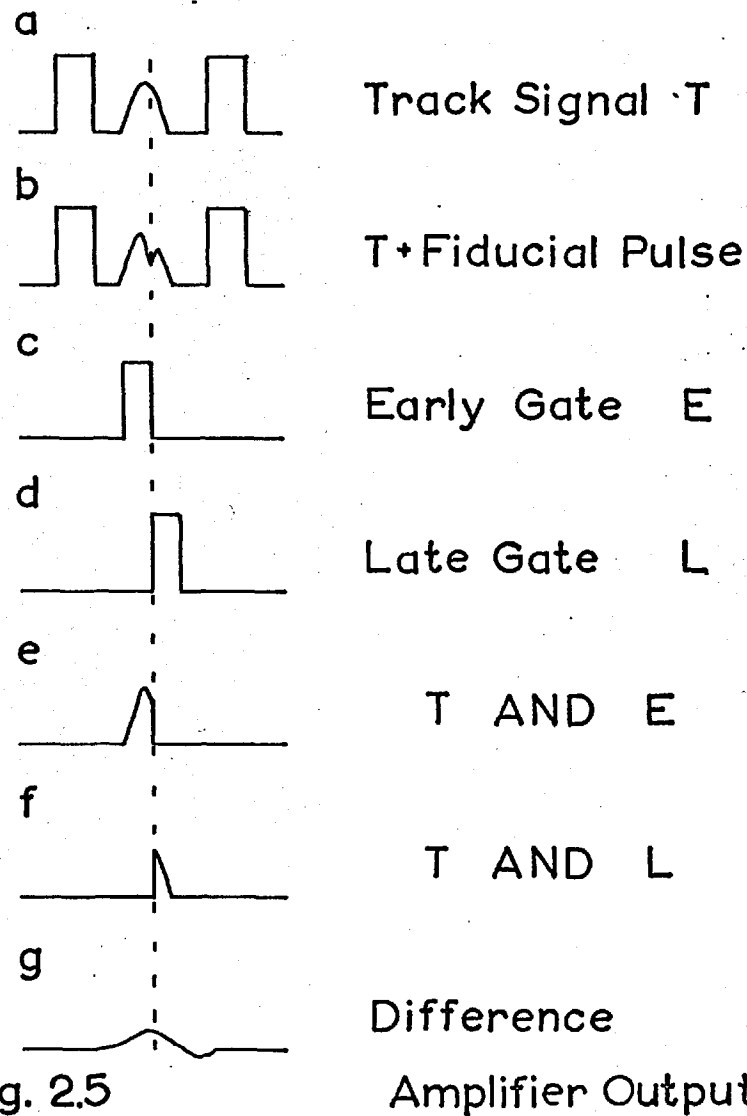


Fig. 2.5

## CHAPTER 3

### THE DATA PROCESSING SYSTEM

#### 3.1 Introduction.

This chapter is concerned with the techniques used to scan for, measure and compute events in the 41,000 stereoscopic triplets analysed by the Imperial College group. The rest of the film was treated in a similar manner by the other groups in the collaboration. The scanning, measuring and book-keeping are discussed in section 3.2 below. In sections 3.3-3.5 the geometrical reconstruction and kinematic fitting programmes are described, whilst sections 3.6 and 3.7 are concerned with the post-fitting analysis programmes.

#### 3.2 Scanning, Measuring and Book-keeping.

During each of the two scans of the entire film, two views of the chamber were examined for all events in which one or more decays were visible. The events were classed according to the total number of charged secondary tracks present,  $N_c$ , the number of secondary tracks which decayed,  $N_D$ , and the number of associated neutral particle decays,  $N_V$ . These three numbers were combined to form a single three digit code number ( $N_c N_D N_V$ ) which provided a complete

description of the event. Events involving two or more decays were recorded no matter where they occurred in the chamber. For the commoner events involving a single decay a restricted fiducial volume was chosen in order to exclude events exhibiting short tracks. The information recorded during the scans was used to prepare library lists of events and to compute the scanning losses which had to be allowed for in the cross section calculations. All beam track  $\tau$ - decays were also noted.

The frame, event and code numbers for each interaction were recorded on a special scanning card. Space was provided on this card for a rough sketch of the event, and any additional measurement instructions necessary for the recording of stopping points etc. The only criteria used during scanning to remove events involving non-strange particle decays were the following: stopped positive pions were identified by their characteristic 1 cm. muon tracks, and electron-positron pairs were identified by slow but minimum ionising tracks on zero opening angle neutral decays.

The measurements were made on the machines described in the last chapter. The measurers were supplied with the scanning cards and instructed to measure each interaction in a pre-arranged sequence for fiducials, tracks and apices.

A Ferranti Mercury computer was then used to transfer the data from its paper tape format to cards. These were loaded onto magnetic tape via an IBM 1401 computer for input to an IBM 7090 computer.

### 3.3 The Geometry Programme.

The main function of the geometrical reconstruction programme is to provide an estimate, with errors, of the vector momentum for each of the charged particles involved in a bubble chamber interaction. Before this is possible the parameters describing the trajectory of the particle in space must be found, using the measurements made on each of the conical projections of the trajectory available on film. To a first approximation the trajectory may be taken as part of a helix, the axis of which is parallel to the direction of the magnetic field in the chamber. Once the parameters specifying the helix have been found, it is possible to obtain the momentum and direction of the track by performing a least squares fit to a helix of variable curvature. This allows for the slowing down of the particle in the chamber liquid resulting from the energy loss brought about by Coulomb interactions.

The programme which was used to carry out this geometrical reconstruction was written at the Rutherford

Laboratory by J.W.Burren and J. Sparrow<sup>25)</sup>.

### The first space fit

Each film measurement is used, together with the known positions of the camera lenses, to define a ray in the chamber liquid. These rays are employed to obtain approximate space co-ordinates along the trajectory. Once these space points have been determined for all three views the first approximation helix fit takes place.

In a suitable frame of reference the equation of the helix may be written,

$$x = \alpha + \rho \cos \theta$$

$$y = \beta + \rho \sin \theta$$

$$z = \gamma + \rho \theta \tan \lambda.$$

The x-y projection is a circle of radius  $\rho$  and centre  $(\alpha, \beta)$ . These parameters are determined by the method of least squares using the (x,y) co-ordinates of the space points mentioned above. As soon as  $\alpha, \beta$  and  $\rho$  are known  $\theta$  is calculated for each spatial co-ordinate and  $\tan \lambda$  is found from the linear dependence of  $z$  on  $\theta$ , again by means of a least squares fit.

### The Final Mass Dependent Helix Fit<sup>26)</sup>.

To take the slowing down into account two mass dependent terms  $C_x(\theta)$  and  $C_y(\theta)$  are included in the equations for  $x$  and  $y$  respectively. The computation of

these terms is discussed in detail in the Lawrence Radiation Laboratory Memorandum by F.T. Solmitz<sup>27)</sup>. The final least squares fit is made to a projection of the modified helix on a nominal film plane. The quantity,  $\sum d_i^2$ , which is rendered a minimum in the least squares fit is the sum of the squares of the deviations from the projection of the helix of the N reprojected ray co-ordinates  $(x_f, y_f)$ .

The output of the programme consists of the momentum and two angles defining the direction of the track with respect to a left handed co-ordinate system, oriented such that the x-y plane is parallel to the front window. The angles are  $\lambda$ , the dip with respect to this plane, and  $\phi$ , an azimuthal angle measured with respect to the x-axis. These quantities and their associated errors are produced for each track using three mass assignments, as proton, kaon and pion.

### 3.4 Errors on Track Variables.

The reason for making the final helix fit on a nominal film plane is intimately associated with the determination of the errors on  $p$ ,  $\tan \lambda$  and  $\phi$ . The errors on the track variables are obtained directly from the quantity

$$\sigma_p^2 = \frac{1}{N-5} (\sum d_i^2)_{\text{final}}$$

by means of the usual propagation formulae (this quantity also provides a measure of the goodness of the final fit).

It is because this quantity is so closely related to the errors on the co-ordinate pairs actually measured that this particular treatment is used. The magnitude of  $\sigma_p$  is governed by the extent of turbulence and Coulomb scattering in the chamber liquid and by the accuracy of the measuring machine.

In order to overcome the difficulty associated with the statistical fluctuations of  $\sigma_p$  (which might lead to bad chi squares in the kinematic fitting programme), it was allocated a standard value  $\sigma_f$ . To decide on a suitable value for  $\sigma_f$  the distribution of  $\sigma_p$  for a large number of measured tracks was examined, cf. Fig. 2.6, and  $\sigma_f$  was set equal to the mode of this distribution. As a result  $\sigma_f$  was taken as  $8\mu$  in the programme, but whenever  $\sigma_p$  was larger than  $12\mu$  the track was regarded as badly measured and the internally calculated value was used. There is one slightly unpleasant aspect to this approach. In general the value of  $\sigma_m$ , the error introduced by the measuring machine, is a function of the total number of rays used in the final fit ( $\sigma_m \propto N^{-\frac{1}{2}}$ ). This means that  $\sigma_p$  is also dependent on this number, and, strictly speaking, the magnitude of  $\sigma_p$  is not entirely a matter of statistics. In practice the value of  $N$  usually ranges between about 15 and 30 giving  $\sim 25\%$  variation in  $\sigma_m$ , and the procedure of using a single value for  $\sigma_f$  is

probably more or less justified. The errors due to Coulomb scattering were computed after the final fit and added to those calculated from  $\sigma_p$ . There are several other sources of both random and systematic errors but most of these are negligible compared with the errors discussed above. A detailed analysis of these errors for the Saclay Hydrogen bubble chamber has recently been given by J. Badier<sup>28)</sup>.

### 3.5 The Kinematic Fitting Programme.

The four conservation laws for a given interaction vertex can be written, using the variables  $p, \lambda$  and  $\phi$ ,

$$\sum_1 p_{x_i} = \sum_1 (c_i) p_i \cos \phi_i \cos \lambda_i = 0$$

$$\sum_1 p_{y_i} = \sum_1 (c_i) p_i \sin \phi_i \cos \lambda_i = 0$$

$$\sum_1 p_{z_i} = \sum_1 (c_i) p_i \sin \lambda_i = 0$$

$$\sum_1 E_i = \sum_1 (c_i) \sqrt{p_i^2 + m_i^2} = 0$$

where  $c_i = +1$  ( $-1$ ) for an outgoing (incoming) track at the vertex and  $m_i$  is the mass of the  $i$ -th track. The summation is over all tracks at the vertex. These constraint equations, together with the values of  $p$ ,  $\lambda$  and  $\phi$  obtained by the geometry programme, are used to determine any of the variables which are unmeasured. For example, if a vertex involves a neutral particle then the vector momentum of the particle can be found using three of the conditions given above. Although three of the constraints will then be satisfied exactly, the fourth will not, due to the measurement errors on the charged tracks. To obtain improved values of all the track variables, the method of least squares is used to adjust the variables in such a way that all four equations are satisfied, subject to the  $X^2$  being a minimum, where  $X^2$  is defined by

$$X^2 = \sum_{ij} (x_i - x_i^m) G_{ij}^x (x_j - x_j^m)$$

here  $x_i$  is the  $i$ -th track variable and  $(G_{ij}^x)^{-1}$  is the error matrix associated with the track variables. The constraint equations are automatically taken into account if the expression

$$M = \sum_{ij} (x_i - x_i^m) G_{ij}^x (x_j - x_j^m) + 2 \sum_{\lambda} a_{\lambda} f_{\lambda}(x)$$

is minimized, where  $f_\lambda$  ( $\lambda = 1, \dots, 4_N$ ) are the constraint conditions and the  $a_\lambda$  are Lagrange multipliers. (N = no. of vertices.) The programme written to perform this kinematic fitting is due to A.G. Wilson <sup>29</sup>).

For the majority of the interactions to be "fitted" the masses associated with the tracks are unknown. This means that for each topological specification (see page 62) several possible hypotheses allowed by the conservation laws for charge, strangeness etc., must be tested. The masses are assigned to the charged (and perhaps neutral) tracks in an event by a special hypothesis assigning programme <sup>30</sup>), which takes into account all possible permutations in cases of ambiguity.

Once the masses are assigned the fitting programme is entered, and it proceeds to determine whether the energy-momentum conservation laws can be satisfied for this assignment. If the iterative procedure used to seek the minimum of the function M converges, the final value of  $X^2$  together with the adjusted values of the track variables are stored, and a "fit" is registered. In general each interaction fits several hypotheses and additional information must be used to decide which is the correct hypothesis. The methods used to make these final decisions are discussed in chapter 4.

The distribution of  $X^2$ , when plotted for a large number of events, will depend on the number of constraint equations which are used in finding starting values for unmeasured variables. If all the constraint equations are used to find such variables then no adjustment is possible (0- constraint case) and  $X^2$  has no meaning. If three are used up in a single vertex fit then  $X^2$  should have a distribution corresponding to a single degree of freedom, and so on. The actual distribution of  $X^2$ , for a given number of degrees of freedom, depends critically on the errors assigned to the track variables by the geometry programme, as well as on which variables are used in the fitting process. The programme under discussion makes use of the values of  $1/p$ ,  $\tan \lambda$  and  $\phi$  determined at the centre of each track. These variables are chosen since they are closely related to the quantities measured and are therefore more likely to have normally distributed errors. Before the fitting commences the vertex variables are obtained by a swimming procedure using the known range-momentum relation for each track. This procedure, together with the justification for using centre-of-track variables, is discussed in the kinematics programme report <sup>29)</sup>.

If the errors assigned to the variables for a given event are too large, the corresponding  $X^2$  for the correct

hypothesis will tend to be too small, and vice versa. Overestimation of the errors results in  $\chi^2$  distributions which are biased toward low values. Apart from this, overestimation also allows more fits to incorrect hypotheses. Underestimation, on the other hand, leads to larger  $\chi^2$  and thence to a loss of genuine fits if an upper limit on the allowed value of  $\chi^2$  is employed. The experimental  $\chi^2$  plots are discussed in Chapter 4.

Several other quantities are computed by the kinematics programme to enable bias investigations to be undertaken. For all vertices involving a missing neutral particle the mass associated with this particle is calculated using the fourth constraint equation. Distributions of these "missing masses" are given later. The  $\chi^2$  together with the number of degrees of freedom are used to compute a  $\chi^2$  probability <sup>31)</sup>. This quantity can be used to decide on the goodness of a given fit without reference to the number of degrees of freedom involved. Finally, a "normalised stretch" is evaluated for each track variable

$$S_i = \frac{x_i - x_i^m}{\langle \delta(x_i - x_i^m) \delta(x_i - x_i^m) \rangle^{\frac{1}{2}}}$$

Plots of  $S_i$  should have a gaussian distribution about 0 with a standard error of 1. The usefulness of this quantity in seeking systematic errors is considered in the next chapter.

### 3.6 The Statistics Programme.

The Statistics programme (written by J.M. Scarr) has two main functions. The first of these is to calculate quantities of physical interest from the fitted results.

These consist of :

- a) Effective masses for groups of particles.
- b) Centre of mass momenta and angles for individual particles and resonances.
- c) The invariant momentum transfer corresponding to diagrams involving meson exchange.
- d) Baryon polarization angles.
- e) Resonance decay angles.
- f) Angles required for density matrix analysis (cf. section 1.5).

The second principal function is to provide histograms and two-dimensional plots of these quantities. For the effective mass histograms Lorentz invariant phase space curves <sup>32)</sup> are superimposed, and kinematic boundaries are provided on both Dalitz and Triangle plots. Plots may also be

generated using various selection criteria, enabling associated production of resonances and effects of reflections to be investigated. All one-dimensional plots may be produced under various weight conditions, whereby the individual events are weighted according to the nature and position of their decay products.

A special version of the programme is available which allows information to be obtained from unfitted events. In this version the mass and momentum of the missing neutral are calculated from the geometrical values of the momenta for the charged tracks. This track is then treated in exactly the same way as a normal track and allows effective masses involving, for example, multiple neutrals to be studied.

### 3.7 Maximum Likelihood and the determination of Density Matrix Parameters.

#### The Maximum Likelihood Method 33)

For the case to be considered below the problem to be solved is the following; given a set of  $N$  events each characterised by  $j$  physical quantities  $x_j$ , what is the best set of  $M$  parameters  $a_k$  ( $k = 1, \dots, M$ ) in the function  $f(a_k; x) = f(a_1, a_2, \dots, a_M; x)$  which describe the experimental distribution? For the  $i$ -th event, the probability of obtaining the values

$x_j^{(i)}$  is proportional to

$$P_i = f(\alpha_k; x_j^{(i)}).$$

The joint probability for the  $N$  events is therefore given by,

$$P = \prod_{i=1}^N P_i = \prod_{i=1}^N f(\alpha_k; x_j^{(i)}).$$

The best estimates of the parameters  $\alpha_k$  are obtained by searching for the maximum of this function (usually denoted  $L(\alpha_k)$ ). Furthermore, if  $N$  is sufficiently large (good statistics) the function can be shown to have a single maximum.

In practice numerical methods were used to search for these solutions, using two programmes written at the Lawrence Radiation Laboratory by F. Grand<sup>34)</sup> and W.E. Humphrey<sup>35)</sup>. These programmes seek the maximum of the logarithm of the likelihood function

$$W = \ln L(\alpha_k).$$

### The Density Matrix.

The decay distribution of a vector meson in terms of the angles  $\theta$  and  $\phi$  (cf. chapter 1), has been shown by Jackson et al<sup>36)</sup> to be related to the elements of its density

matrix  $\rho_{ij}$  as follows,

$$W(\theta, \varphi) = \frac{3}{4\pi} [\rho_{00} \cos^2 \theta + \rho_{11} \sin^2 \theta - \rho_{1-1} \sin^2 \theta \cos 2\varphi - \sqrt{2} \operatorname{Re} \rho_{10} \sin 2\theta \cos \varphi]$$

where trace  $\rho$  ( $= 2\rho_{11} + \rho_{00}$ ) is normalised to unity. The experimentally determined values of  $\theta$  and  $\varphi$  for events occurring in the region of a given resonance (usually with a momentum transfer cut-off) were employed to find the values of  $\rho_{00}$ ,  $\rho_{11}$ ,  $\rho_{1-1}$  and the  $\operatorname{Re} \rho_{10}$ , thus leaving only  $\operatorname{Im} \rho_{10}$  undetermined. In this case the log likelihood function is

$$W = \sum_{i=1}^N \ln W(\theta_i, \varphi_i).$$

# Topological Code Numbers

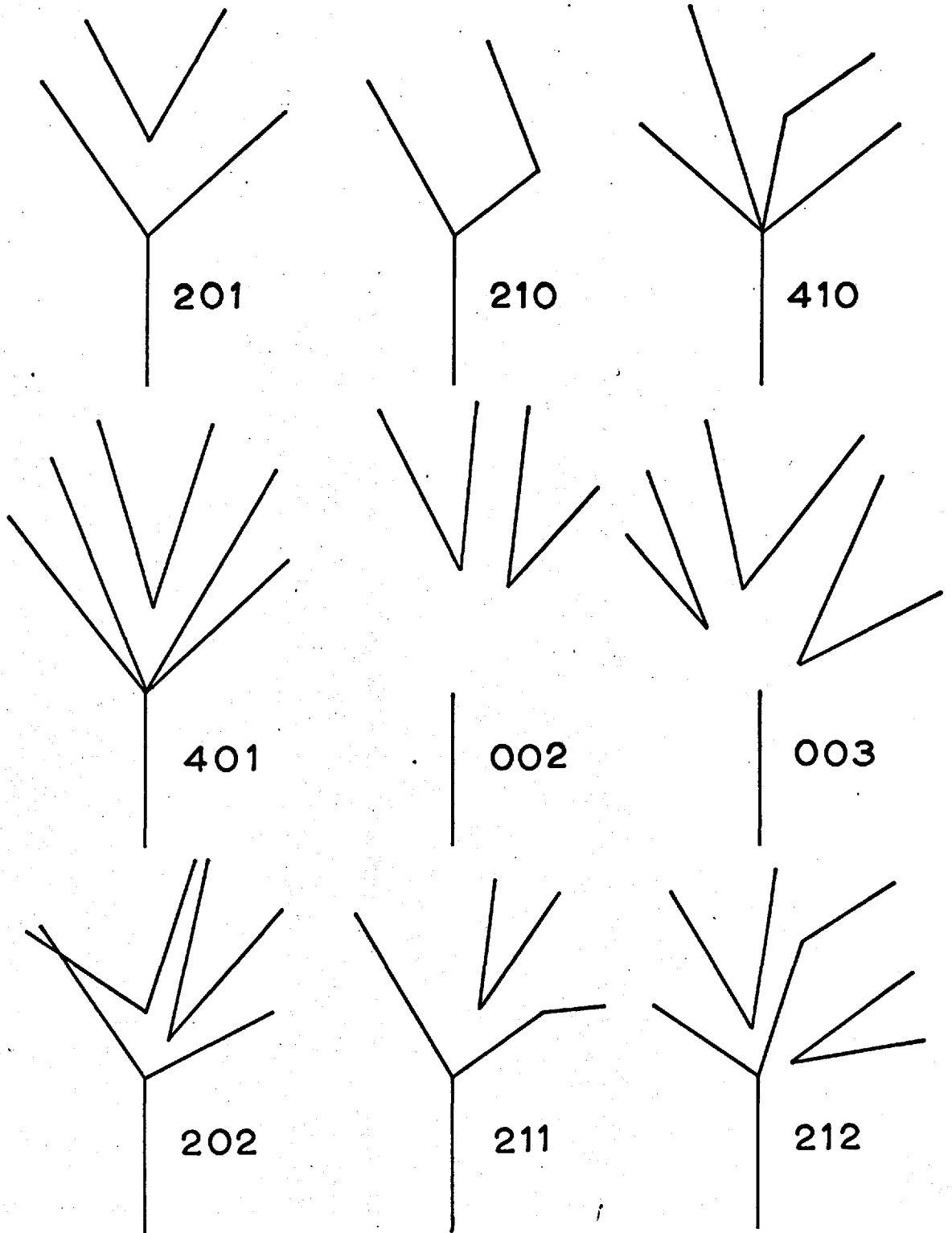


Fig. 3.1

## CHAPTER 4

### BIASES AND BACKGROUND

#### 4.1 The General Approach to Event Classification.

All events which failed to pass through either the tape-to-card conversion programme or the geometry programme were remeasured. At the beginning of the experiment very little was known about the sensitivity of the programmes to the cut-offs imposed on errors. In particular, the influence of large track errors on the extent to which an event would fit, or fail to fit, given hypotheses, was completely unknown. As a result these cut-offs were set high, and a large number of seemingly badly measured events were passed to the fitting programme. In practice it was found that the track errors,  $\sigma_p$ , could be two to three times the standard error,  $\sigma_f$ , without resulting in multiple fits. Experience showed which of the events possessing a geometrical reconstruction needed remeasurement, and these could be returned to the measuring machines before the kinematics output was examined. The advisability of remeasuring events after the kinematics stage is more questionable, but any event with multiple fits, for which few fits could be rejected using the criteria discussed below, were remeasured. Remeasurement was stopped when 95% of the

events were considered to have satisfactory geometry output.

Events in the common topologies were tested against every conceivable hypothesis involving an incoming kaon or pion. This was necessary because hardly any information was available concerning associated production in K and  $\pi$  interactions at high energies. As it turned out, only about a quarter of the total number tried were useful.

For a hypothesis to be selected for consideration the  $X^2$  probability had to be greater than 0.05. The event was then examined on a scanning table and visual agreement required between calculated and observed track ionizations. An event was classed as unambiguous, if one hypothesis had a  $X^2$  probability five times greater than all the others. The remaining events were classified as either multineutral, if this was indicated by the missing mass, or ambiguous when there were several acceptable multivertex fits.

These criteria, when applied to the rare topologies, resulted in almost every event being classed as ambiguous, with the exception of the 002's. The selection of rare events was carried out on the basis of missing mass studies, after certain fits had been rejected as unlikely on the grounds of various "a priori probability" considerations. These criteria, which were different for each channel, are discussed in the

chapter concerned with cross sections. The danger of using the  $X^2$  as the only selection criterion has recently been stressed by F.T. Solmitz<sup>37)</sup>.

#### 4.2 Estimation of the Pion Background.

In experiments at high energies, events caused by pions can very easily simulate those caused by kaons. For this reason the pion contamination in the beam was estimated by comparing the kaon and pion cross section equivalents. The kaon micro-barn equivalent was calculated from the number of  $\tau$  decays seen in scanning and yielded a result of  $0.36 \pm 0.05 \mu\text{b}/\text{event}$ . For the pions, the equivalent was determined from unique fits to pion hypotheses in certain rather prominent channels. In three of the channels chosen, two neutral decays, a  $\Lambda$  and  $K^0$  were observed, and the production missing mass was such as to exclude the possibility of the event being kaon induced. In the fourth, a charged  $\Sigma$  and  $K^0$  were seen in a reaction involving no unseen neutral particles. Cross sections for  $\pi^-$ -proton interactions at 3.5 Gev/c were found by interpolation, using the published results at 2.4, 3, 4 and 4.65 Gev/c. These cross sections could probably be in error by as much as 25%. The results are presented in the table below.

Topology	Channel	$N_{\text{Obs.}}$	$N_{\text{T}}$	$\sigma(\mu\text{b})$	$\mu\text{be}$	$\pi:\text{K}$
002	$\Sigma^0/\Lambda\text{K}^0$	8	43	115	2.5	0.14
002	$\Sigma^0/\Lambda\text{K}^0(\pi\pi^0)$	17	90	220	2.4	0.15
202	$\Sigma^0/\Lambda\text{K}^0\pi^+\pi^-$	6	32	130	4.0	0.09
211	$\Sigma^\pm\pi^\mp\text{K}_1^0$	21	75	120	1.6	0.22

The weighted mean for the  $\pi/\text{K}$  ratio is 0.15. Investigation of other strange particle cross sections in  $\pi^-$  proton interactions leads to the conclusion that the expected contamination from such sources is very small. The most important reactions, when analysing the  $\Sigma^\pm\text{K}_1^0\text{K}_2^0\pi^\mp$  channels, are  $\pi^-p \rightarrow \Sigma^\pm\text{K}_1^0\pi^\mp\pi^0\pi^0$ . Although no data has been presented for the upper limits to the cross sections for these reactions, it is observed that the similar final states  $\Sigma^\pm\text{K}_1^0\pi^\mp\pi^+\pi^-$  have cross sections in this momentum region which are less than  $5\mu\text{b}$ .

#### 4.3 Biases in the Lambda Hyperon Events.

Several checks were made for biases in all channels. The  $X^2$  distributions were compared with their theoretical counterparts and found to be in excellent agreement. Missing mass distributions for most channels, especially those involving neutral K's and charged  $\Sigma$ 's, indicated little, if any, serious

contamination of one final state by another. The stretch functions were plotted and, with one exception (cf. section 4.4), showed no evidence for systematic or badly estimated errors.

From now on the discussion will be restricted to those events of 201 topology for which the neutral decay was classified as a  $\Lambda$ . The main reason for this is that many of the reactions involving zero-hypercharge mesons considered in later chapters, have a  $\Lambda$  and several pions in the final state. The firmly established boson resonances which might be found in the 201's are listed below, in order of increasing mass.

$\eta^0$	$\longrightarrow$	$\pi^+\pi^-\pi^0, \pi^+\pi^-\gamma$
$\rho^0$	$\longrightarrow$	$\pi^+\pi^-$
$\omega^0$	$\longrightarrow$	$\pi^+\pi^-\pi^0, \pi^+\pi^-, \pi^+\pi^-\gamma$
$X^0$	$\longrightarrow$	$\pi^+\pi^-\eta^0, \pi^+\pi^-\gamma, \pi^0\pi^0\eta_c^0$
$\phi^0$	$\longrightarrow$	$\pi^+\pi^-\pi^0(\rho\pi)$
$A1^0$	$\longrightarrow$	$\pi^+\pi^-\pi^0(\rho\pi)$
$B^0$	$\longrightarrow$	$\pi^+\pi^-\pi^0\pi^0(\omega\pi^0)$
$f^0$	$\longrightarrow$	$\pi^+\pi^-$
$A2^0$	$\longrightarrow$	$\pi^+\pi^-\pi^0(\rho\pi)$

In addition, phase space allows several of these resonances to be produced in association with neutral pions. Some of the resonances decay into two kaons, and can therefore occur in the  $\Lambda K^+ K^-$  reaction. These events present an additional separation problem in an already complex situation.

The  $X^2$  distributions for the unambiguous events in the  $\Lambda \pi^+ \pi^- \pi^0$  class (I.C. only) are presented in Fig. 4.1. The upper distribution is for the 3- constraint  $\Lambda$  fits, where the  $\Lambda$  line of flight is fixed by the position of the production apex. The lower  $X^2$  plot is for the 1- constraint production fits. These are 1- constraint because the fit is performed after the vector momentum of the  $\Lambda$  has been determined, leaving only the  $\pi^0$  momentum unknown. The final selection of these events was based on a two vertex fit for which the  $X^2$  distribution (not presented) was also satisfactory.

To test for a possible loss of events in which  $\Lambda$ 's decay close to production, a plot of  $\ln N$  versus  $L/p$  was drawn up, Fig. 4.2, where  $N$  represents the total number of  $\Lambda$ 's present at a given proper time  $\tau$ , for which the length  $L$ , divided by the momentum  $p$ , is a measure. From this graph the true number at  $\tau = 0$  may be obtained by extrapolation and shows that there is a loss of about 8%. A two-dimensional plot of  $L$  versus  $p$  was examined, and demonstrated that the loss

was not noticeably momentum dependent; it represented a depletion in the range of  $L$  from 0 to 5 mms.

Fig. 4.3 is a Gaussian ideogram of the  $\Lambda$  mass, calculated as discussed in section 3.6, and gives some idea of the experimental resolution which can be expected in several of the final states.

#### 4.4 Missing Mass Considerations.

The 3,453 201 events for which the neutral decay fitted as a  $\Lambda$  are included in the distributions discussed below. A study of a sub-set of 661 of these events showed that only 4.4% of the  $V^0$ 's which fitted as  $\Lambda$ 's were subsequently classified, on the basis of ionization, as  $K^0$ 's.

By considering the missing mass<sup>2</sup> distribution alone it was possible to divide the events into several categories. Fig. 4.4 shows clearly the sharp peak around zero caused by the  $\Lambda\pi^+\pi^-$  and  $\Sigma^0\pi^+\pi^-$  events, a broad hump spreading from  $-0.02$  to  $0.08 \text{ Gev}^2$  with which the  $\Lambda\pi^+\pi^-\pi^0$  events may be associated and a continuum starting at  $0.08 \text{ Gev}^2$  which is attributable to the  $\Sigma^0\pi^+\pi^-\pi^0$  and  $\Lambda\pi^+\pi^-(\pi^0)$  events.

At first sight it would appear that the  $\Lambda/\Sigma^0\pi^+\pi^-$  events are ambiguous with  $\Lambda\pi^+\pi^-\pi^0$  events. This is not so, however, for two reasons: (i) the missing momentum in the

former events is seldom greater than 200 Mev/c, (ii) the error on the missing mass<sup>2</sup> for these events is considerably smaller than for the single  $\pi^0$  events. A triple selection of missing mass<sup>2</sup> (-0.01 to 0.01 Gev<sup>2</sup>) error (<0.02 Gev<sup>2</sup>) and missing momentum (<0.2 Gev) was used to extract 95% of the  $\Lambda/\Sigma^0\pi^+\pi^-$  events. The percentage was found by varying the limits and studying the manner in which events were selected or rejected. After these events had been removed (shaded in Fig. 4.4), all the remaining events in the region from -0.02 to 0.08 Gev<sup>2</sup> were considered as belonging to the  $\Lambda\pi^+\pi^-\pi^0$  class. The number and nature of these events was in good agreement with the fitted results. Events above 0.08 Gev<sup>2</sup> were regarded as multineutrals. Fig. 4.5 shows the error distributions for these classes, and indicates schematically the regions in which they occur on an error versus missing mass plot.

Before considering the final problem, that of separating the  $\Lambda\pi^+\pi^-$  and  $\Sigma^0\pi^+\pi^-$  reactions, it is worth noting that the  $\Lambda\pi^+\pi^-(K^0)$ ,  $\Lambda\pi^+K^-(K^0)$ ,  $\Lambda\pi^+\pi^-(\eta^0)$ ,  $\Lambda K^+\pi^-(K^0)$ , channels all give rise to missing masses in the continuum and are virtually inseparable from the multineutral events. Both the reactions  $\Sigma^0\pi^+\pi^-\pi^0$  and  $\Lambda K^+\pi^-\pi^0$  probably give rise to small (~5%) contamination in the  $\Lambda\pi^+\pi^-\pi^0$  events.

Separating  $\Lambda\pi^+\pi^-$  from  $\Sigma^0\pi^+\pi^-$  presented a more formidable problem. Several curious features were found to be associated with the 406 events selected as either  $\Sigma^0$  or  $\Lambda\pi^+\pi^-$ . The missing momentum distribution for these events, Fig. 4.6 shows three peaks. The peak close to zero can be understood from the following considerations. For an event involving no missing particle the expressions,

$$\begin{aligned}\vec{P}_m &= \vec{P}_{in} - \vec{P}_{out} \\ M_m^2 &= (E_{in} - \sum E_{out})^2 - P_m^2 \\ E_{in} &= E_{K^-} + m_p\end{aligned}$$

do not provide the best estimates of the quantities  $P_m$  the missing momentum and  $M_m$  the missing mass<sup>38</sup>). Taking the track errors into account it can be shown that, if the momentum errors dominate, the best estimate for the momentum is given by

$$P_m^{*2} = P_m^2 - \sum_i \Delta p_i^2$$

and for the mass by

$$M_m^{*2} = M_m^2 + \sum_i (1 - \beta_i^2) \Delta p_i^2$$

where  $\beta_i$  is the velocity of the  $i$ th particle and  $\Delta p_i$  its

momentum error. The summation is over all the tracks at the production apex. In the programmes  $P_m^2$  and  $M_m^2$  are calculated, and the experimental distributions for these quantities show the familiar shifts to positive and negative values respectively.

An average momentum error of 10 Mev/c produces a shift of + 20 Mev/c from zero in the missing momentum, which demonstrates that the first peak on the momentum plot is due to the  $\Lambda\pi^+\pi^-$  events. The peak around 80 Mev/c is caused by the  $\Sigma^0\pi^+\pi^-$  events (50% of  $\Sigma^0$  decays give rise to (invariant) transverse momenta >64 Mev/c). This leaves only the intermediate peak to explain.

On a scatter plot of missing mass<sup>2</sup> versus missing momentum<sup>2</sup> it was noticed that a clustering of events occurred along the line  $P_m^2 = -M_m^2$ , and that this clustering was most intense in the region of  $P_m$  associated with the second peak. The events in the three bands centred on the peaks were investigated separately. A missing mass to the two pions was calculated and plotted for the events in each group, Fig. 4.7. As expected both the  $\Lambda$  and  $\Sigma^0$  can be distinguished on these plots, but for the events associated with the intermediate values of  $P_m$  a considerable displacement towards low mass values is observed. This effect can be explained if a systematic

error of  $-20 \text{ Mev}/c$  occurred in the estimated beam momentum for these events. This also explains the clustering along  $P_m^2 = -M_m^2$  since  $P_m$  is more sensitive than  $E_m$  (the missing Energy) to an error in the beam momentum.

The division between  $\Lambda\pi^+\pi^-$  and  $\Sigma^0\pi^+\pi^-$  was made by selecting events from bands on the momentum plot and using a variable cut-off on the ' $\Lambda\gamma$ ' mass. This resulted in 246  $\Lambda\pi^+\pi^-$  and 160  $\Sigma^0\pi^+\pi^-$  being selected with estimated contaminations of less than 10% in both cases.

The events with the wrongly assigned beam momentum were found to belong mainly to the second of the bubble chamber exposures. As a final check on this error the beam momentum stretch function was plotted, Fig. 4.8, for unambiguous events involving no neutral particles. The systematic error is apparent from this distribution. An error of  $20 \text{ Mev}/c$  (this corresponded to a single standard deviation) is not serious enough to result in a loss of fits, and certainly does not give rise to excessive shifts in effective masses. The extent to which stretch functions provide important information concerning the beam momentum can hardly be over emphasized.

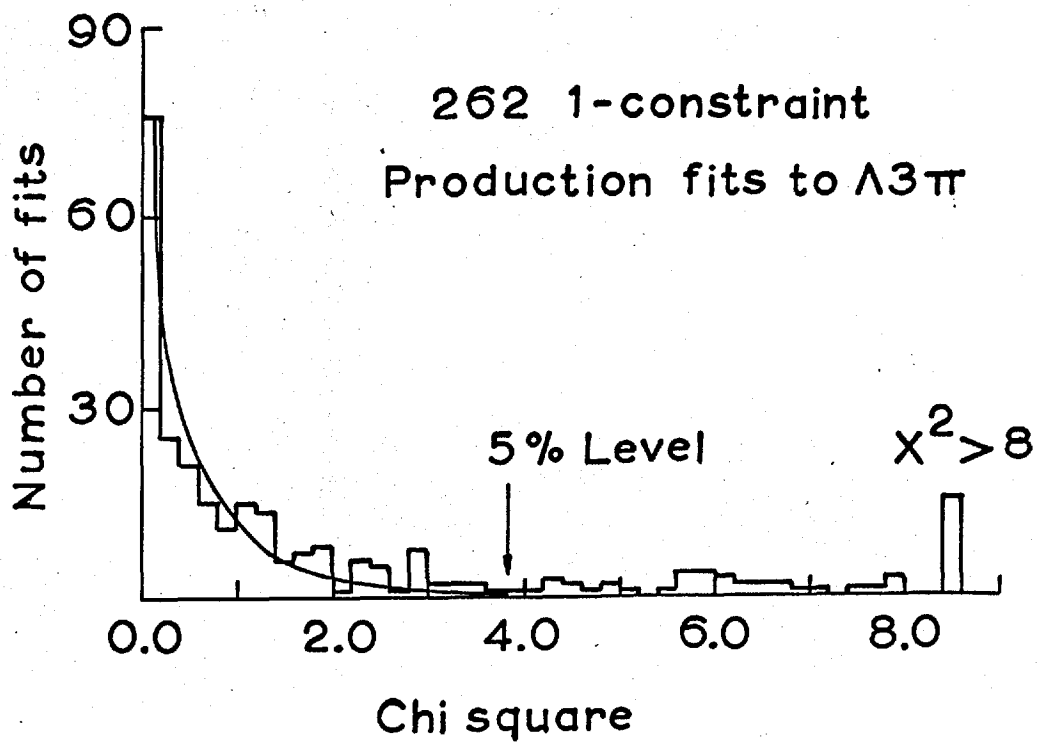
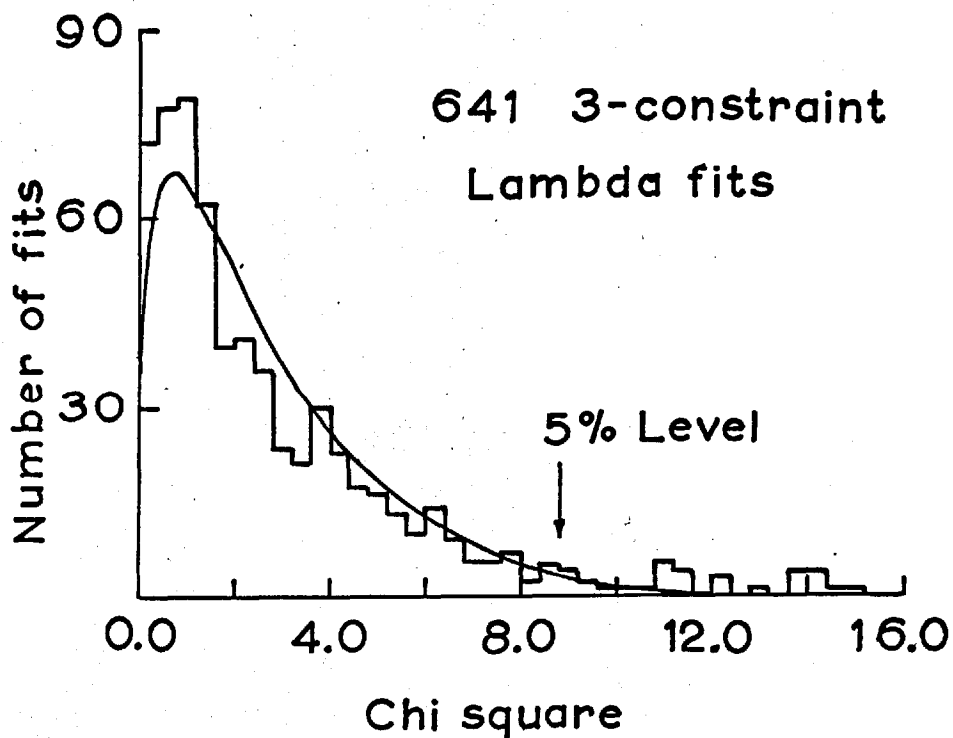
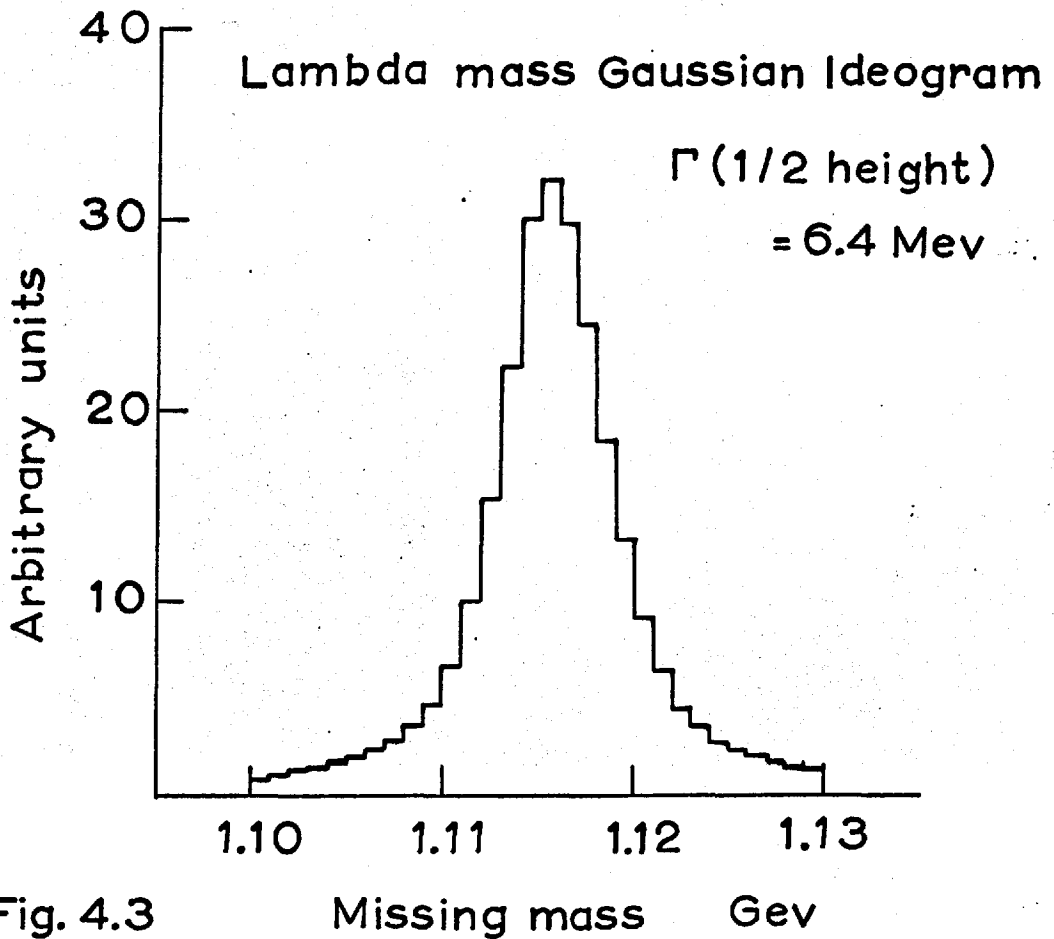
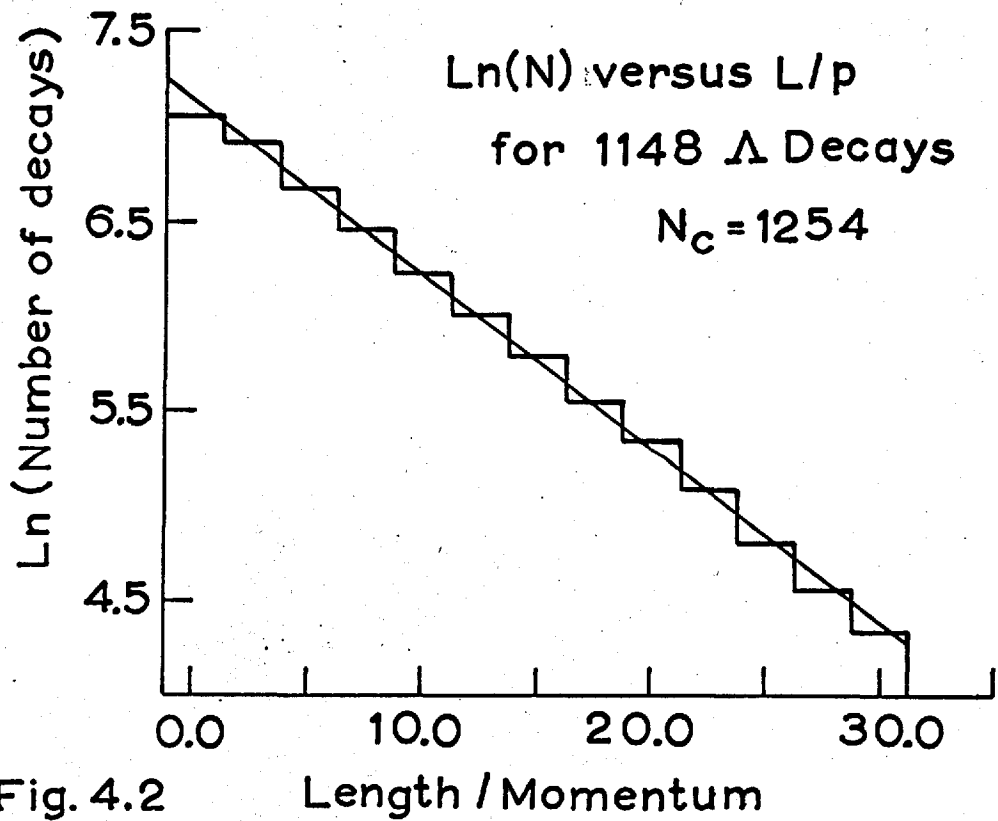


Fig. 4.1



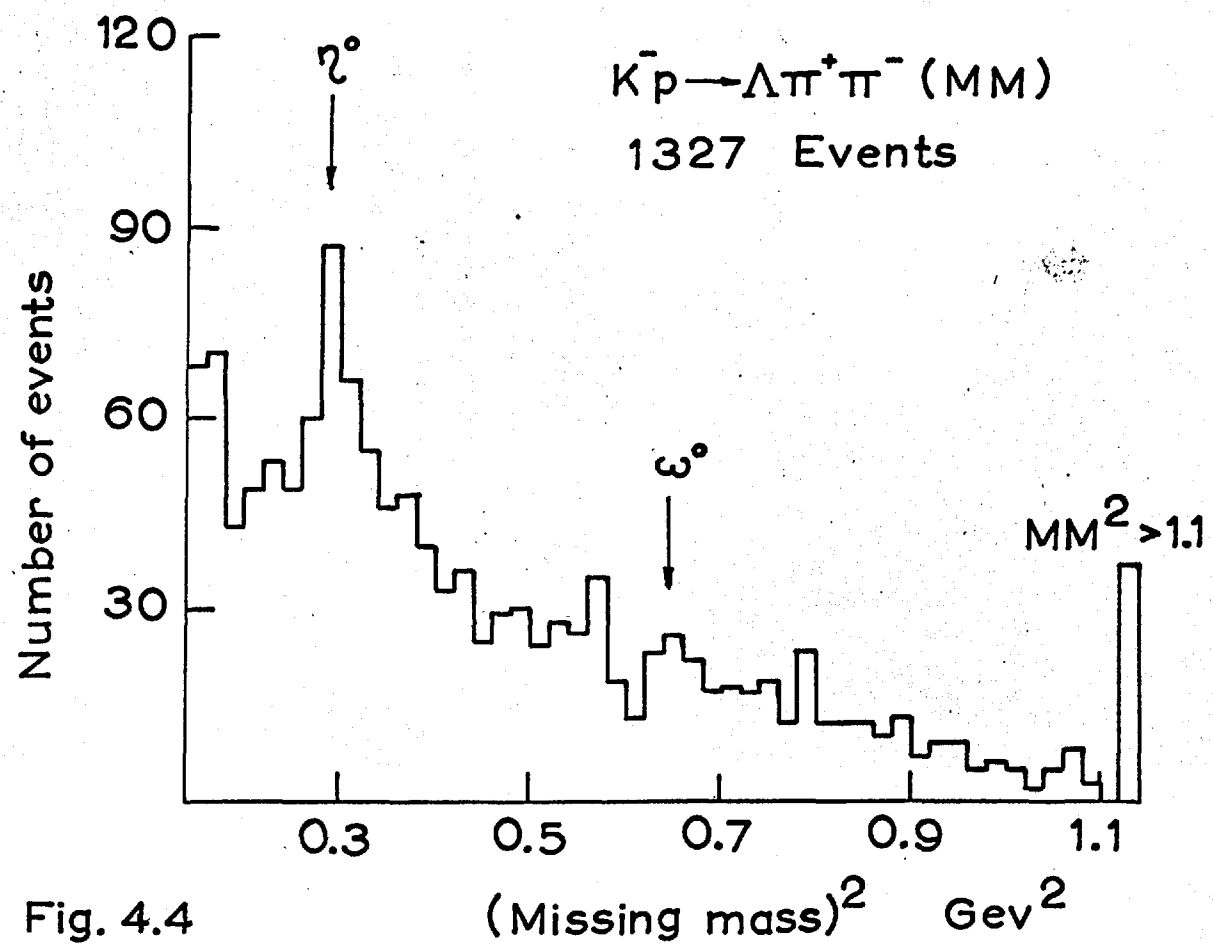
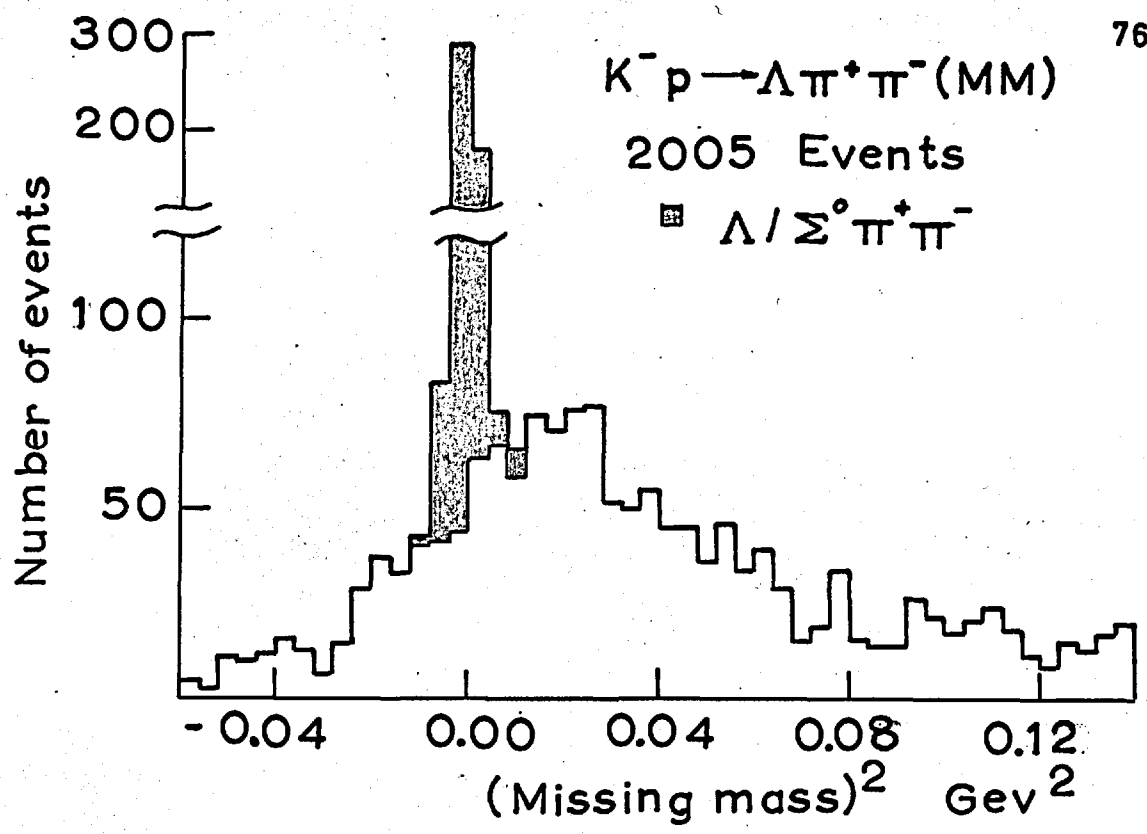
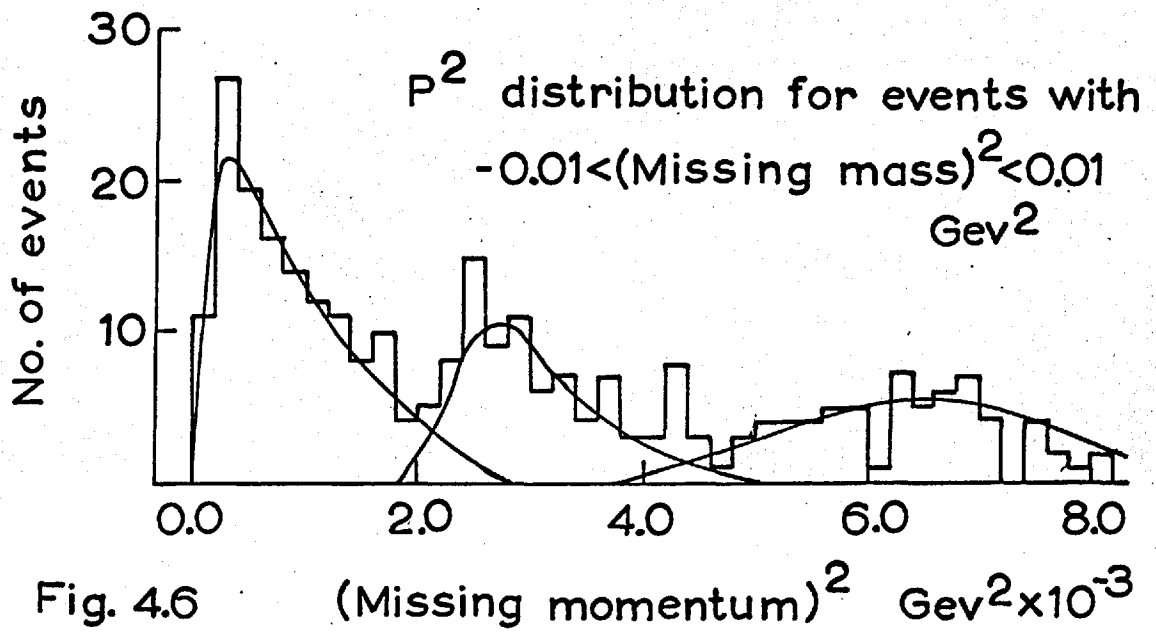
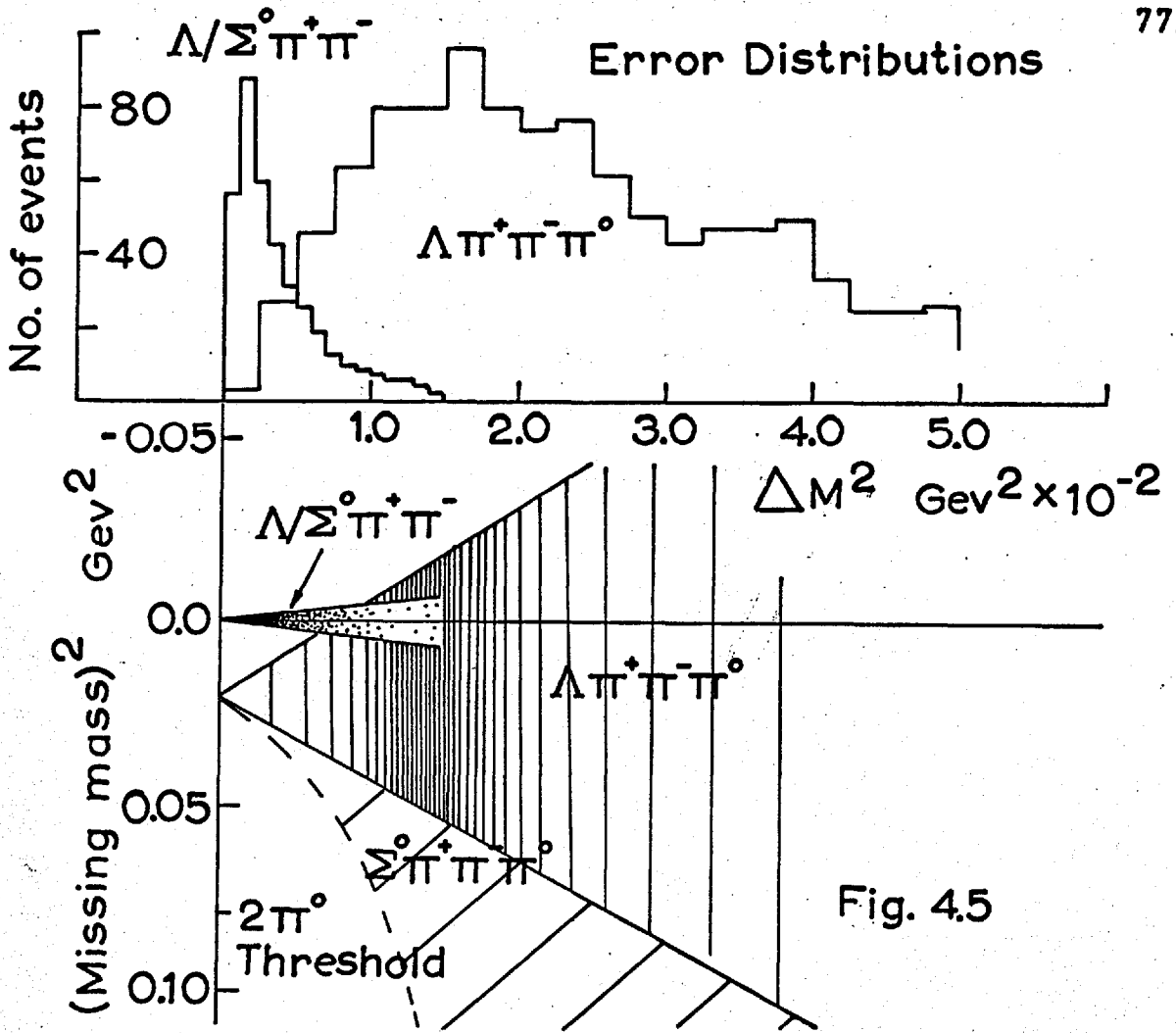


Fig. 4.4



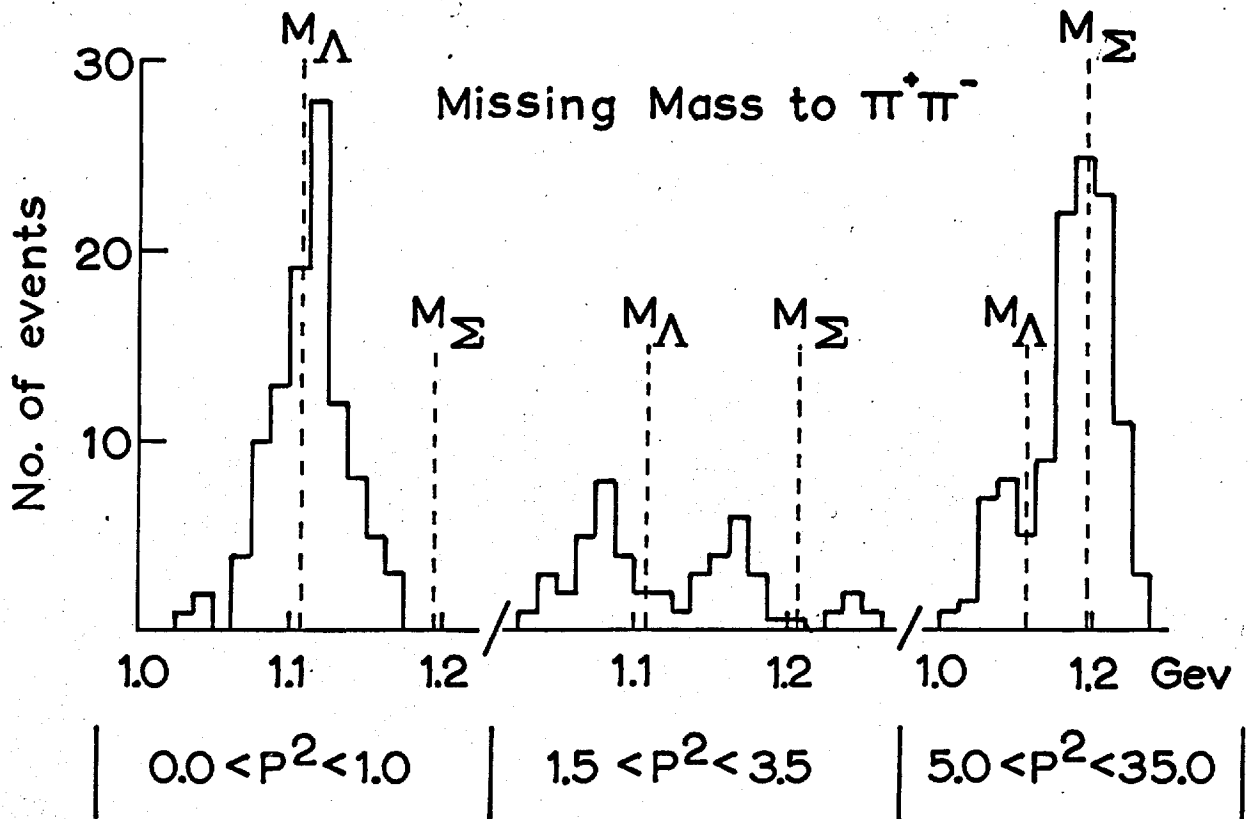


Fig. 4.7  $P^2 = (\text{Missing Momentum})^2 \times 10^3 \text{ Gev}^2$

Momentum Stretch  
Function for Beam  
Track

68 Unambiguous  
Fits (no neutrals)

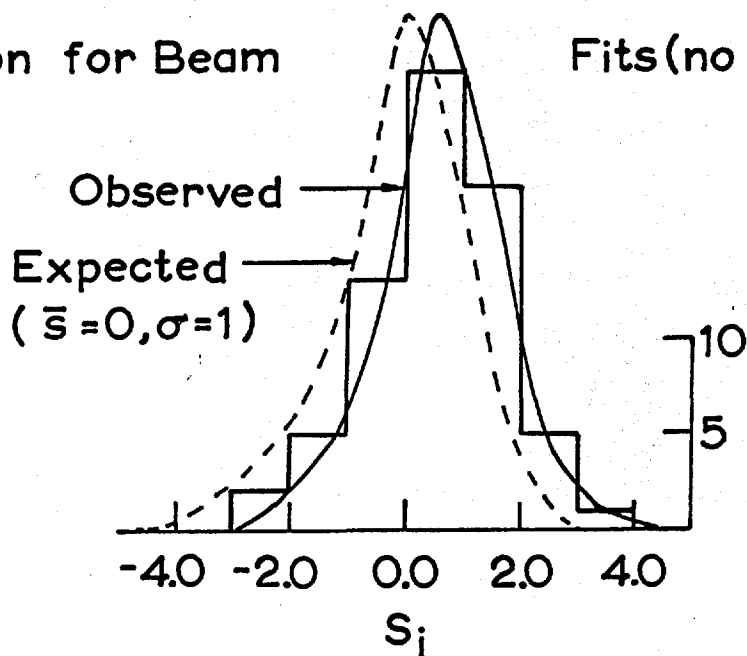


Fig. 4.8

CHAPTER 5  
TOTAL CROSS SECTIONS

5.1 Detection Efficiency

The correct method for adjusting angular distributions, to take into account the losses due to scanning, measuring and finite chamber size, has recently been considered by F.T. Solmitz<sup>37)</sup>. The alternative of using individual weights for the events leads to a slight loss of information, but is the only practical procedure in view of the complexity of strange particle events.

For the  $K^0$  and  $\Lambda$  events the following expression was used for the weights  $w$ ,

$$1/w = \exp(-l_p/(p\tau/m)) - \exp(-L_p/(p\tau/m))$$

where  $\tau$ ,  $p$  and  $m$  are the mean life, momentum and mass of the  $V^0$  and  $c$  is the velocity of light  $l_p$  is the lower limit on the decay length at which a  $V^0$  can be distinguished from normal production tracks and  $L_p$  is the potential length for the decay, defined as the distance along the  $V^0$  direction from the production point to the edge of the fiducial volume.

For the charged  $\Sigma$ 's, empirical expressions, based on a careful study of a sample of observed decays, were derived by J.G. Loken<sup>39)</sup>. These expressions, which were

different for the  $\Sigma^+$  and  $\bar{\Sigma}$  and were dependent on the momentum, were included in the Statistics programme by J.M. Scarr.

The average weights for the various strange particle decays were found to be

$\Lambda$	1.15
$K^0$	1.10 (4 body events only)
$\Sigma^+$	1.56
$\Sigma^-$	1.25

These weights were used to correct the associated production cross sections given in section 5.4.

## 5.2 Cross section Calculations

The cross section for a channel where N events are observed is given by

$$\sigma = (1/A\rho_H L)N \quad \text{cm}^2$$

A : Avogadro's number,  $6.025 \times 10^{23}$

$\rho_H$ : Density of hydrogen under operating conditions,  
 $6.25 \times 10^{-2} \text{ gm/cm}^3$

L : Total track length of kaons involved.

The cross section determination depends on a knowledge of  $N_0$ , the total number of kaons entering the chamber and l, the length of the fiducial volume. The number of decaying

kaons is given by

$$N_D = f N_0 (1 - \exp [-l/(pc\tau/m)])$$

in which  $\tau$  is the mean life,  $m$  the mass and  $p$  the momentum of the kaon and  $c$  is the velocity of light.  $f$  is a factor which allows for the loss of beam track through interaction ( $f=0.98$ ).

Since the exponent in this expression is very small  $N_D$  may be approximated by

$$N_D = f N_0 l / (pc\tau/m)$$

$$\text{and } L = f N_0 l = N_D (pc\tau/m)$$

The total number of decays is obtained from the observed number of  $\tau$  decays,  $N_\tau$ . Only  $5.8 \pm 0.3\%$  of the  $K^-$  decays involve 3 charged particles, therefore,

$$N_D = N_\tau / (0.058 \pm 0.003) = (17.3 \pm 0.9) N_\tau$$

Defining the micro-barn equivalent  $\mu$ , such that

$$\sigma = \mu N$$

gives the cross section in micro-barns, then

$$\mu = 10^{30} / A_0 H N_D (pc\tau/m)$$

$$= 2090 / N_\tau p \quad \mu\text{barns/event} \quad \text{with } p \text{ in GeV}/c$$

For the Imperial College film,  $N_\tau = 233$  in a 42cm. fiducial volume. This gives, with  $p = 3.46 \text{ GeV}/c$

$$\mu = 2.6 \pm 0.6 \mu\text{barns/event}$$

### 5.3 Single Strange Particle Channels.

The cross sections for these channels are listed in Table 2, together with the observed and corrected numbers of events involved. The corrections applied were as follows :

- i) Addition of 5% to allow for scanning loss;
- ii) a weighting factor as given in section 5.1;
- iii) a factor of  $\sim 3$  in the  $K^0$  channels to allow for the  $K_2^0$  (50%) and neutral  $K_1^0$  (15.3%) decays;
- iv) a factor of  $\sim 3/2$  in the  $\Lambda$  channels to allow for the  $\Lambda \rightarrow n\pi^0$  (31.6%) decays.

In some cases an additional correction has been made to allow for the events which were ambiguous after the ionization and  $X^2$  probability criteria discussed in section 4.1 had been applied. In most channels the losses and contaminations are expected to be less than 10%.

One notable feature is the high cross section for the production of multineutrals in the  $\Lambda$ -201 topology. A possible explanation is given in chapter 6.

### 5.4 Associated Production Channels.

All the reactions to be considered in this section involve two kaons in the final state. An additional complication arises, in the cross section calculations,

when two neutral kaons are produced. A system consisting of such kaons is in general a mixture of two components of opposite C-parity<sup>40</sup>). When the production mechanism results in a statistical mixture of these two components being present in equal proportions (i.e. when  $K^0\bar{K}^0$  is produced), 50% of the decays occur via  $K_1^0 K_2^0$ , 25% via  $K_1^0 K_1^0$  and the remaining 25% via  $K_2^0 K_2^0$ . The relative rates of decay of a  $K_1^0$  into  $\pi^+\pi^-$  and  $\pi^0\pi^0$  are in the ratio 2:1, which means that only 2/3 of the  $K_1^0 K_2^0$  decay of the  $K^0\bar{K}^0$  system is seen as  $K_c^0(K^0)$ . (Here,  $K_c^0 \Rightarrow K_1^0 \rightarrow \pi^+\pi^-$ , and  $(K^0) \Rightarrow K_1^0 \rightarrow \pi^0\pi^0$  or a  $K_2^0$  decay.) Of the  $K_1^0 K_1^0$  contribution 4/9 (= 2/3 x 2/3) is seen in the chamber as  $K_c^0 K_c^0$ ; another 4/9 (= 2 x 2/3 x 1/3) simulates the  $K_1^0 K_2^0$  component by decaying  $K_c^0(K^0)$ . If  $N$   $K^0\bar{K}^0$  pairs are produced they will be observed in the chamber as follows:

$$N_{11} = \frac{4}{9} \times \frac{N}{4}$$

$$N_{12} = \frac{4}{9} \times \frac{N}{4} + \frac{2}{3} \times \frac{N}{2}$$

$N_{11}$  is the no. of events with two visible  $K^0$  decays  $N_{12}$  is the no. of events with a single visible  $K^0$  decay. For equal amounts of the  $C = +1$  and  $C = -1$  components we have

$$N_{12} = 4 N_{11} = \frac{4}{9} N$$

If this relationship is not satisfied for a given channel, one of the components must occur with greater frequency than the other. This can happen if a neutral, zero hypercharge resonance is being produced, which undergoes a C-parity conserving (strong) decay into two  $K^0$ 's. For a  $C = -1$  resonance only decay into  $K_1^0 K_2^0$  is allowed and any excess of  $N_{12}$  over  $4N_{11}$  would reflect the presence of such a resonance.

In fact, in all the  $K^0 \bar{K}^0$  processes observed in the present experiment this inequality occurs, and abundant production of the  $C = -1$ ,  $\phi$  meson is apparent from the  $K\bar{K}$  effective mass distributions (cf. chapter 6).

If in addition to  $N$   $K^0 \bar{K}^0$  pairs,  $N'$  examples of  $\phi$  meson production occur, the relationship between  $N_{11}$  and  $N_{12}$  becomes,

$$N_{12} = 4 N_{11} + \frac{2}{3} N'$$

In Table 3 the observed numbers of  $K_1^0 K_1^0$  and  $K_1^0 (K^0)$  are presented for the reactions involving  $\Lambda$  or  $\Sigma$  hyperons.  $N_{11}$  and  $N_{12}$  are calculated from these numbers using the weights for the  $\Lambda$ ,  $K^0$  and  $\Sigma$  given in section 5.1 and the branching ratio for the  $\Lambda$  decay. Column 5 contains the  $N'$  defined above, apart from a factor of  $3/2$ . The final column lists the  $\phi(K_1^0 K_2^0)$  cross sections calculated from  $N' \times \mu\text{be}$ .

These cross sections are in excellent agreement with the cross sections given in chapter 6.

The total cross sections are presented in Table 4. For the  $K^0\bar{K}^0$  reactions these are obtained by multiplying  $(9 N_{11} + N')$  into the micro-barn equivalent. The selection criteria for the associated production events are given in Table 5.

(N.B. reactions involving both incoming pions and kaons are included in this table in the ambiguity and contamination columns).

TABLE 2

Channel	N(Observed)	N(Corrected)	Cross Section (mb)
$\bar{K}^0 p \pi^-$	339	1191	$0.875 \pm 0.049$
$\bar{K}^0 p \pi^- \pi^0$	472	1554	$1.120 \pm 0.064$
$\bar{K}^0 n \pi^+ \pi^-$	474	1542	$1.137 \pm 0.065$
$\bar{K}^0 p \pi^- \pi^+ \pi^-$	108	117	$0.216 \pm 0.021$
$\bar{K}^0 p \pi^- \pi^+ \pi^- \pi^0$	43	47	$0.089 \pm 0.014$
$\bar{K}^0 n \pi^+ \pi^- \pi^+ \pi^-$	18	21	$0.053 \pm 0.010$
$\Lambda \pi^+ \pi^-$	236	407	$0.280 \pm 0.030$
$\Lambda \pi^+ \pi^- \pi^0$	1107	1916	$1.382 \pm 0.063$
$\Lambda \pi^+ \pi^- (n \pi^0)$	1510	2588	$2.180 \pm 0.110$
$\Lambda \pi^+ \pi^- \pi^+ \pi^-$	142	248	$0.163 \pm 0.013$
$\Lambda \pi^+ \pi^- \pi^+ \pi^- \pi^0$	210	359	$0.245 \pm 0.015$
$\Lambda \pi^+ \pi^- \pi^+ \pi^- (n \pi^0)$	112	195	$0.135 \pm 0.014$
$\Sigma^0 \pi^+ \pi^-$	170	294	$0.212 \pm 0.026$
$\Sigma^0 \pi^+ \pi^- \pi^+ \pi^-$	67	118	$0.079 \pm 0.009$
$\Sigma^+ \pi^-$	69	107	$0.141 \pm 0.012$
$\Sigma^+ \pi^- \pi^0$	368	597	$0.347 \pm 0.018$
$\Sigma^+ \pi^- \pi^+ \pi^-$	200	318	$0.162 \pm 0.012$
$\Sigma^+ \pi^- \pi^+ \pi^- \pi^0$	285	438	$0.250 \pm 0.012$
$\Sigma^- \pi^+$	13	22	$0.011 \pm 0.003$
$\Sigma^- \pi^+ \pi^0$	247	318	$0.183 \pm 0.013$
$\Sigma^- \pi^+ \pi^- \pi^+$	188	237	$0.140 \pm 0.006$
$\Sigma^- \pi^+ \pi^- \pi^+ \pi^0$	243	300	$0.186 \pm 0.005$

TABLE 3

Channel	No. of $K_1^0 K_1^0$	No. of $K_1^0 (K^0)$	$N_{11}$	$N_{12}$	$N_{12} - 4N_{11}$	$\sigma(\varphi - K_1^0 K_2^0)$ $\mu\text{b}$
$\Lambda K^0 \bar{K}^0$	14	56	16.8	106.2	39.0	17.5
$\Sigma^0 K^0 \bar{K}^0$	5	22	6.4	42.0	16.4	7.4
$\Sigma^0 / \Lambda K^0 \bar{K}^0 \pi^0$	3	47	5.4	89.3	67.7	30.4
$\Sigma^+ K^0 \bar{K}^0 \pi^-$	2	16	3.8	27.4	12.2	5.5
$\Sigma^- K^0 \bar{K}^0 \pi^+$	2	27	3.0	37.5	25.4	11.4

TABLE 4

Channel	N(Observed)	N(Corrected)	Cross Section (mb)
$\Lambda K^0 \bar{K}^0$	68	212	$0.063 \pm 0.021$
$\Lambda K^+ K^-$	57	98	$0.065 \pm 0.013$
$\Sigma^0 K^0 \bar{K}^0$	27	82	$0.025 \pm 0.008$
$\Sigma^0 K^+ K^-$	30	56	$0.036 \pm 0.014$
$\Sigma^+ K^- K^0$	5	26	$0.008 \pm 0.006$
$\Sigma^- K^+ \bar{K}^0$	11	44	$0.013 \pm 0.008$
$\Sigma^0/\Lambda K^0 \bar{K}^0 \pi^0$	50	150	$0.045 \pm 0.009$
$\Sigma^0/\Lambda K^+ K^- \pi^0$	58	100	$0.067 \pm 0.014$
$\Sigma^0/\Lambda K^+ \bar{K}^0 \pi^-$	9	52	$0.016 \pm 0.008$
$\Sigma^0/\Lambda K^- K^0 \pi^+$	18	108	$0.031 \pm 0.012$
$\Sigma^+ K^0 K^- \pi^0$	1	5	$0.001 \pm 0.002$
$\Sigma^- \bar{K}^0 K^+ \pi^0$	3	12	$0.004 \pm 0.004$
$\Sigma^+ K^0 \bar{K}^0 \pi^-$	18	53	$0.016 \pm 0.006$
$\Sigma^- K^0 \bar{K}^0 \pi^+$	27	65	$0.020 \pm 0.007$
$\Sigma^+ K^+ K^- \pi^-$	14	22	$0.013 \pm 0.006$
$\Sigma^- K^+ K^- \pi^+$	12	15	$0.009 \pm 0.005$

TABLE 5

Selection Criteria for Associated Production Events

Final State	Missing Mass Limits		Ambiguity - Contamination - Loss
	Lower	Upper	
$\Lambda K_1^0 K_1^0$	1.100	1.130	Missing mass limits imposed in 002's because of background from $K_1^0 K_1^0 \pi^0$ .
$\Lambda K_1^0 K_2^0$	0.447	0.547	Missing mass limits (cf. Fig. 5.1) introduced to reduce contamination from $\Lambda K^0 \pi^0 \pi^0$ and $\Sigma^0 K_1^0 K_2^0$ . Loss < 10%
$\Sigma^0 K_1^0 K_1^0$	1.175	1.205	$\Lambda K \bar{K}$ well separated from $\Sigma^0 K \bar{K}$ in 003's but not in 002's, cf. section 4.4.
$\Sigma^0 K_1^0 K_2^0$	0.547	0.650	Missing mass limits introduced after 'Ky' mass plot for $\Sigma^0 K^+ K^-$ examined. Loss < 20%
$\Lambda K^+ K^-$	-0.100	0.100	Separation of $\Sigma^0$ and $\Lambda K^+ K^-$ accomplished as for $\Sigma^0 / \Lambda \pi^+ \pi^-$ . No. of $\Lambda K \bar{K}$ fits (55) agrees well with no. selected using this method (57)
$\Sigma^0 K^+ K^-$	-0.100	0.100	Both the $\Sigma^0$ and $\Lambda K^+ K^-$ events were very ambiguous with 1-C fits of type $\Lambda 3\pi$ , $\Lambda K^+ \pi^0 \pi^0$ etc.
KKKN	-	-	1 example of $K_1^0 K_2^0 K_1^0 n$ identified. 5 possible $K_1^0 K_1^0 K_2^0 n$ on basis of missing mass. Other 3KN final states impossible to identify

TABLE 5 contd.

Selection Criteria for Associated Production Events

Final State	Missing Mass Limits		Ambiguity - Contamination - Loss
	Lower	Upper	
$\Sigma^0/\Lambda K_1^0 K_1^0 \pi^0$	-	-	3 fits to $\Lambda K_1^0 K_1^0 \pi^0$ . A single 003 had a missing mass consistent with $\Sigma^0 K_1^0 K_1^0 \pi^0$
$\Sigma^0/\Lambda K_1^0 K_2^0 \pi^0$	0.650	-	No 5-body $\Lambda K K \pi \pi$ fits obtained in 401's and 202's. Assume none in 002's. $\Sigma^0 K_1^0 K_2^0$ contamination <20%
$\Sigma^0 K^0 K^{\pm} \pi^{\mp}$ $\Lambda$	-	-	Many 202's fitted both $\Sigma^0 K K \pi$ and $\Lambda K K \pi$ -separation impossible. Slight ambiguity (20%) with $\Sigma^0/\Lambda K^+ \pi^+ \pi^-$
$\Sigma^0 K^+ K^- \pi^0$ $\Lambda$	-0.140	0.280	Kin. Programme gave many pseudo fits, with momentum of $\pi^0 < 0$ . -mainly misinterpreted $\Sigma^0 \pi \pi$ and $\Lambda K^+ \pi^-$ events
$\Sigma^+ K^+ K^0$	-	-	Few fits obtained. About 30% ambiguous with $\Sigma^+ \pi^+ K^0$ . 210 events not used.
$\Sigma^+ K^+ K^0 \pi^0$	-	-	15 fits, some of which were classified as $\Sigma K_1^0 K_2^0 \pi^0$ on basis of ionization
$\Sigma^+ K_1^0 K_1^0 \pi^+$	-	-	No ambiguity with $\Xi^-$ events involving incoming kaons or pions
$\Sigma^+ K_1^0 K_2^0 \pi^+$	0.450	-	All $K^+$ decay fits rejected as $NvL/p$ plot 1000 x too steep. No ambiguity with $\Xi^-$ events. Missing mass (Fig. 5.2) shows clean $K^0$ peak
$\Sigma^+ K^+ K^- \pi^+$	-	-	Events ambiguous with 1-C fits to commoner hypotheses. All 4-C fits accepted. Occasionally ionization favoured 2K hypothesis

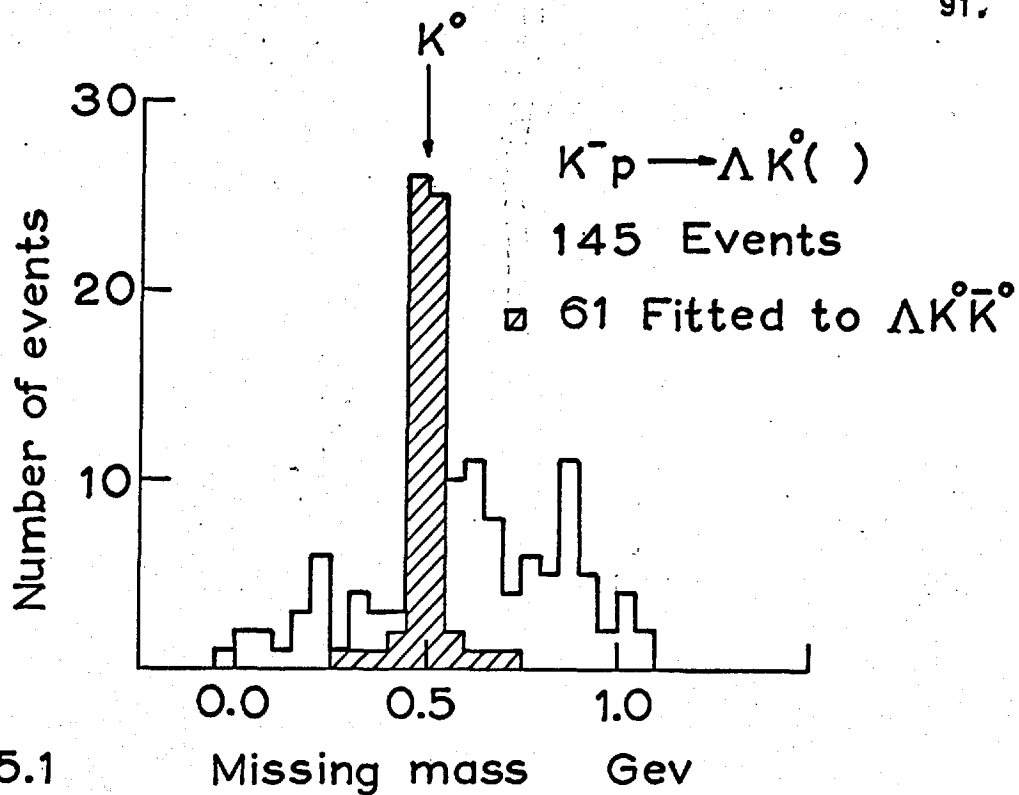


Fig. 5.1

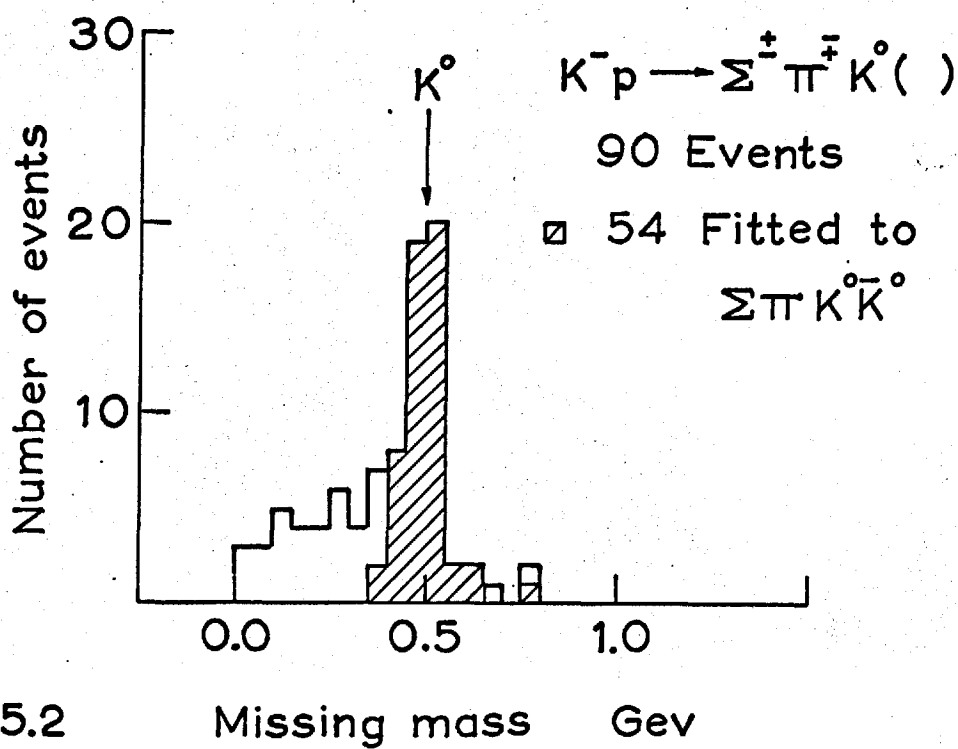


Fig. 5.2

CHAPTER 6

PRODUCTION OF THE  $\rho^0$ ,  $\omega^0$  AND  $\phi^0$  MESONS

6.1 Introduction.

The charge and hypercharge of the  $K^-$ - proton system are both zero. From the conservation of these quantum numbers the  $\rho^0$ ,  $\omega^0$  and  $\phi^0$  mesons can only be produced in association with the following :

$$\begin{array}{ll} pK^- & n\bar{K}^0 \\ p\bar{K}^0\pi^- & nK^-\pi^+ \end{array}$$

$$\Sigma^+\pi^- \quad \Sigma^0/\Lambda \quad \Sigma^-\pi^+$$

$$\begin{array}{ll} E^0K^0 & E^-K^+ \\ E^0K^+\pi^- & E^-K^0\pi^+ \end{array}$$

Additional  $\pi^0$ 's and  $\pi^+\pi^-$  pairs can be added if allowed by the available phase space.

A few general points need to be made about the distributions presented in this chapter and chapter 7:

- 1) the resonance cross sections were obtained using a maximum likelihood method to fit Breit-Wigner + phase space distributions to the effective mass histograms,

- except in the  $\phi$  meson channels where the cross sections were obtained by counting;
- 2) the phase space curves presented on the plots are normalised to the fraction of events which do not involve the resonance under consideration;
  - 3) the angular distributions have been weighted to allow for losses, these being most important in the centre of mass system (C.M.S.) angular distributions;
  - 4) all masses are quoted in natural units (i.e.  $\hbar$  and  $c$  are taken equal to unity).

## 6.2 Production in association with a $\Lambda$ Hyperon.

### Two Body Reactions.

The Dalitz plots for the three body final states  $\Lambda\pi^+\pi^-\bar{K}$  and  $\Lambda K\bar{K}$ , Fig. 6.1, show strong production of the  $\rho^0$  and  $\phi^0$  resonances. A clean separation of the  $\rho^0$  is made difficult by the presence of a strong competing  $Y_1^{*+}$  (1385) in the  $\Lambda\pi^+\pi^-$  channel. In the  $\Lambda K\bar{K}$  reaction there is no evidence for the production of  $N^*$  ( $\rightarrow\Lambda K$ ) or  $E^*$  ( $\rightarrow\Lambda\bar{K}$ ) resonances. The  $E^*$  (1820) reported by Smith et al. <sup>41)</sup> at 2.6 GeV/c does not appear to be produced strongly at 3.5 GeV/c <sup>42)</sup>. The effective mass plots, Fig. 6.2, show that the  $\omega^0$  and  $\phi^0$  are both fairly free of background. The production cross

sections for all three reactions are listed below.

Resonance	Final State	Cross section ( $\mu\text{b}$ )
$\rho^0$	$\Lambda\pi^+\pi^-$	$78_{\pm 15}$
$\omega^0$	$\Lambda\pi^+\pi^-\pi^0$	$95_{\pm 15}$
$\phi^0$	$\Lambda K_1^0 K_2^0$	$19_{\pm 5}$
$\phi^0$	$\Lambda K^+ K^-$	$18_{\pm 5}$

All losses have been taken into account when calculating these cross sections. The total cross section for  $\phi^0$  production is greater than the sum of the two contributions given above since the  $\phi^0$  is believed to decay into  $\pi^+\pi^-\pi^0$  also. The branching ratio into this channel is difficult to determine from the  $\pi^+\pi^-\pi^0$  effective mass distribution but is probably  $\frac{1}{3}$  of the total  $K\bar{K}$  contribution.

The production angular distributions in the centre of mass are shown in Fig. 6.3. These distributions seem to indicate that the production mechanisms in the  $\omega^0$  and  $\phi^0$  channels are considerably different. This point is taken up again in chapter 8. The resonance decay angles  $\theta$  and  $\varphi$  (cf. Fig. 6.4), for the low momentum transfer events, have been used to obtain the following set of density matrix elements :

Res.	Effective Mass Range	$\Delta^2$ cut-off. (Gev) <sup>2</sup>	$\rho_{00}$	$\rho_{1-1}$	$\text{Re} \rho_{10}$
$\rho^0$	0.66-0.86	0.8	$0.18 \pm 0.12$	$-0.13 \pm 0.11$	$-0.09 \pm 0.08$
$\omega^0$	0.74-0.80	0.7	$0.28 \pm 0.14$	$0.15 \pm 0.10$	$-0.08 \pm 0.07$
$\phi^0$	1.01-1.03	0.7	$0.39 \pm 0.10$	$0.07 \pm 0.09$	$-0.01 \pm 0.03$

Vector exchange appears, at first sight, to be the dominant production mechanism in all of the channels. As mentioned in chapter 1, consideration of the effect of absorption can modify this conclusion (cf. chapter 8).

Fig. 6.5 shows the  $\theta$  and  $\phi$  distributions for the  $\rho^0$  and  $\omega^0$  events produced in the backward direction in the centre of mass. Baryon exchange has been taken as the production mechanism for the calculation of these angles. There are too few events for useful density matrix elements to be presented.

Finally, the polarization of the  $\Lambda(P_\Lambda)$  has been examined for the backward and forward events in each of the channels. Distributions for the cosine of the angle  $\theta'$ , which the decay proton in the  $\Lambda$  centre of mass makes with respect to the normal to the production plane, are given in Fig. 6.6. The product  $\alpha P_\Lambda$ , given by

$$\alpha P_{\Lambda} = 3/N \sum_{i=1}^N \cos \theta'_i$$

is presented on each graph.  $\alpha$  is the  $\Lambda$  decay asymmetry parameter ( $-0.62 \pm 0.07$ ). All the values of  $P_{\Lambda}$  are small and are probably consistent with zero. There is no correlation, in any channel, between the decay of the  $\Lambda$  and the decay of the vector meson.

### Three Body Reactions.

The  $\pi^+\pi^-$  effective mass distribution, Fig. 6.7a, in the  $\Lambda\pi^+\pi^-\pi^0$  channel shows slight evidence for  $\rho^0$  production. A prominent  $\phi^0$  is produced in the  $\Lambda K^+K^-\pi^0$  reaction, however, as can be seen from the  $K^+K^-$  mass plot of Fig. 6.7b. No information concerning  $\Lambda\omega^0\pi^0$  can be presented because two neutral pions are involved in this final state. Similarly the  $\phi^0$  decay into  $K_1^0K_2^0$  cannot be studied, but it is to be noted that there are sufficient multineutral  $\Lambda K_1^0$  events in the 002's to account for this decay mode

Channel	Cross section ( $\mu\text{b}$ )
$\Lambda\rho^0\pi^0$	$60 \pm 10$
$\Lambda\phi^0\pi^0$	$24 \pm 10$

The  $K_1^0K_2^0$  decay of the  $\phi$  has been taken into account in the cross section presented above.

The following upper limits can be placed on the production of the  $\rho^0$  and  $\phi^0$  in association with a  $Y_1^{*0}$  (1385) at 3.5 Gev/c.

$$\sigma(Y_1^{*0}(1385)\rho^0) < 15\mu\text{b} \quad \sigma(Y_1^{*0}(1385)\phi^0) < 6\mu\text{b}$$

### Multiparticle Final States.

The  $\pi^+\pi^-$  and  $\pi^+\pi^-\pi^0$  effective mass plots for the channels  $\Lambda\pi^+\pi^-\pi^+\pi^-$  and  $\Lambda\pi^+\pi^-\pi^+\pi^-\pi^0$  are shown in Fig. 6.8; both the  $\rho^0$  and  $\omega^0$  are strongly produced. A single example of  $\Lambda K^+K^-\pi^+\pi^-$  has been identified but no events compatible with  $\Lambda K_1^0 K_2^0 \pi^+\pi^-$  have been observed. The cross sections are as follows :

Channel	Cross section ( $\mu\text{b}$ )
$\Lambda\rho^0\pi^+\pi^-$	$108\pm 20$
$\Lambda\omega^0\pi^+\pi^-$	$185\pm 34$
$\Lambda\phi^0\pi^+\pi^-$	$< 3$

Neither the  $\rho^0$  nor the  $\omega^0$  are produced peripherally. A detailed investigation of these channels, which will not be reported here, indicates that the  $Y_1^{*0}$  (1385) is also copiously produced. It is conceivable, though somewhat difficult to prove, that both the  $\rho^0$  and the  $\omega^0$  are entirely associated with the  $Y_1^{*0}$  to form the following final states,

$$Y_1^{*\pm} (1385) \pi^{\mp} \rho^0 \quad \text{and} \quad Y_1^{*\pm} (1385) \pi^{\mp} \omega^0$$

If this is true it is possible to explain the large cross section for multineutrals in the  $\Lambda$ -201 topology, if the states

$$Y_1^{*+} \pi^0 \rho^+, Y_1^{*0} \pi^+ \rho^+, Y_1^{*0} \pi^0 \rho^0, \text{ and } Y_1^{*0} \pi^0 \omega^0$$

are produced equally strongly. The events belonging to the class  $\Lambda \pi^+ \pi^-$  ( $n\pi^0$ 's) do show a strong (if slightly shifted)  $\rho^0$  in the  $\pi^+ \pi^-$  effective mass distribution, Fig. 6.8.

The amount of  $Y^{*0}$  (1520) decaying into  $\Lambda \pi^+ \pi^-$  in these channels, is consistent with that seen in the  $\Sigma \pi$  decay modes discussed later in this chapter.

### 6.3 Production in association with a $\Sigma$ Hyperon.

#### Two Body Reactions.

Fig. 6.9 shows the  $\pi^+ \pi^-$  and  $K^+ K^-$  masses in the  $\Sigma^0 \pi^+ \pi^-$  and  $\Sigma^0 K^+ K^-$  final states. Also shown for comparison, is the  $K^0 K^{\pm}$  effective mass distribution for the  $\Sigma^{\pm} K^{\mp} K^0$  channels. No enhancement is seen in this distribution, in marked contrast to the strong  $\phi^0$  produced in association with the  $\Sigma^0$ . Results cannot be given for the unfittable  $\Sigma^0 \omega^0$  final state, but the table below contains the  $\rho^0$  and  $\phi^0$  cross sections in the other two states.

Channel	Cross section ( $\mu\text{b}$ )
$\Sigma^0 \rho^0$	$55 \pm 19$
$\Sigma^0 \phi^0$	$18 \pm 5$

The cross section for  $\Sigma^0 \phi^0$  is about half that for  $\Lambda \phi^0$ , a feature observed by Connolly et al.<sup>43)</sup> at 2.23 GeV/c. In  $\Sigma^0 \pi^+ \pi^-$ , the absence of strong  $Y^*$  production makes the  $\rho^0$  easier to extract than in the  $\Lambda \pi^+ \pi^-$  case, and the effective mass plot is noticeably less affected by background. The C.M.S. angular distributions (not presented) are similar to those for  $\Lambda \rho^0$  and  $\Lambda \phi^0$ . No detailed analysis of the density matrix elements could be undertaken because of the small number of events.

### Three Body Reactions.

Strong  $\rho^0, \omega^0$  and  $\phi^0$  production occurs in the final states involving charged  $\Sigma$ 's as can be seen from the effective mass plots of Fig. 6.10. Within the available statistics, the cross sections for the production of  $\omega^0$  and  $\phi^0$  are the same in the channel involving the  $\Sigma^+ \pi^-$  combination as in that involving  $\Sigma^- \pi^+$ , and for this reason the  $\Sigma^{\pm}$  reactions are combined together in the table below. The  $\Sigma^+ \pi^- \rho^0$  and  $\Sigma^- \pi^+ \rho^0$  cross section are kept separate for a reason which

will become apparent below.

Resonance	Final State	Cross section ( $\mu\text{b}$ )
$\rho^0$	$\Sigma^+ \pi^- \pi^+ \pi^-$	$88 \pm 26$
$\rho^0$	$\Sigma^- \pi^+ \pi^- \pi^+$	$64 \pm 19$
$\omega^0$	$\Sigma^\pm \pi^\mp \pi^- \pi^+ \pi^0$	$139 \pm 35$
$\phi^0$	$\Sigma^\pm \pi^\mp K^0 K^0$	$15 \pm 7$
$\phi^0$	$\Sigma^\pm \pi^\mp K^+ K^-$	$10 \pm 3$

The first question that arises as far as these states are concerned is, does the extra  $\pi$  resonate with either the  $\Sigma$  or the vector meson to reduce the final state to one involving two bodies, predominantly? The answer to this appears to be no. Dalitz plots for the  $\Sigma\pi\rho^0$  and  $\Sigma\pi\omega^0$  channels are shown in Fig. 6.11. The vertical band on the  $\Sigma\pi\rho^0$  plot at about  $1.7 \text{ Gev}^2$  shows that at least part of the  $\Sigma^+ \pi^- \rho^0$  state originates from  $\Sigma^+ A_2^-$ . The production of the  $A$  meson is taken up again in chapter 7. The  $\Sigma\pi$  combinations on both plots show slight evidence for  $Y_0^*$  (1520) production. Examination of these Dalitz plots alone does not establish the existence of  $Y_0^*$  - vector meson production, since the background may contain strong  $Y_0^*$  + non-resonating pion or kaon combinations.

In order to demonstrate that there is associated  $Y_0^*$  (1520) - vector meson production, background-subtracted effective mass plots for the  $\Sigma\pi$  combinations are presented in Fig. 6.12. The subtraction has been made in such a way that 80% of any associated production remains in the selected band. The  $\Sigma\pi$  effective mass distributions are presented for the  $\Sigma\pi\rho^0$  and  $\Sigma\pi\phi^0$  channels only, the errors generated by the subtraction process being so large in the  $\Sigma\pi\omega^0$  case as to render the final distribution meaningless. The cross sections were obtained directly from triangle plots. These are not shown here as they provide very little additional information in these very complex final states.

Channel	Cross section ( $\mu\text{b}$ )	Channel	Cross section ( $\mu\text{b}$ )
$Y_0^*(1520)\rho^0$	$76_{\pm 16}$	$Y_0^*(1405)\rho^0$	$12_{\pm 8}$
$Y_0^*(1520)\omega^0$	$16_{\pm 8}$	$Y_0^*(1405)\omega^0$	$< 8$
$Y_0^*(1520)\phi^0$	$16_{\pm 6}$	$Y_0^*(1405)\phi^0$	$7_{\pm 4}$

The  $Y_0^*(1520) \rightarrow \Sigma^+ \pi^-$  branching ratio has been taken as  $39_{\pm 5}\%$ . From the cross sections above it can be seen that the  $\rho^0$  and  $\omega^0$  are not produced preferentially in association with a  $Y_0^*$ .

The C.M.S. angular distributions for the  $\rho^0, \omega^0$  and  $\phi^0$  are shown in Fig. 6.13, with only the  $\rho$  mesons in the  $\Sigma A$

events removed. A forward peak is in evidence in all three angular distributions, but only the  $\rho^0$  and  $\omega^0$  show signs of an additional backward peak (cf. section 6.1).

### Multiparticle Final States<sub>2</sub>

The effective mass distribution for the  $\pi^+\pi^-$  combinations in the  $\Sigma^+\pi^-\pi^+\pi^-\pi^0$  final state, Fig. 6.14, shows little, if any,  $\rho^0$  production. A limit of about  $17\mu\text{b}$  can be placed on the cross section for  $\Sigma^+\pi^-\pi^0\rho^0$ .

### 6.4 Production in KN and EK channels.

Most of the channels involving KN and additional pions are dominated by the production of the  $K^*$  and  $N^*$  resonances. The detailed analysis of these channels has been reported elsewhere <sup>44</sup>). For completeness the  $\pi^+\pi^-$  mass spectrum in  $\bar{K}^0n\pi^+\pi^-$  and the  $\pi^+\pi^-\pi^0$  spectrum in  $\bar{K}^0p\pi^-\pi^+\pi^-\pi^0$  are presented in Fig. 6.14. The cross sections for  $\bar{K}^0n\rho^0$  and  $\bar{K}^0p\pi^-\omega^0$  are  $230\pm 50\mu\text{b}$  and  $56\pm 15\mu\text{b}$  respectively. The 400 topology, in which the  $K^-$  states are to be found, has not been measured by the collaboration.

No  $\rho^0$  or  $\omega^0$  production is observed in the EK states at 3.5 Gev/c.

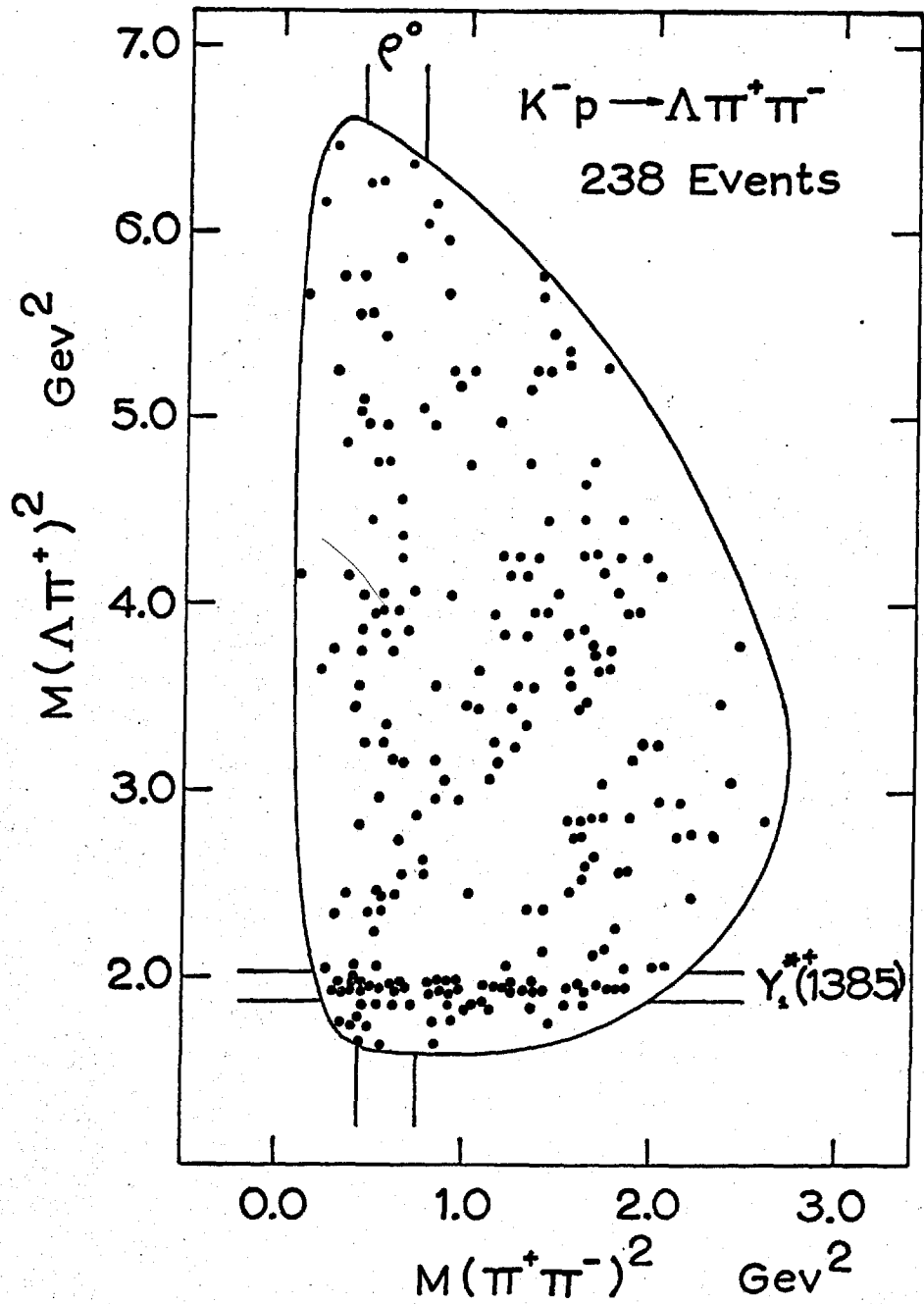


Fig. 6.1a

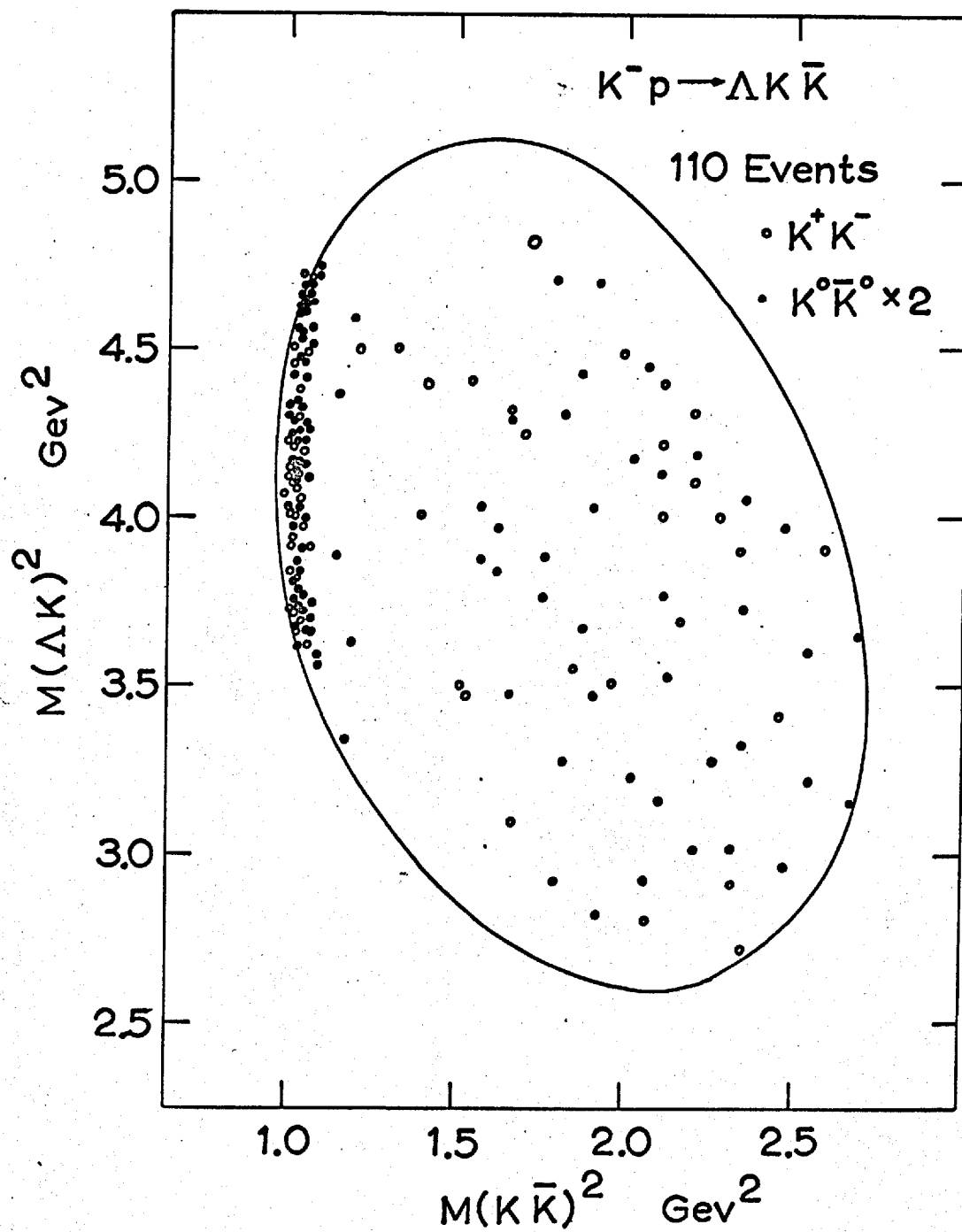


Fig. 6.1b

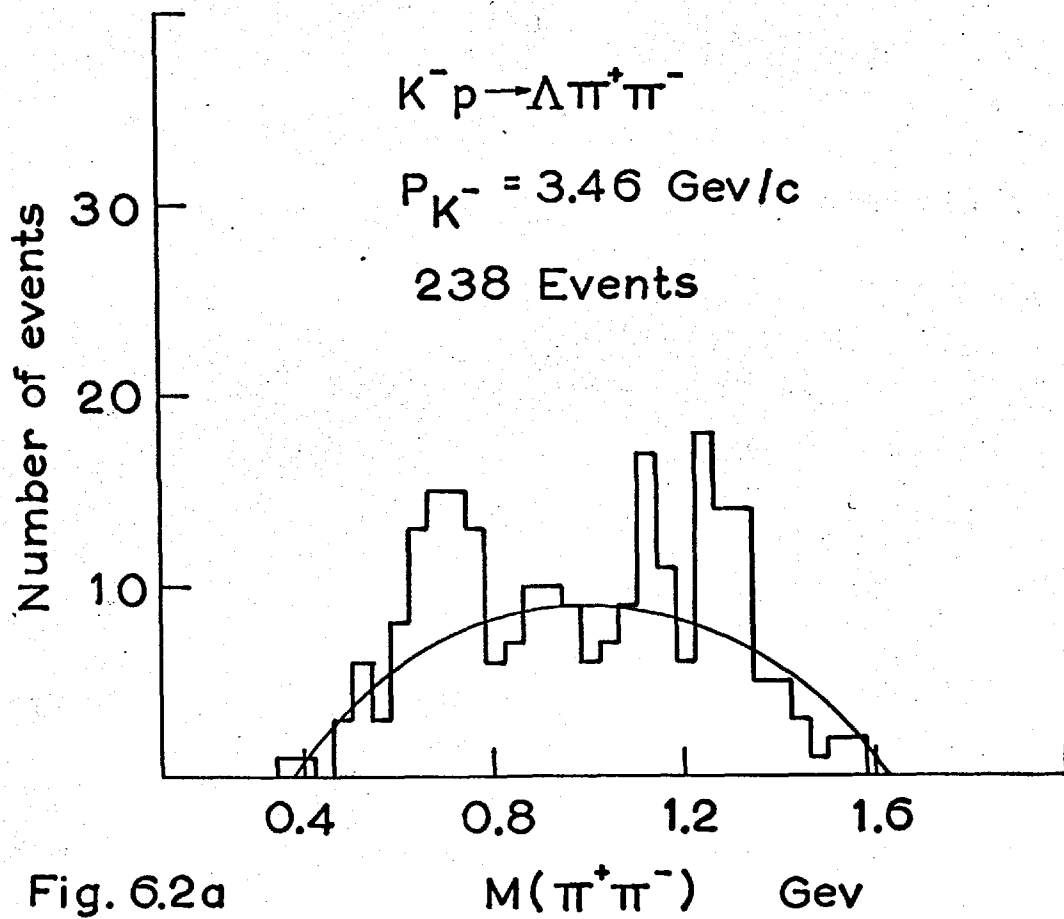


Fig. 6.2a

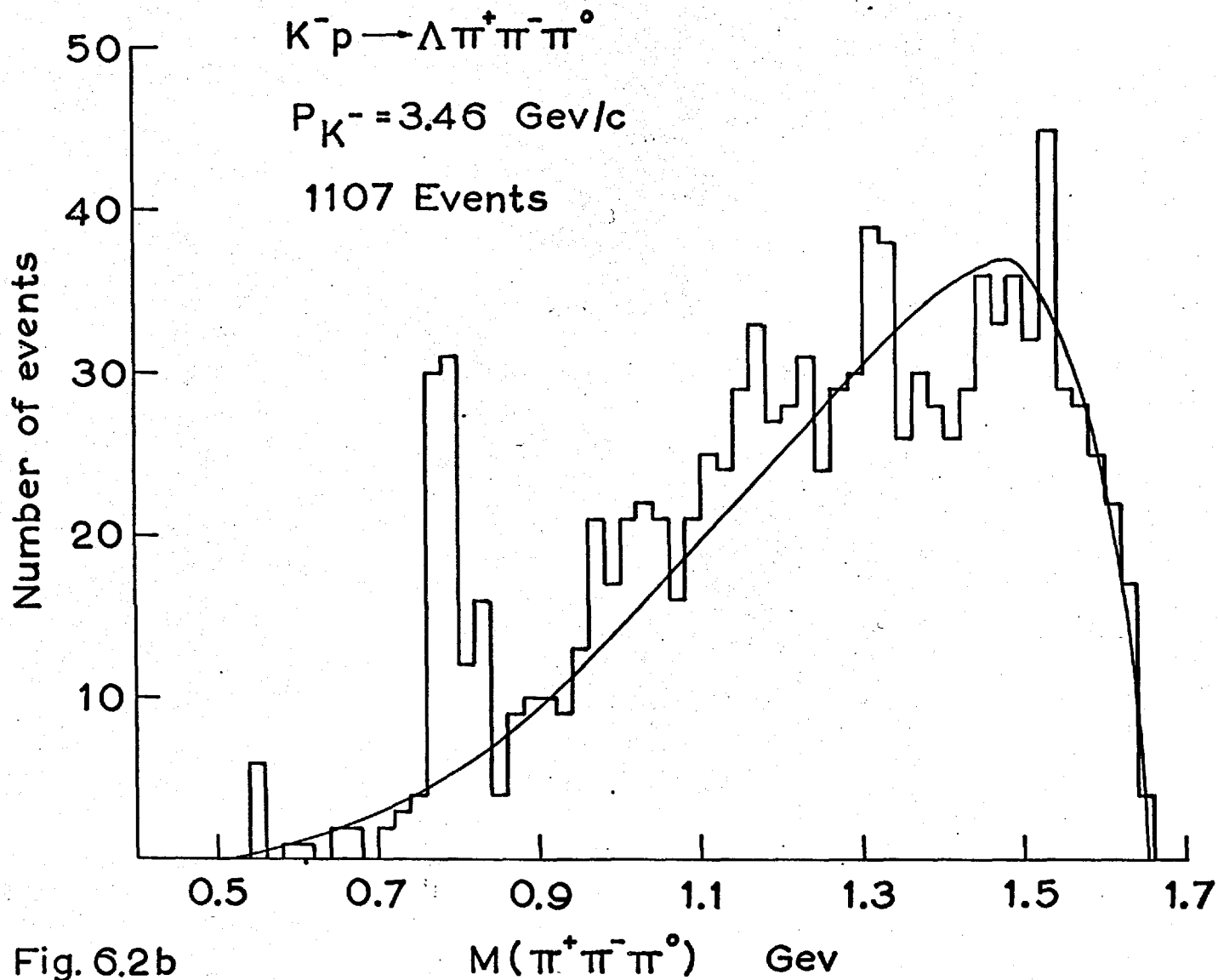


Fig. 6.2b

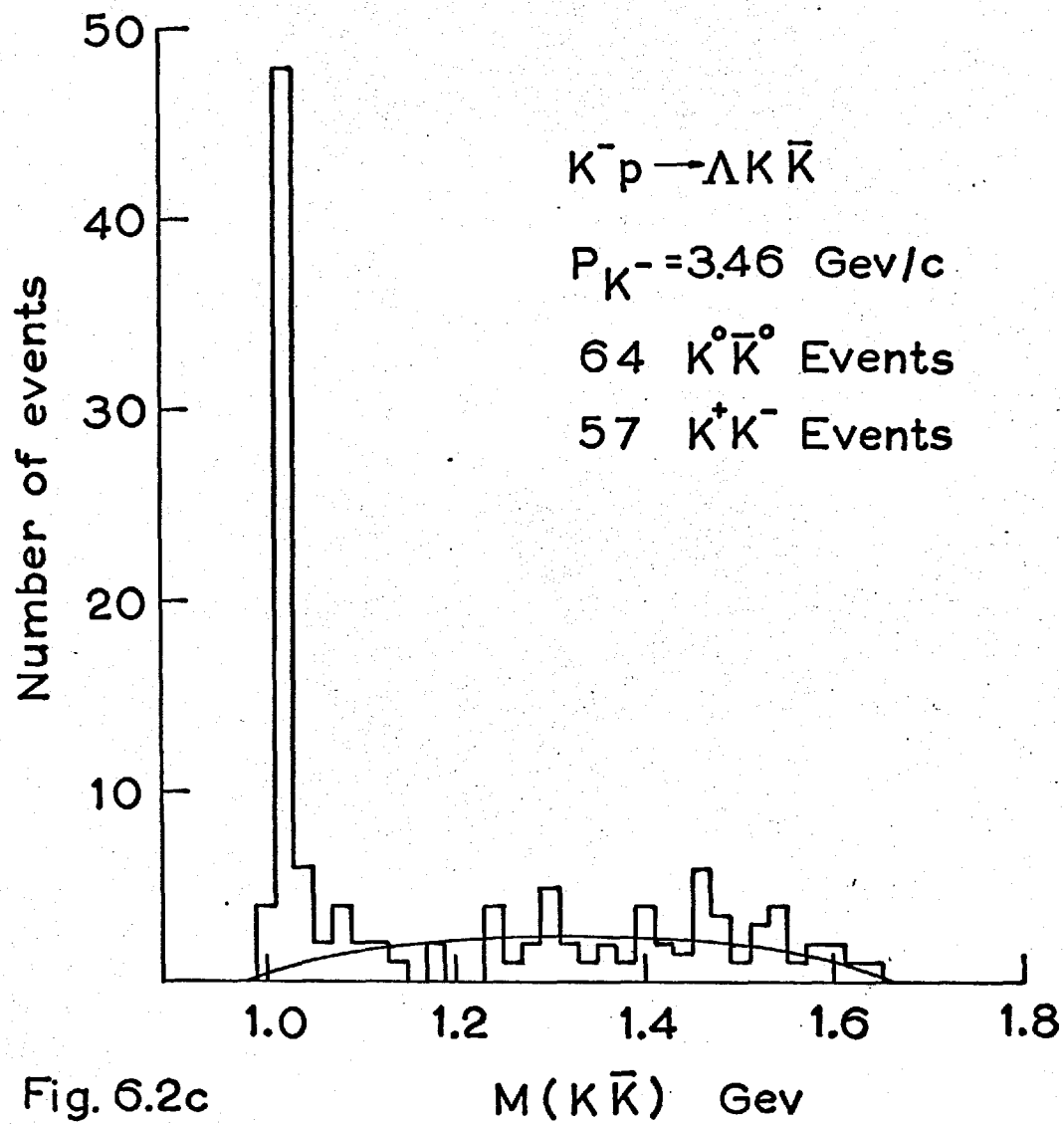


Fig. 6.2c

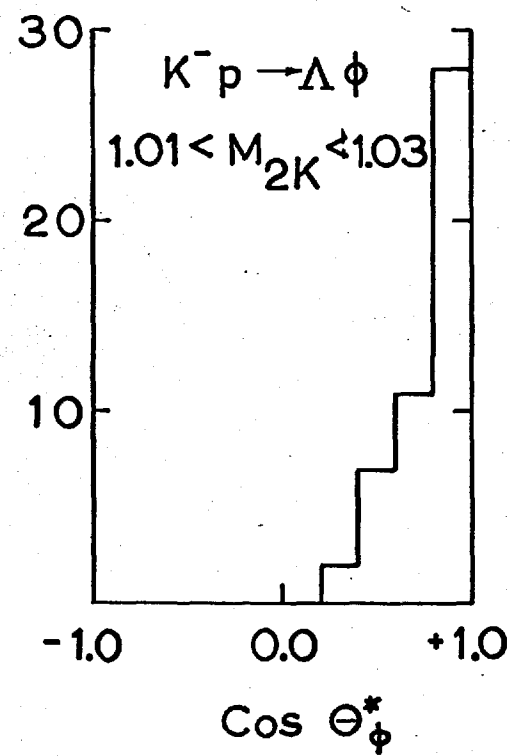
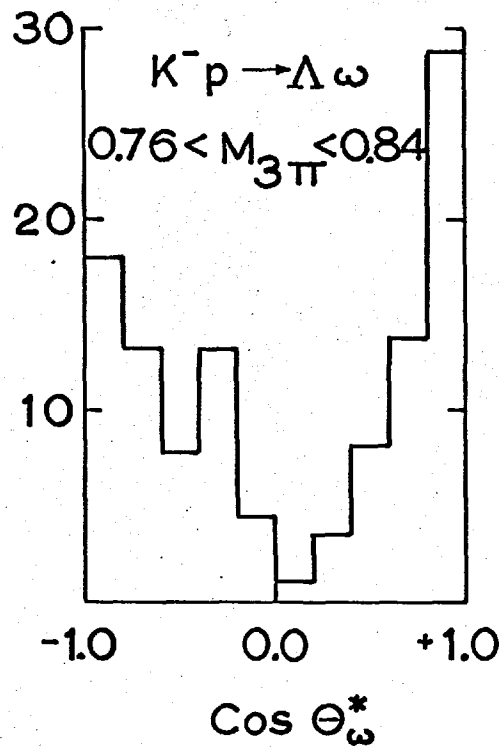
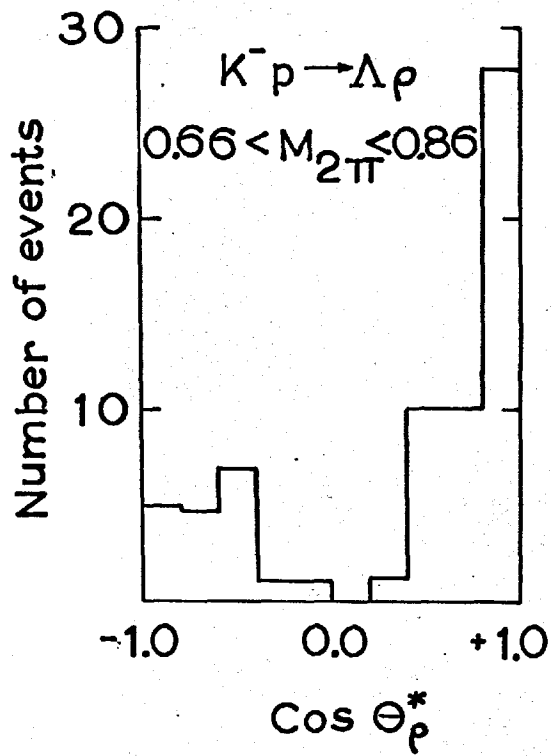


Fig. 6.3 C.M.S. Angular distributions

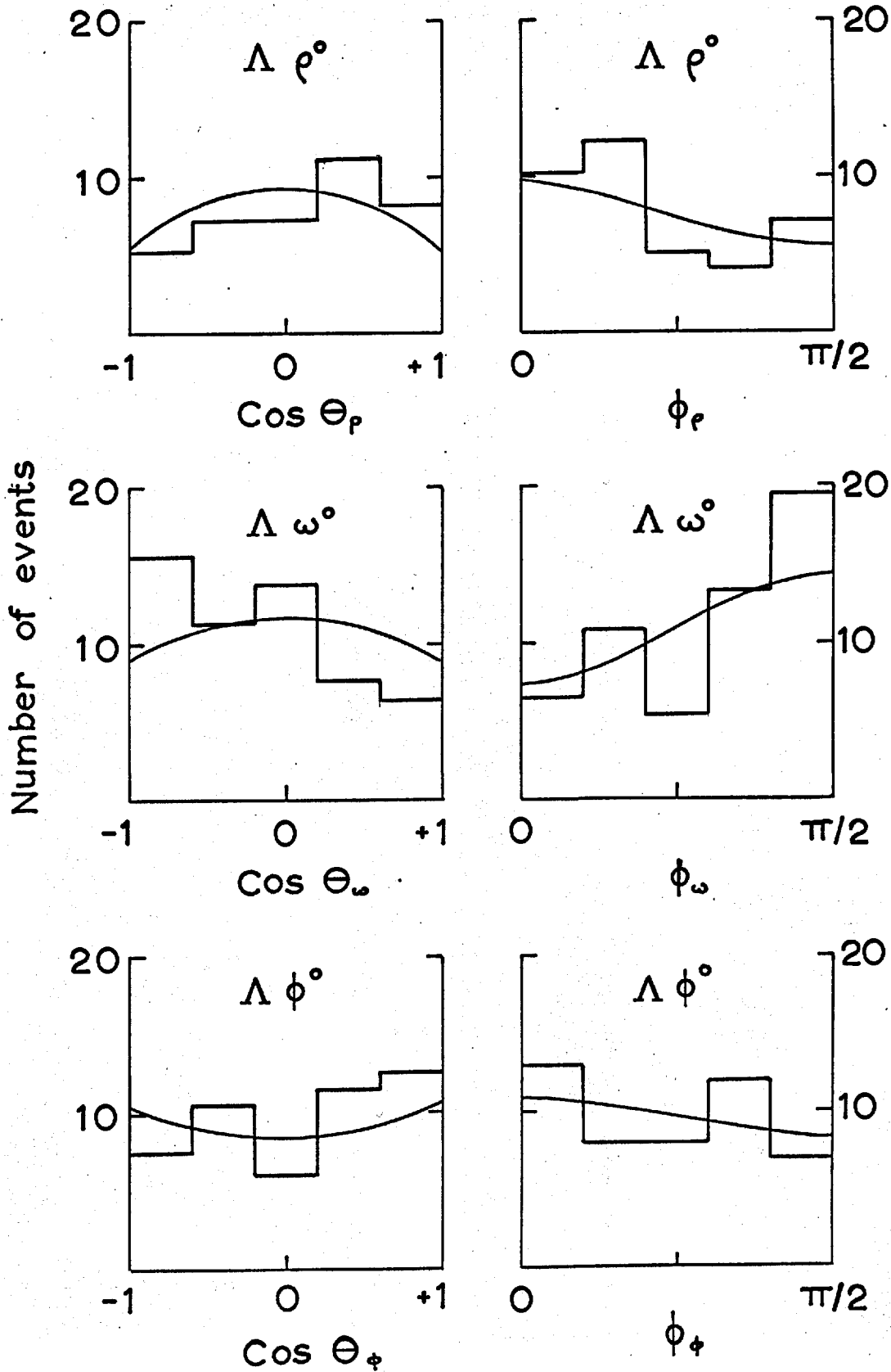


Fig.6.4 Decay angular distributions ( $\text{Cos } \Theta^* > 0$ )

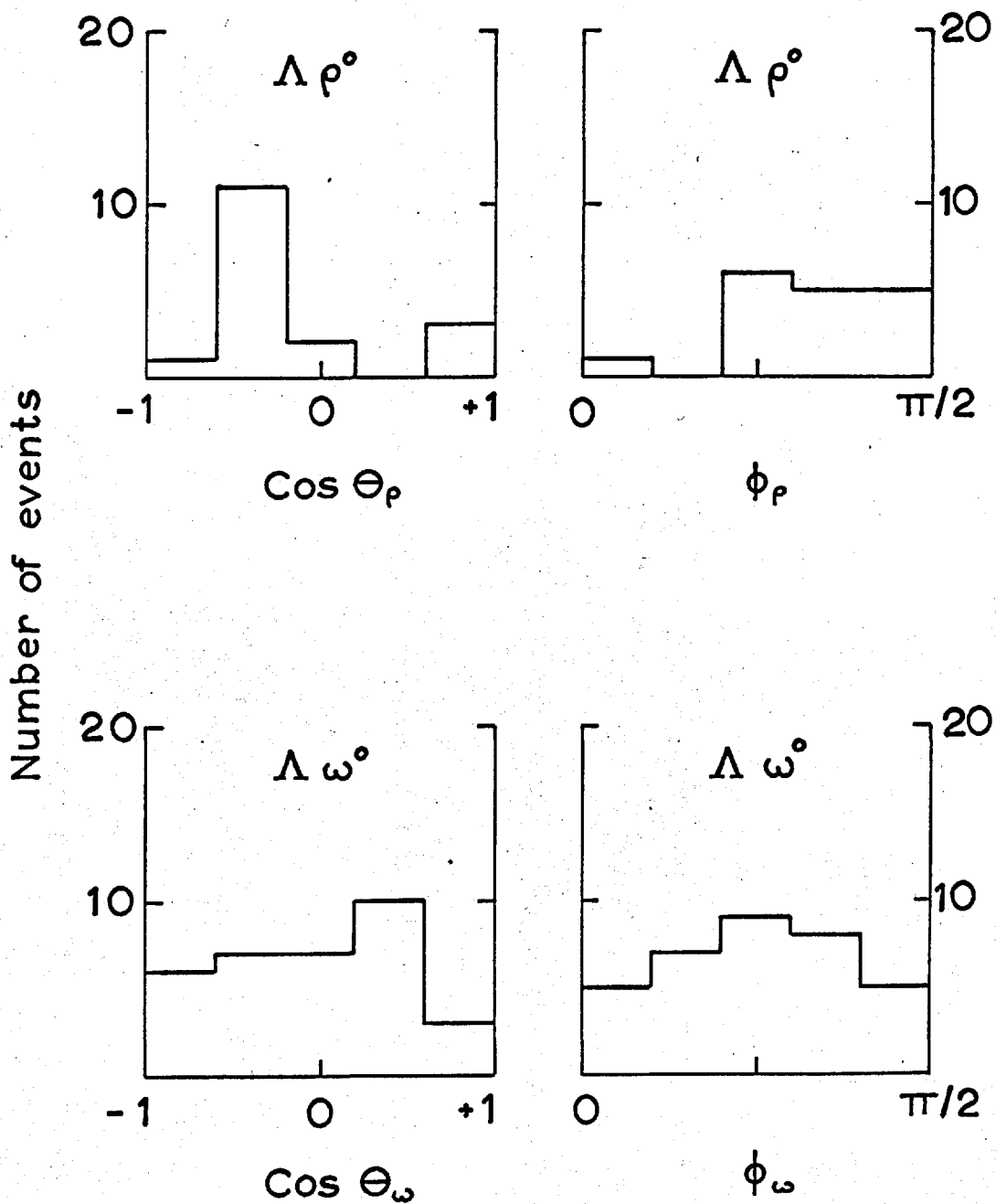


Fig. 6.5 Decay angular distributions

(Cos  $\Theta^* < 0$ )

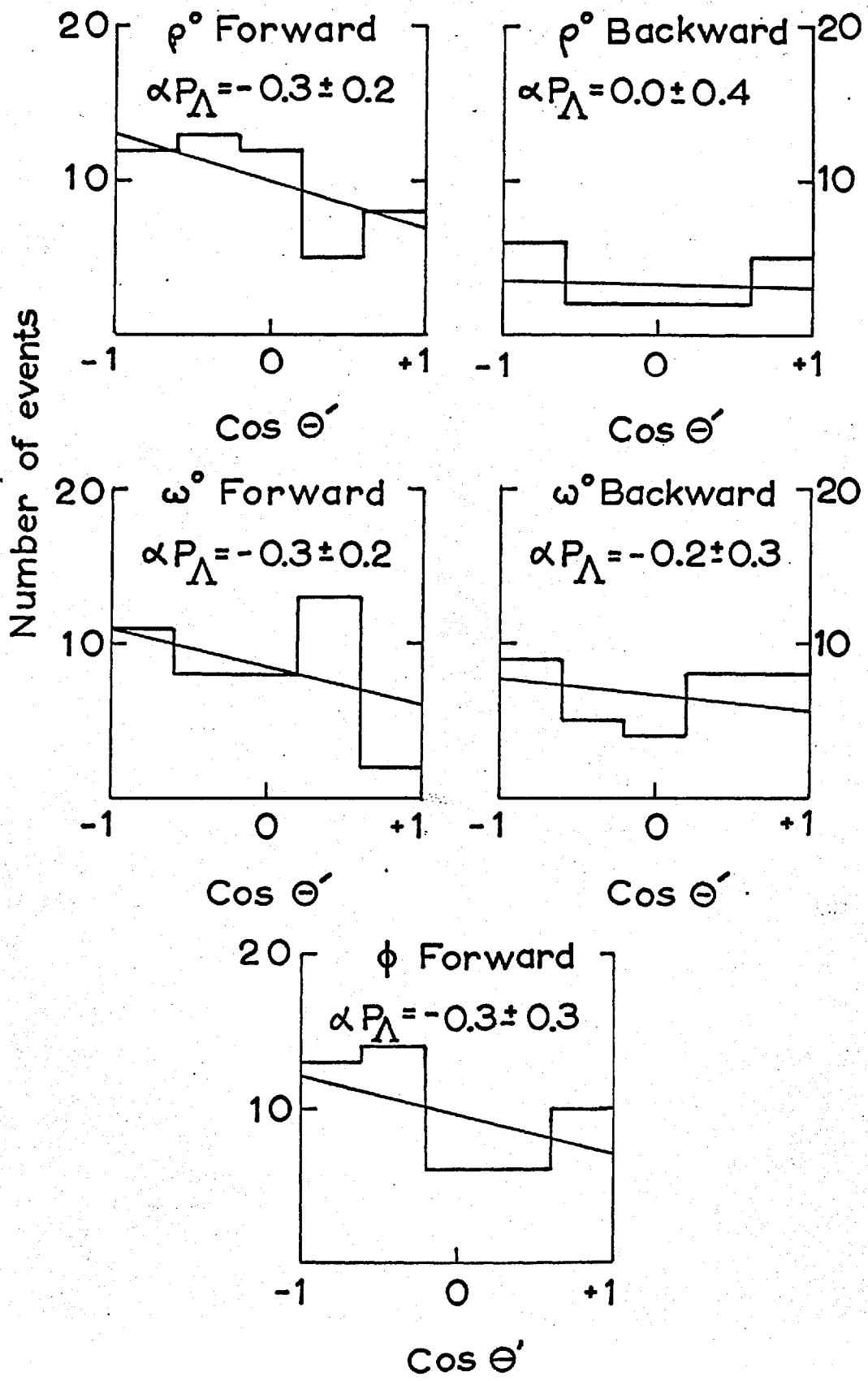


Fig.6.6 Lambda Polarizations

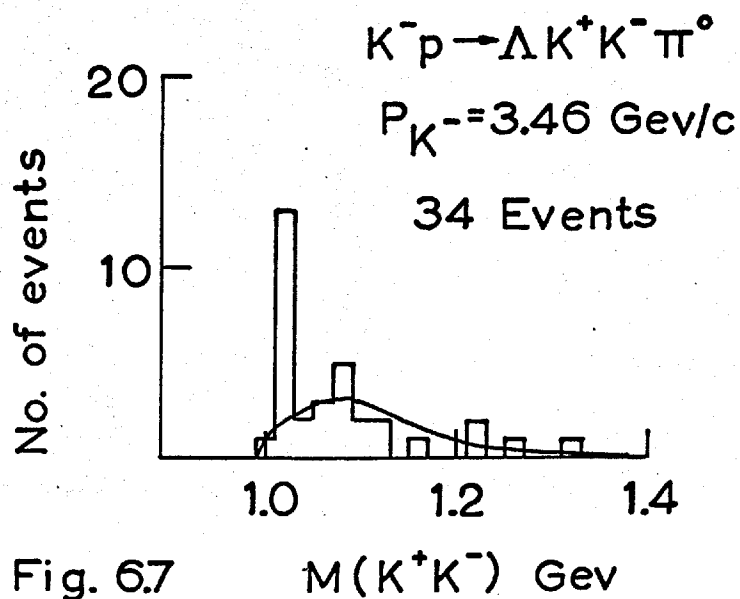
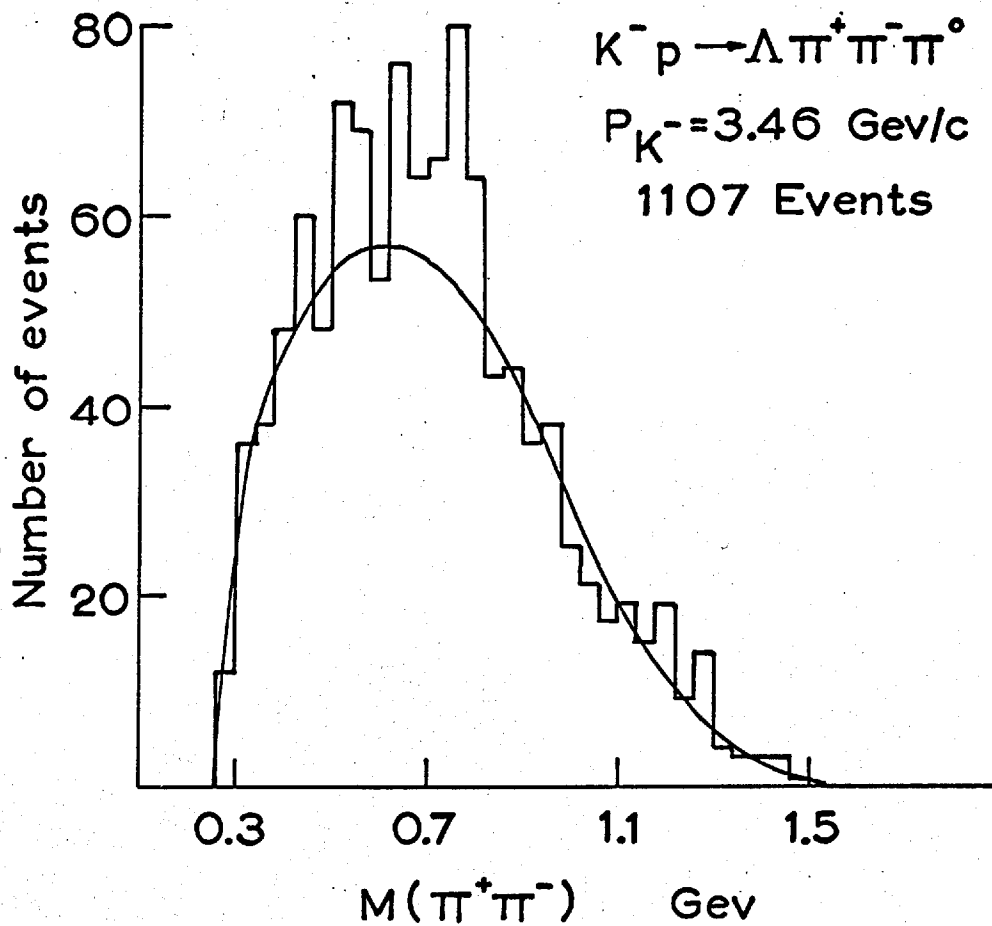


Fig. 6.7

 $M(K^+ K^-) \text{ GeV}$

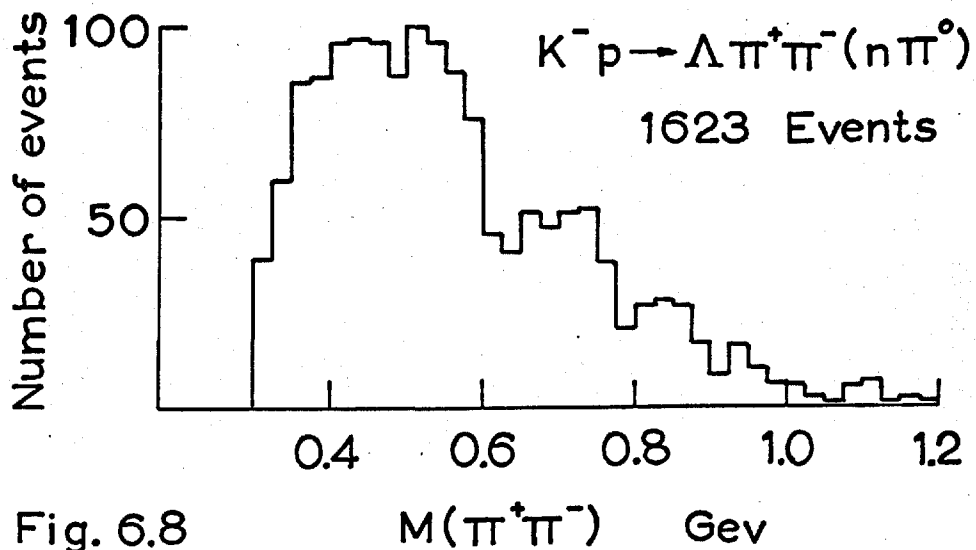
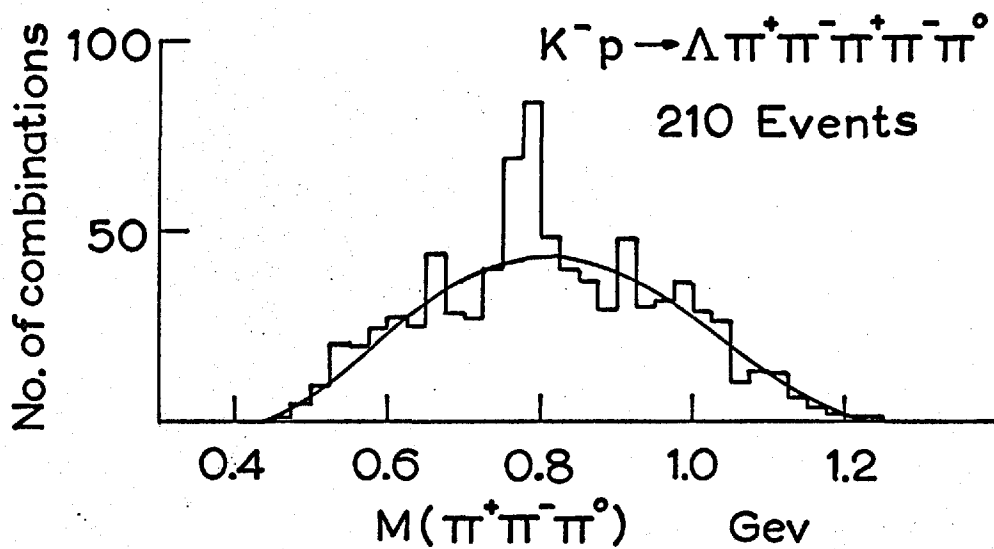
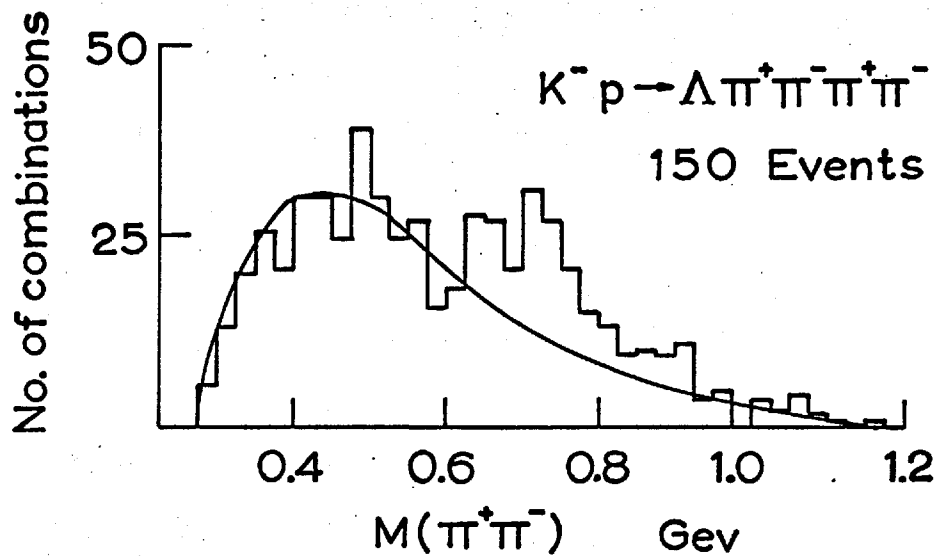


Fig. 6.8

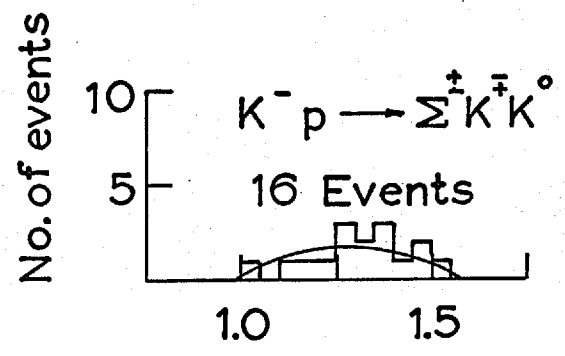
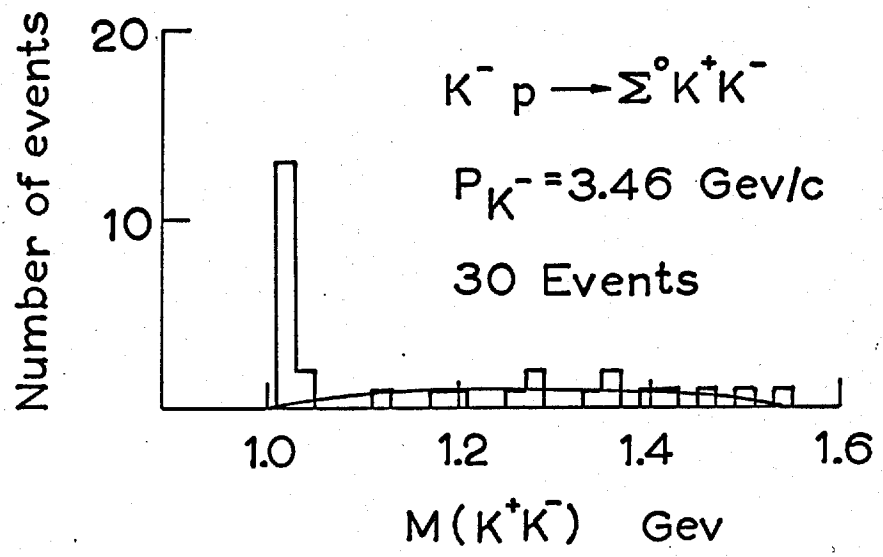
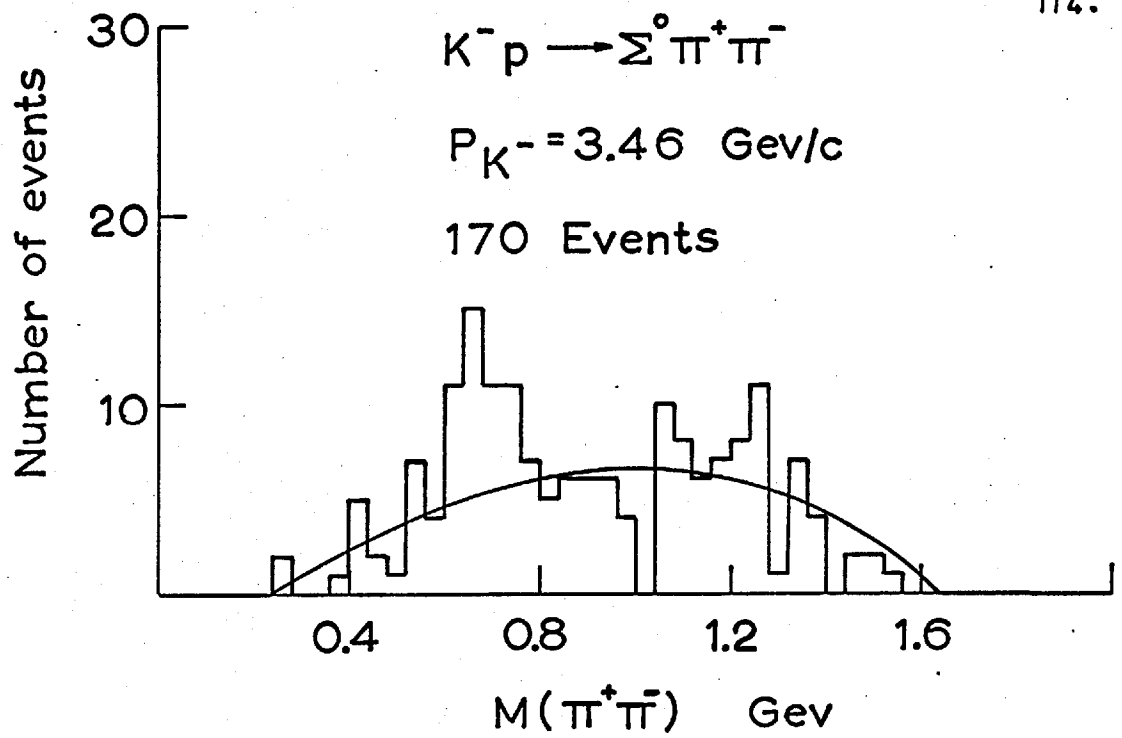


Fig. 6.9  $M(K^{\pm} K^0) \text{ Gev}$

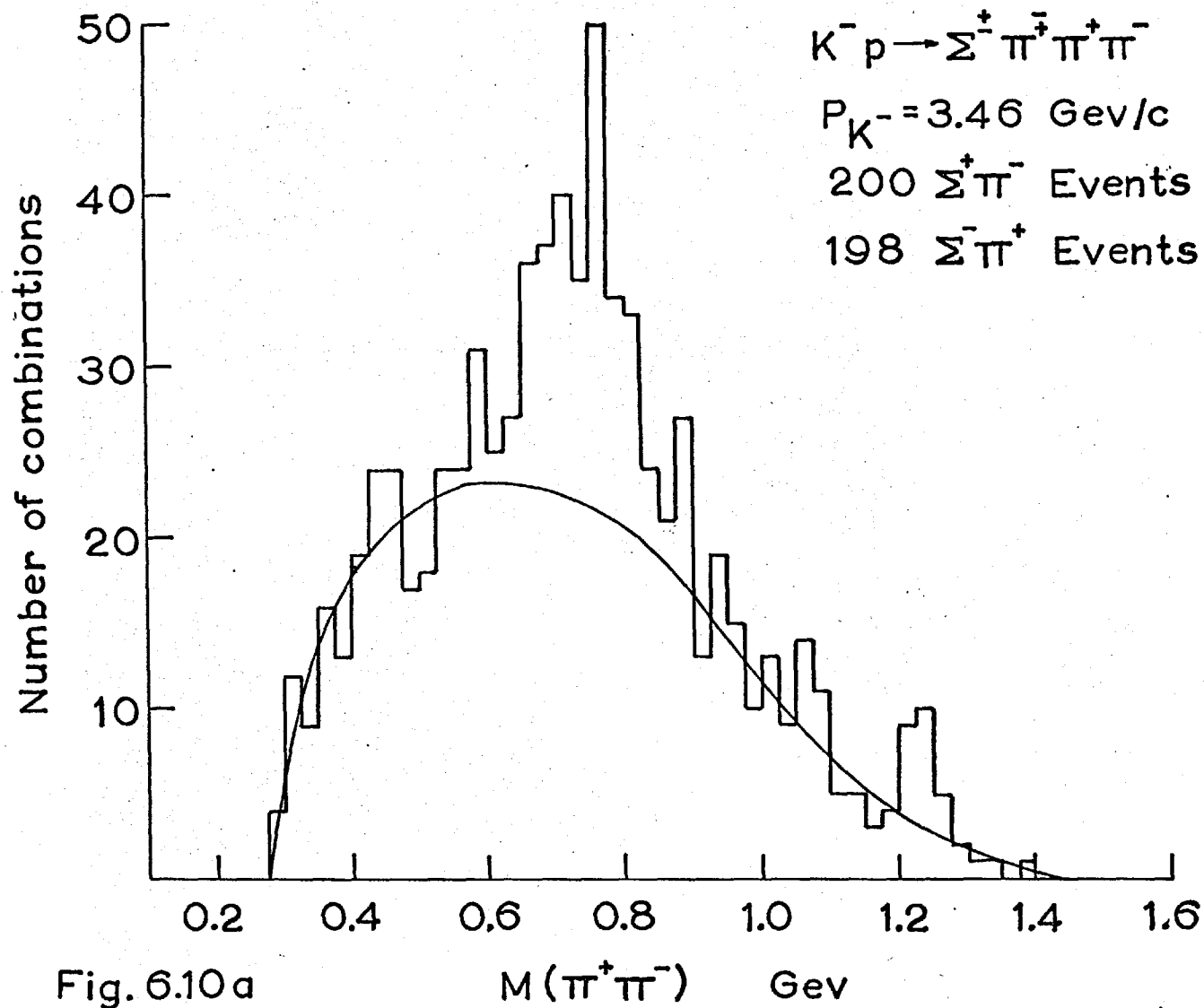


Fig. 6.10a

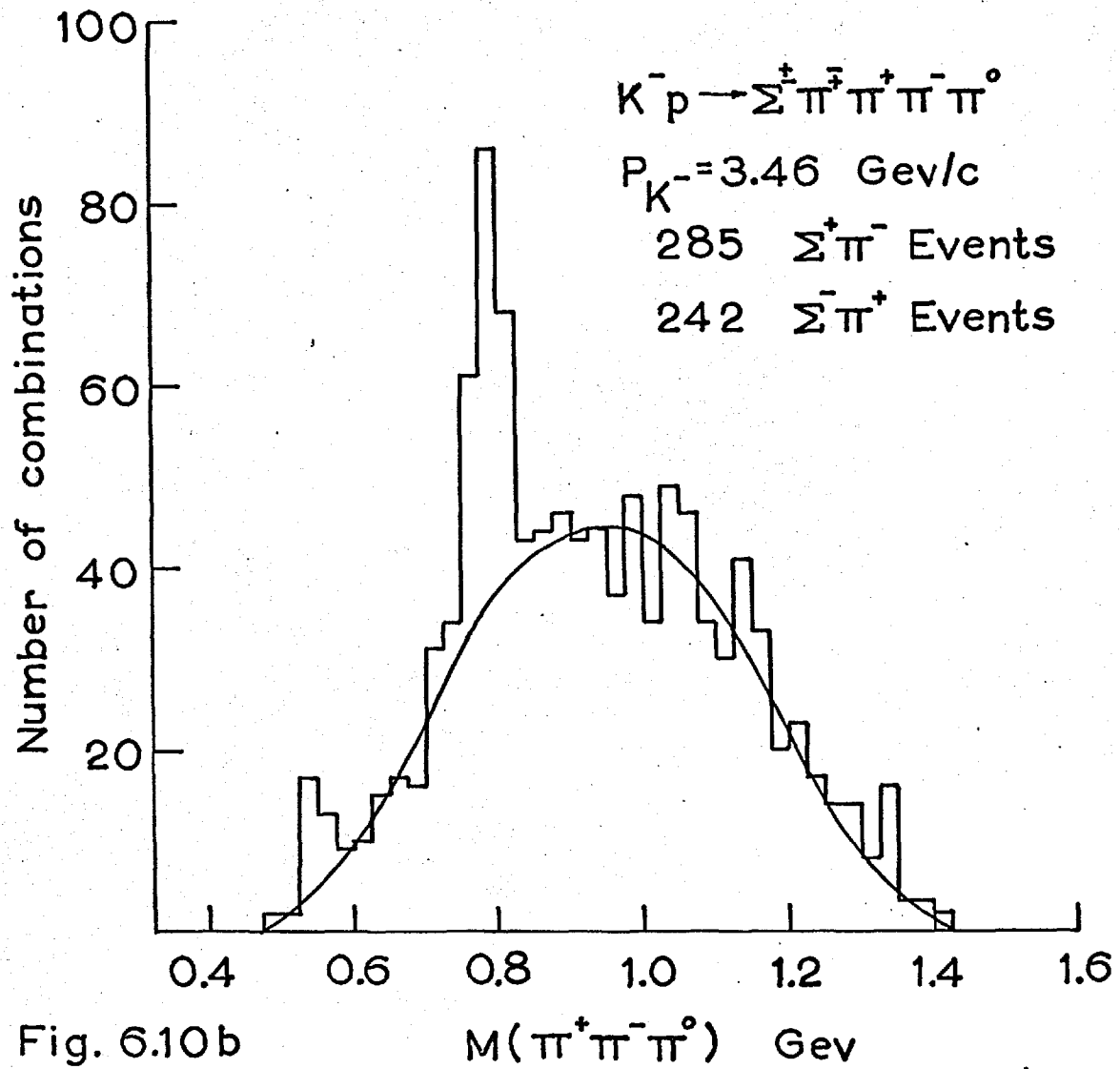


Fig. 6.10b

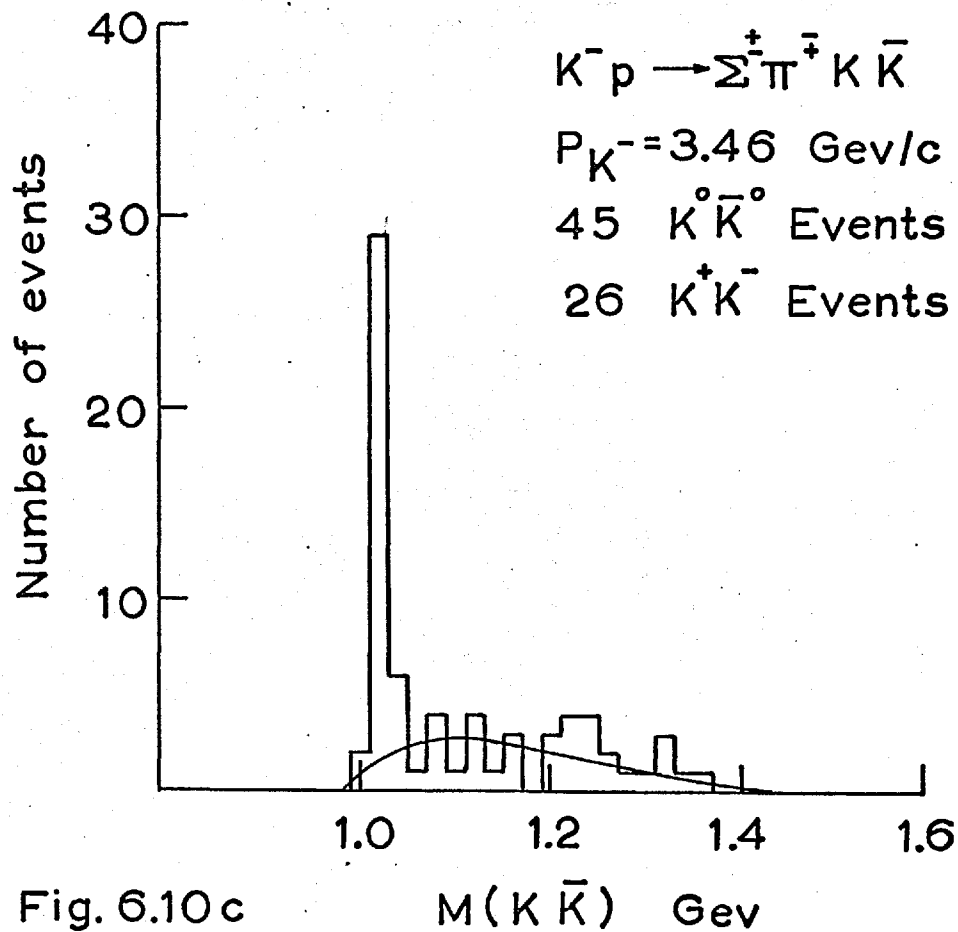


Fig. 6.10c

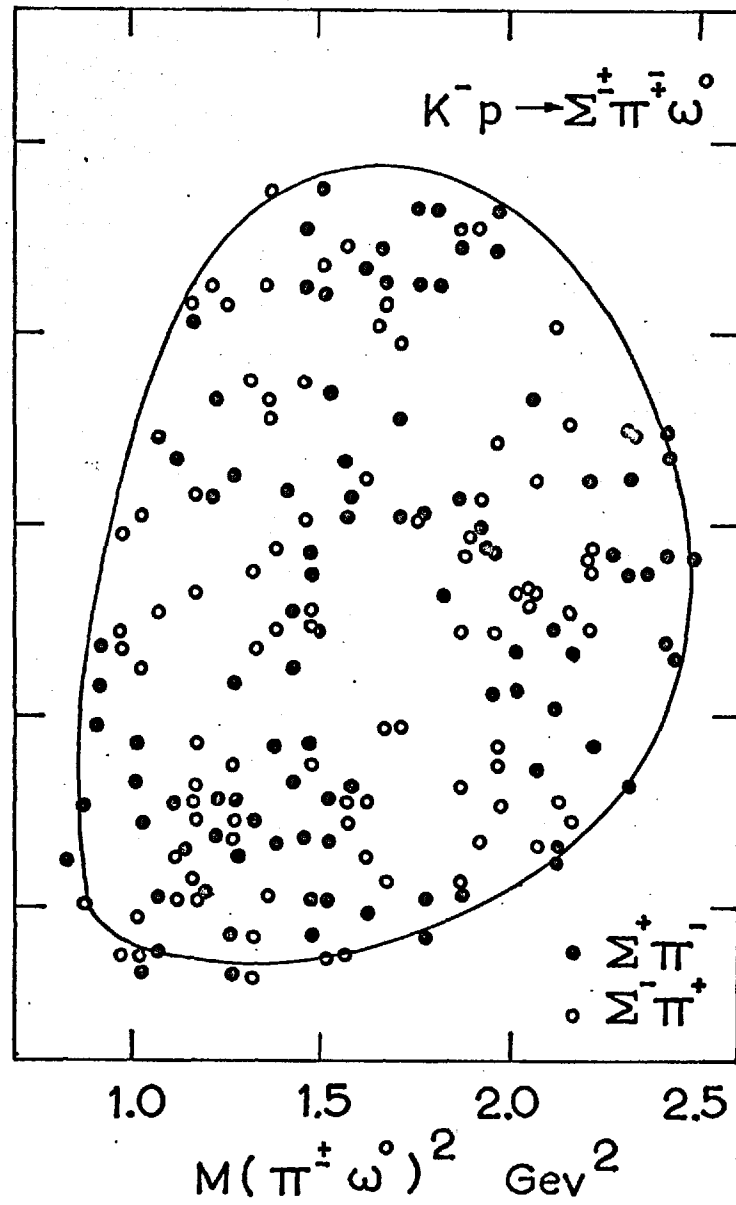
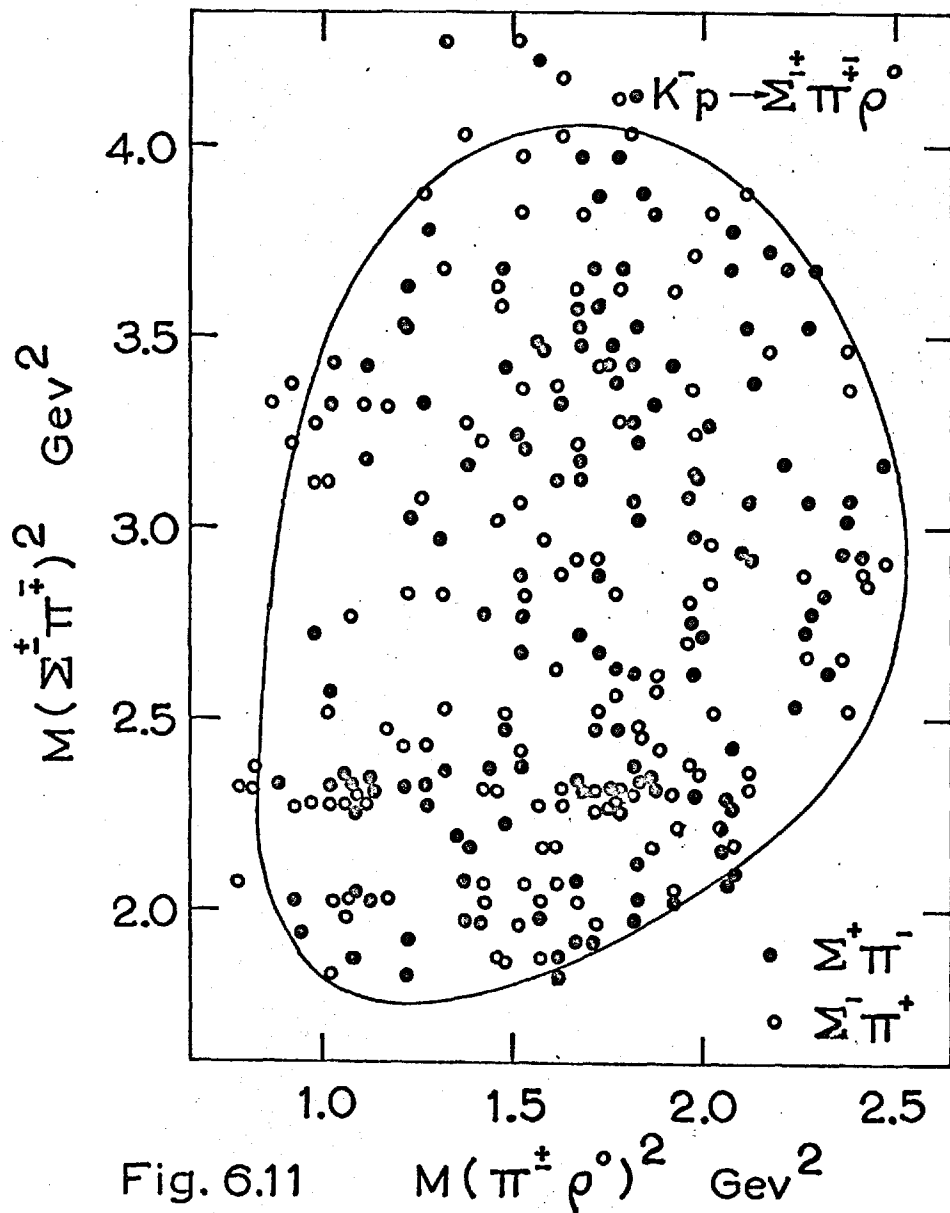


Fig. 6.11

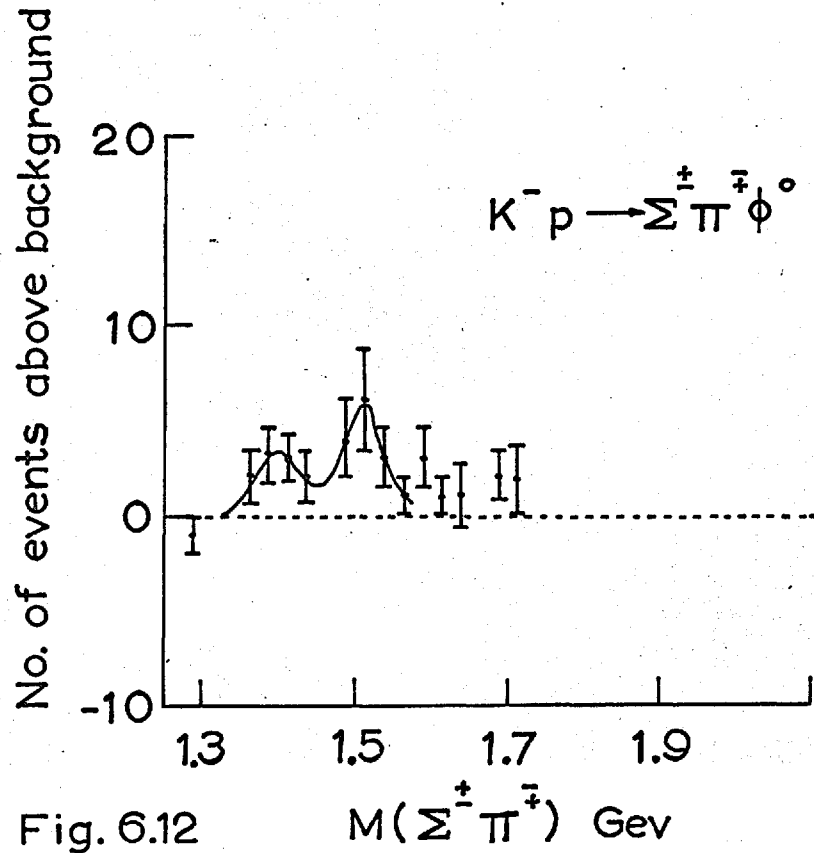
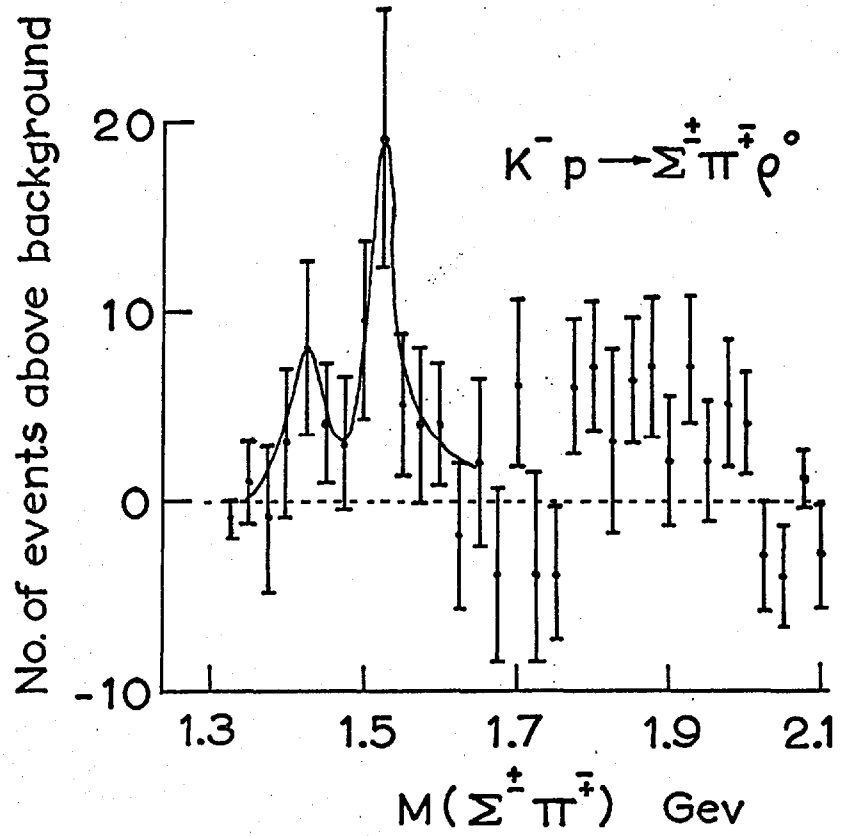


Fig. 6.12

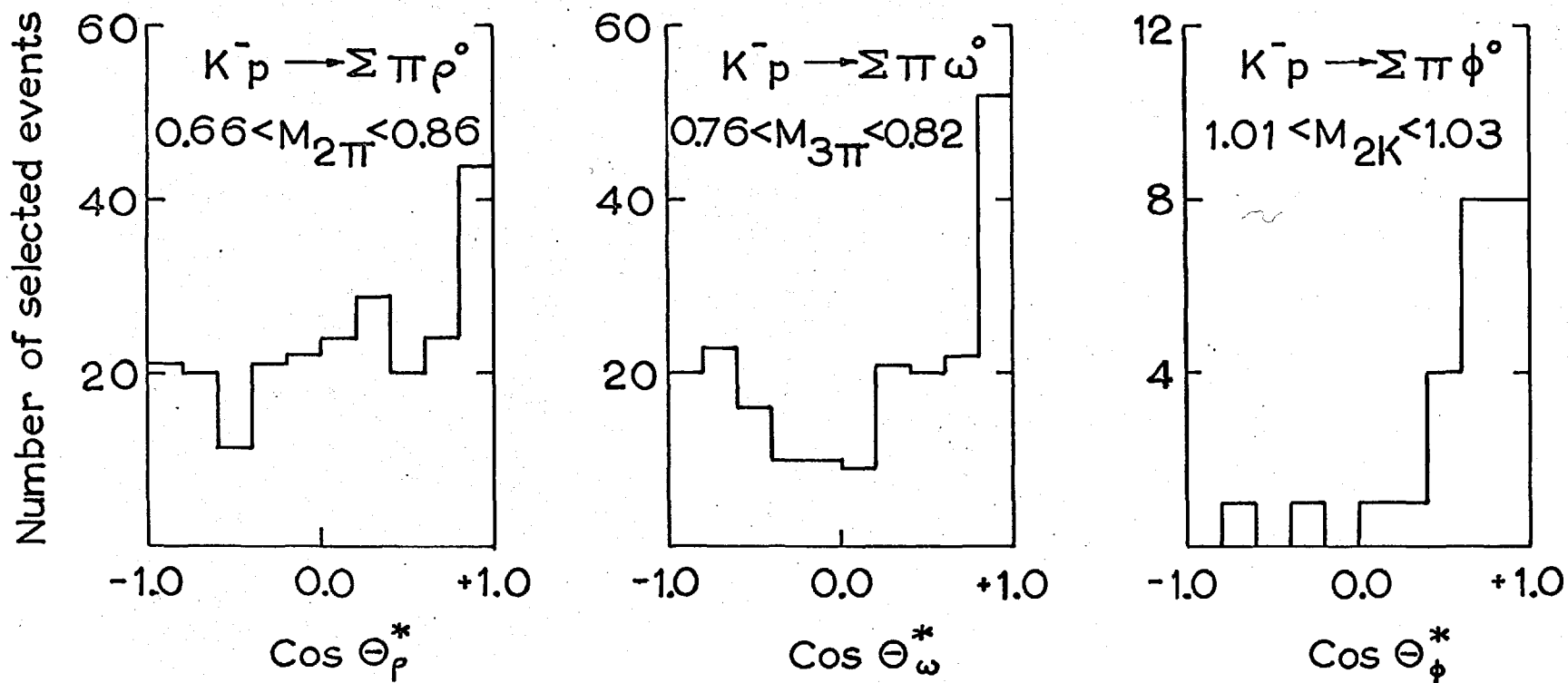


Fig. 6.13

C.M.S. Angular distributions

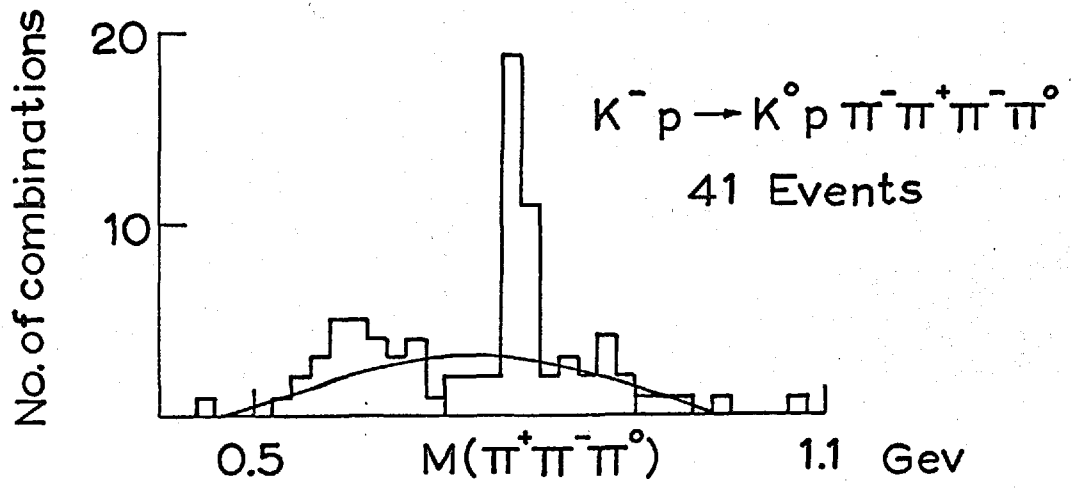
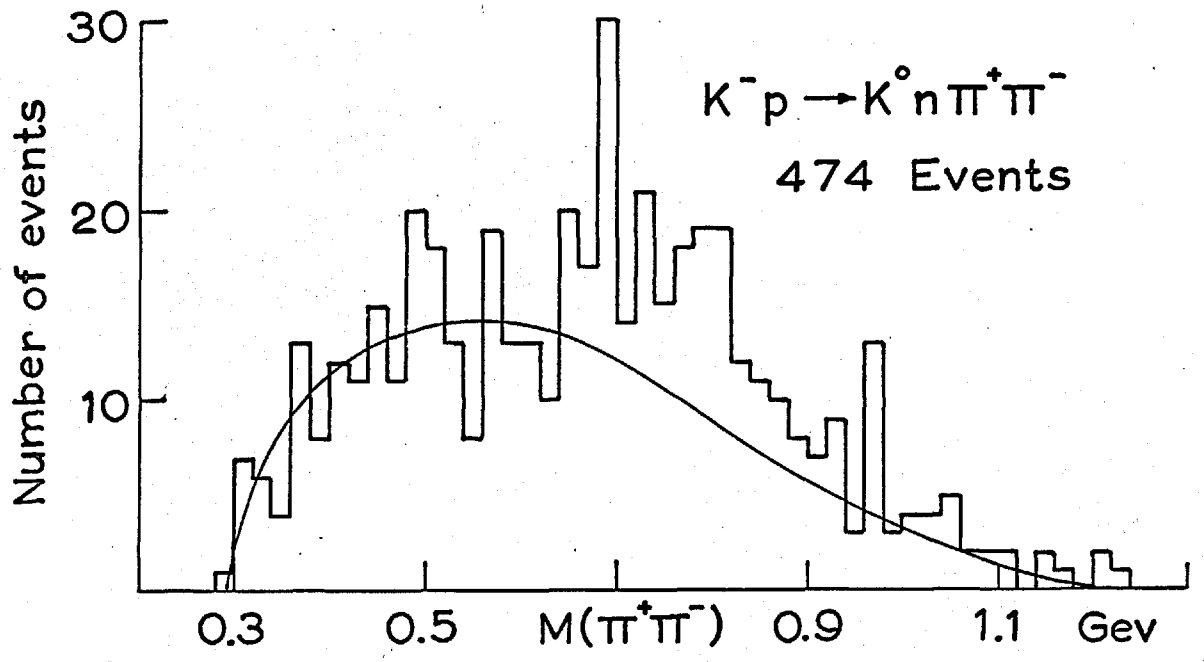
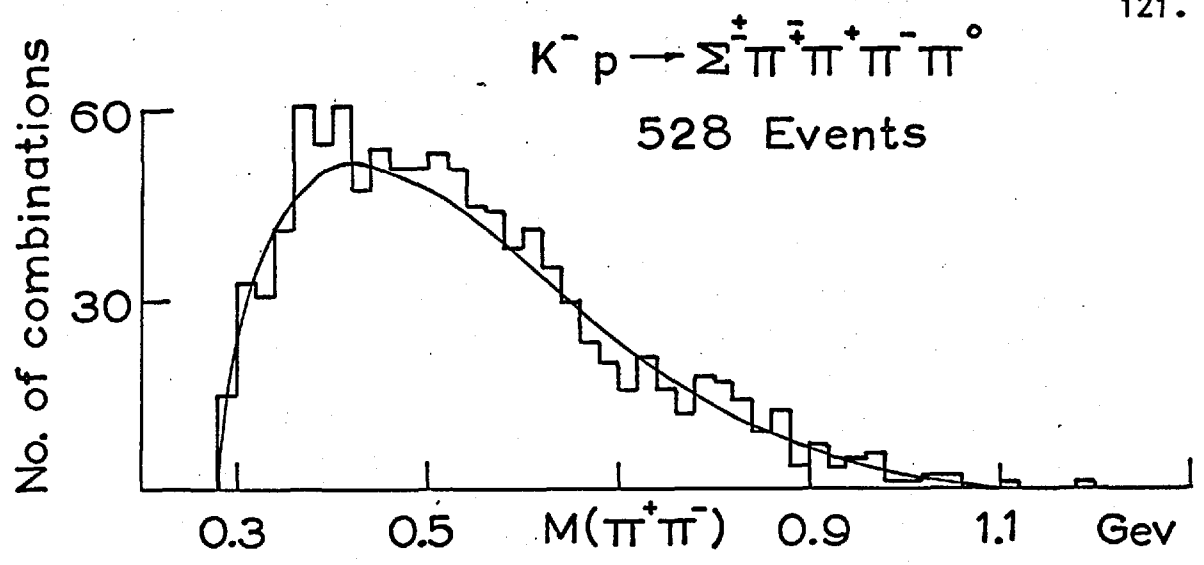


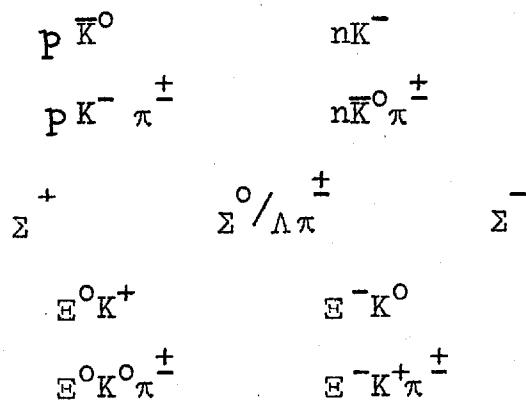
Fig. 6.14

CHAPTER 7

PRODUCTION OF THE  $\rho^{\pm}$  AND OTHER RESONANCES

7.1 Introduction.

The charged  $\rho$  mesons can be produced in association with the following  $Q=\pm 1$ ,  $Y=0$  systems:



Many of these channels are already multineutral and the addition of a single neutral pion renders them all multineutral.

No charged  $\rho$  production is observed in the  $\Xi$  channels, and only one  $\bar{K}^0$  channel,  $\bar{K}^0 p \pi^- \pi^0$ , shows signs of  $\rho^-$ , Fig. 7.5; the cross section is  $280 \pm 70 \mu\text{b}$ . No information is available concerning  $\rho$  production in states involving a  $K^-$ .

In the last two sections of this chapter the  $\eta^0, X^0, f^0$  and  $A_2^-$  resonances are discussed.

## 7.2 Charged $\rho$ Production in association with a $\Lambda$ Hyperon.

### Three Body Reactions.

The  $\pi^+\pi^0$  and  $\pi^-\pi^0$  effective mass distributions for the  $\Lambda\pi^+\pi^0$  final state, Fig. 7.1, seem consistent with cross sections of zero for the  $\Lambda\pi^+\rho^-$  and  $\Lambda\pi^-\rho^+$  channels. The  $Y_1^*(1385)$  is produced strongly in this final state, particularly in the positive charge state. The three  $\Lambda\pi$  versus  $\pi\pi$  triangle plots (not shown) have been examined in detail, and, though consistent with little, if any,  $\rho^+$  and  $\rho^0$  production, do seem to show evidence for a certain amount of  $\rho^-$ , which occurs entirely in association with the  $Y_1^{*+}(1385)$ . Fig. 7.2 shows the background subtracted histogram for the  $\Lambda\pi^+$  effective mass combinations occurring in the  $\rho^-$  region on the triangle plot. This distribution shows conclusively that  $Y_1^{*+}(1385)\rho^-$  production does occur, even though the  $\rho^-$  does not show up very well on the total  $\pi^-\pi^0$  mass plot. The  $Y_1^*\rho$  production is summarized in the following table.

Channel	Cross section ( $\mu\text{b}$ )
$Y_1^{*+}(1385)\rho^-$	$53 \pm 17$
$Y_1^{*0}(1385)\rho^0$	$< 15$
$Y_1^{*-}(1385)\rho^+$	$< 15$

The existence of  $Y_1^{*+} \rho^-$  and non-existence of  $Y_1^{*0} \rho^0$  and  $Y_1^{*-} \rho^+$  suggests a possible peripheral production mechanism for the former. The C.M.S. angular distribution of the  $\rho^-$ , Fig. 7.3, shows that it is strongly peaked in the forward direction. The  $\rho^-$  density matrix elements have been found for the forward events from the  $\theta$  and  $\phi$  distributions, Fig. 7.4. The values obtained by maximum likelihood are,

$$\rho_{00} = 0.37 \pm 0.10 \quad \rho_{1-1} = 0.08 \pm 0.09 \quad \text{Re } \rho_{10} = -0.13 \pm 0.07$$

for the events with  $\cos \theta^*$  greater than 0.7 and mass ranges,  $\Lambda\pi^+ 1.36-1.40$  Gev,  $\pi^-\pi^0 0.66-0.86$  Gev.

The cross sections presented above show the same tendencies as those reported at 3.0 Gev/c<sup>45)</sup>. Not much else has been published for these states.

#### Multiparticle Final States.

The multineutral final states  $\Lambda\rho^{\pm} \pi^{\mp} \pi^0$  are expected to have quite large cross sections, as discussed in the last chapter. An upper limit of a few micro-barns can be placed on the cross sections for  $\Lambda\rho^{\pm} \pi^{\mp} \pi^+ \pi^-$ , as can be seen from the combined  $\pi^+ \pi^0$  and  $\pi^- \pi^0$  mass distributions of Fig. 7.5, for the  $\Lambda\pi^+ \pi^- \pi^+ \pi^- \pi^0$  events.

### 7.3 Charged $\rho$ Production in association with a $\Sigma$ Hyperon.

#### Two Body Reactions.

Fig. 7.6 shows the  $\pi^+\pi^0$  mass distributions for the  $\Sigma^+\pi^-\pi^0$  and  $\Sigma^-\pi^+\pi^0$  final states. The  $\rho$  resonance occurs in both cases, in channels which also show strong  $Y_0^*(1520)$  & (1405) production. Cross sections for the charged  $\rho$  production are presented below. The neutral  $\rho$  considered in the last chapter is included for comparison.

Resonance	Final State	Cross section ( $\mu\text{b}$ )
$\rho^-$	$\Sigma^+\pi^-\pi^0$	$152 \pm 20$
$\rho^0$	$\Sigma^0\pi^+\pi^-$	$55 \pm 19$
$\rho^+$	$\Sigma^-\pi^+\pi^0$	$42 \pm 11$

The momentum transfer scatter plots, Fig. 7.7, show the considerably more peripheral nature of the  $\rho^-$  (and to a certain extent  $\rho^0$ ) production as compared with the  $\rho^+$ . The cluster of events at low momentum transfer ( $\Delta^2 < 0.6$ ) were used to obtain the following set of density matrix elements describing the decay of the  $\rho^-$  (mass range 0.66-0.86 GeV),

$$\rho_{00} = 0.17 \pm 0.09, \quad \rho_{1-1} = 0.17 \pm 0.08, \quad \text{Re } \rho_{10} = 0.01 \pm 0.04$$

The  $\theta$  and  $\phi$  distributions are shown in Fig. 7.4.

These distributions, and the density matrix elements calculated from them, again seem indicative of mainly vector exchange.

#### Multiparticle Final States.

The  $\pi^+\pi^0$  mass distributions in the  $\Sigma^+\pi^-\pi^+\pi^-\pi^0$  reactions are presented in Fig. 7.8. No  $\Sigma^+\rho^+\pi^+\pi^-$ ,  $\Sigma^+\rho^+\pi^-\pi^-$  or  $\Sigma^-\rho^-\pi^+\pi^+$  production is observed.

#### 7.4 Production of the $\eta^0$ and $X^0$ Resonances.

##### $\eta^0$ Production.

The  $\eta^0$  is observed in three final states, as can be seen by consulting the  $\pi^+\pi^-\pi^0$  effective mass distributions already presented for the  $\omega^0$ . After allowing for the neutral decay modes (~70%) the following cross sections are obtained.

Reaction	Cross section ( $\mu\text{b}$ )
$\Lambda\eta^0$	$26_{\pm 11}$
$\Lambda\pi^+\pi^-\eta^0$	$51_{\pm 18}$
$\Sigma^+\pi^-\eta^0$	$100_{\pm 23}$

The C.M.S. angular distribution, Fig. 7.9, for the  $33\eta^0$ 's observed in the  $\Sigma\pi\eta$  state, shows considerable forward peaking. Too few  $\eta$ 's are observed in the other states for the

presentation of C.M.S. distributions to be useful.

### X<sup>0</sup> Production.

The X<sup>0</sup> has only been observed in association with the  $\Lambda$  hyperon. A search for evidence of X<sup>0</sup> production in other channels has been made, but no enhancements have been found. The  $5\pi$  effective mass distribution for the  $\Lambda\pi^+\pi^-\pi^+\pi^-\pi^0$  state, Fig. 7.10, shows the presence of two X<sup>0</sup>'s (both of which decay into  $\pi^+\pi^-\eta^0$ ). The 'missing mass to the  $\Lambda$ ' in the  $\Lambda$ -201 events (Fig. 7.11) indicates that there are  $21 \pm 5$  X<sup>0</sup>'s which decay into  $\pi^+\pi^-$  + neutrals of various types. Fig. 7.12 shows the same missing mass distribution for all multineutral  $\Lambda$ -201 events, defined as those events with an overall missing mass of more than  $2M_\pi$ . This shows, fairly convincingly, that there are  $16X^0$ 's with such a missing mass. In the table presented below the other  $5X^0$ 's are assumed to decay via the  $\pi^+\pi^-\gamma$  mode reported by Connolly et al.<sup>46)</sup> and Kalbfleisch et al.<sup>47)</sup>.

The missing mass for the 21 events was investigated further. Fig. 7.13 shows this mass distribution for all  $\Lambda$ -201 events in the X<sup>0</sup> region (0.94-0.98 Gev.). From this plot it is estimated that there are 12 neutral  $\eta$  decays present in the sample. The background either side of the

$X^0$  has been examined and does not show an  $\eta$  peak. Assuming that these  $12\eta^0$ 's all represent  $X^0$  decay products there are 4 events left unaccounted for. These events which also have a high missing mass are most likely of the  $\pi^0\pi^0\eta^0$  type where the  $\eta^0$  decays into  $\pi^+\pi^-\pi^0$ . The total  $X^0$  cross section is  $40 \pm 20 \mu\text{b}$  assuming a 25% decay rate into all neutrals.

Decay Mode	Rate (fraction)
$\pi^+\pi^-\eta_c$	$0.06 \pm 0.07$
$\pi^+\pi^-\eta_n$	$0.40 \pm 0.30$
$\pi^+\pi^-\gamma$	$0.16 \pm 0.16$
$\pi^+\pi^-$ - neutrals	$0.13 \pm 0.2$
neutrals	0.25

Within the very poor statistics these results are in agreement with those already published for the decay of an isoscalar  $J^{PG} = 0^{-+}$  meson. Most of the  $X^0$ 's are produced with a low momentum transfer ( $< 0.8 \text{ Gev}^2$ ).

#### 7.5 Other Zero Hypercharge Boson Resonance Production.

##### $A_2^-(1310)$ Production

As shown in chapter 6, there is good evidence for  $\Sigma^+ A_2^-$  production. The peak at  $1310 \text{ Mev}/c^2$  in the  $\pi^+\pi^-\pi^-$  effective mass plot, Fig. 7.13, for the  $\Sigma^+\pi^-\pi^+\pi^-$  channel gives

a cross section for  $\Sigma^+A_2^-$  of  $25 \pm 8 \mu\text{b}$ . The number of events in this peak is in good agreement with the number seen in the  $A_2$  band on the  $\Sigma\pi\rho$  Dalitz plot. These and other considerations show that the decay is entirely into  $\rho^0\pi^-$ .

No  $\Sigma^-A_2^+$  is seen, even though the C.M.S. production angular distribution for the  $A_2^-$  (Fig. 7.15) is consistent with a non-peripheral production mechanism. The  $\Sigma^0A_2^0$  state involves two unseen neutrals and cannot be measured. The statistics are too poor for any information concerning the production mechanism or spin of the  $A_2^-$  to be given. There is no evidence for the production of the  $A_1^-$  in the  $\Sigma^+\pi^-\pi^+\pi^-$  final state.

#### $f^0(1253)$ Production.

The  $\pi^+\pi^-$  effective mass for the  $\Lambda\pi^+\pi^-$  state presented on page 105 shows a slight enhancement in the high mass region. If this can be attributed to the  $f^0$  meson first seen by Selove and Hagopian<sup>48)</sup>, the cross section for  $\Lambda f^0$  production is about  $50 \pm 16 \mu\text{b}$ . The mass plot of Fig. 6.10a shows a small peak around 1.25 Gev, giving a cross section of  $15 \pm 4 \mu\text{b}$  for the  $\Sigma^+\pi^+f^0$  reaction.

#### Other Enhancements.

Returning to the effective mass plot of Fig. 7.12 for the  $\Lambda$ -201 multineutrals, it is to be noted that there

is a small deviation from background in the region of the  $B^0(1215)$  resonance first observed by Abolins et al (49).

The upper limit for possible  $B^0$  production is estimated to be about  $20\mu\text{b}$ . No  $B^{\pm}$  is seen in the states involving  $\omega^0\pi^{\pm}$  combinations.

Fig. 7.16 shows the combined  $KK\pi$  effective mass distribution for 15  $\Lambda KK\pi$  and  $\Sigma KK\pi$  final states observed in the present experiment. A slight enhancement ( $\sim 2$  standard deviations) is seen at about 1520 Mev. It is mainly associated with the  $\Lambda K^+K^-\pi^0$  events, which may be strongly contaminated.

The  $\pi^+\pi^+, \pi^-\pi^-,$  etc., distributions of Fig. 7.16<sup>7</sup> show no enhancements.

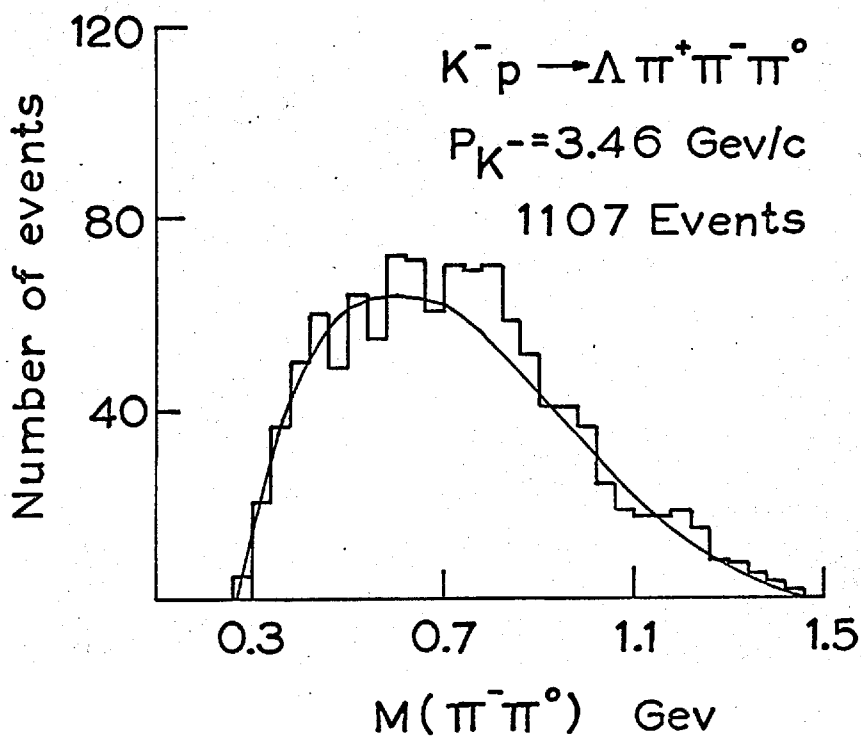
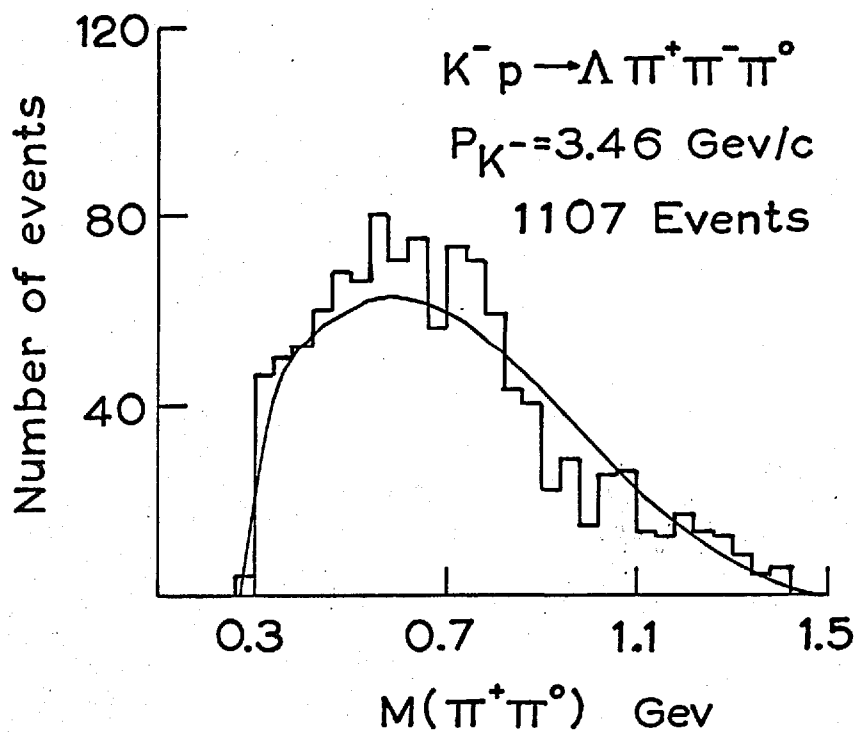


Fig. 7.1

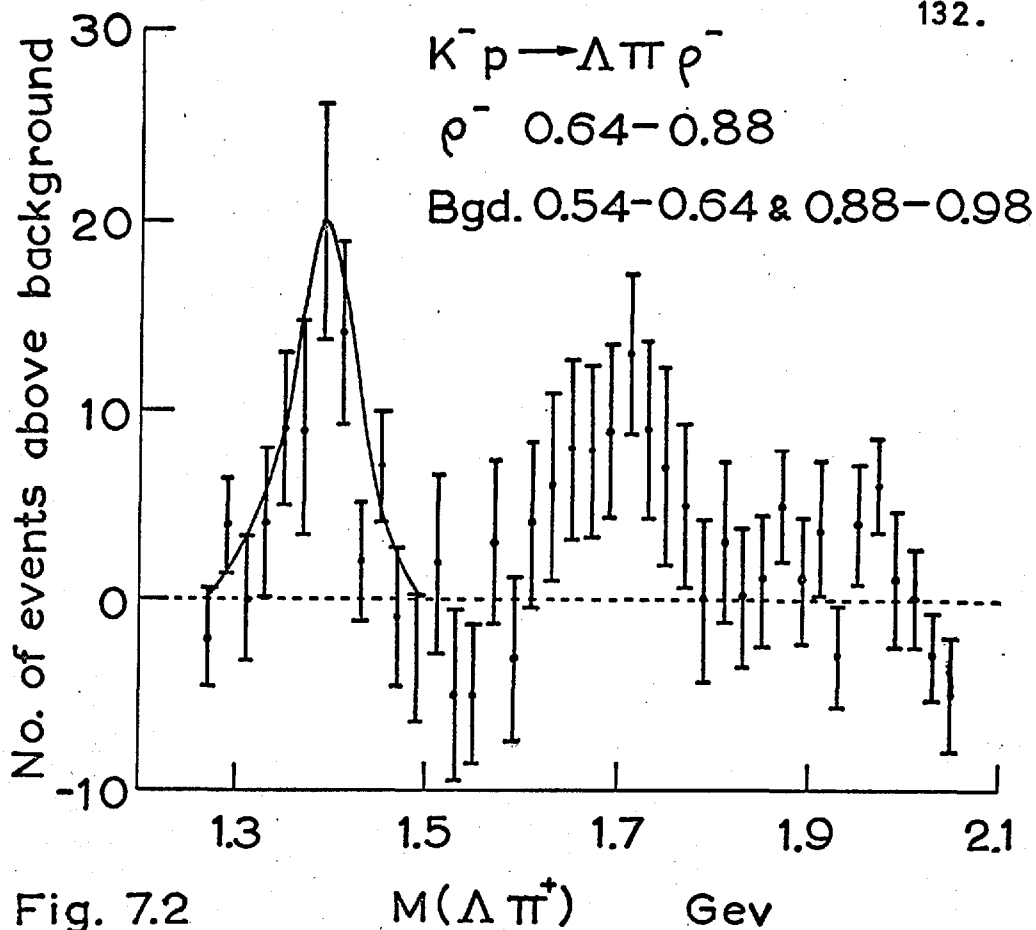


Fig. 7.2

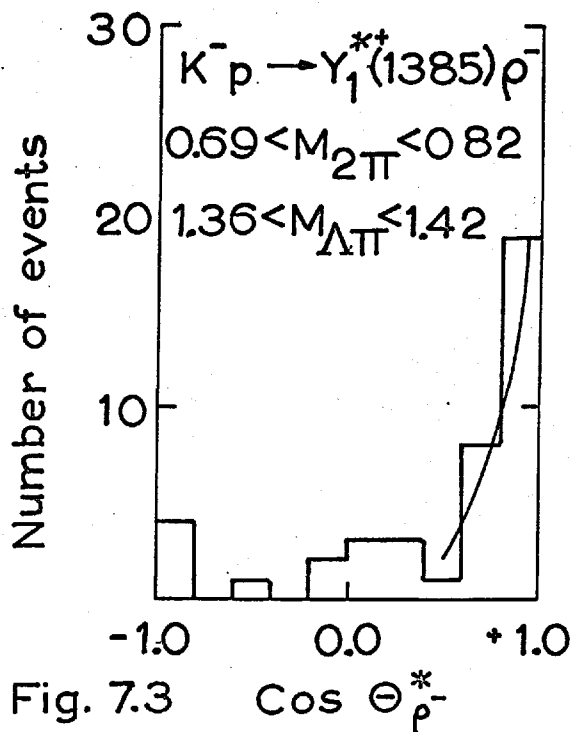


Fig. 7.3

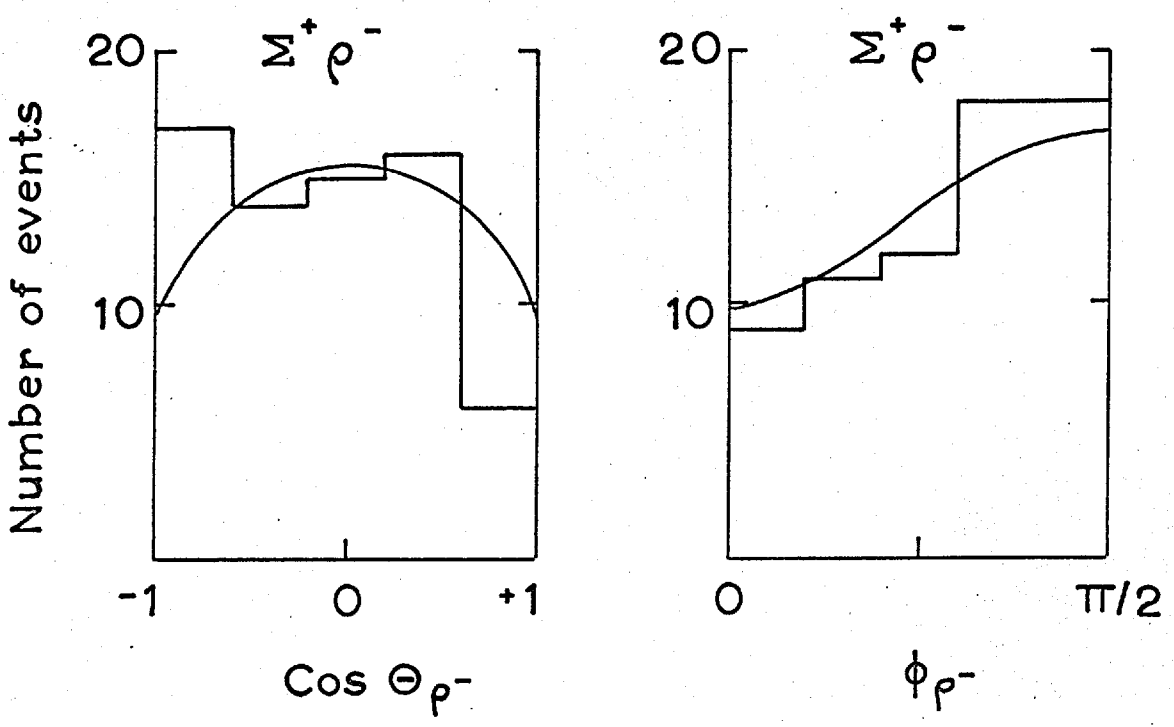
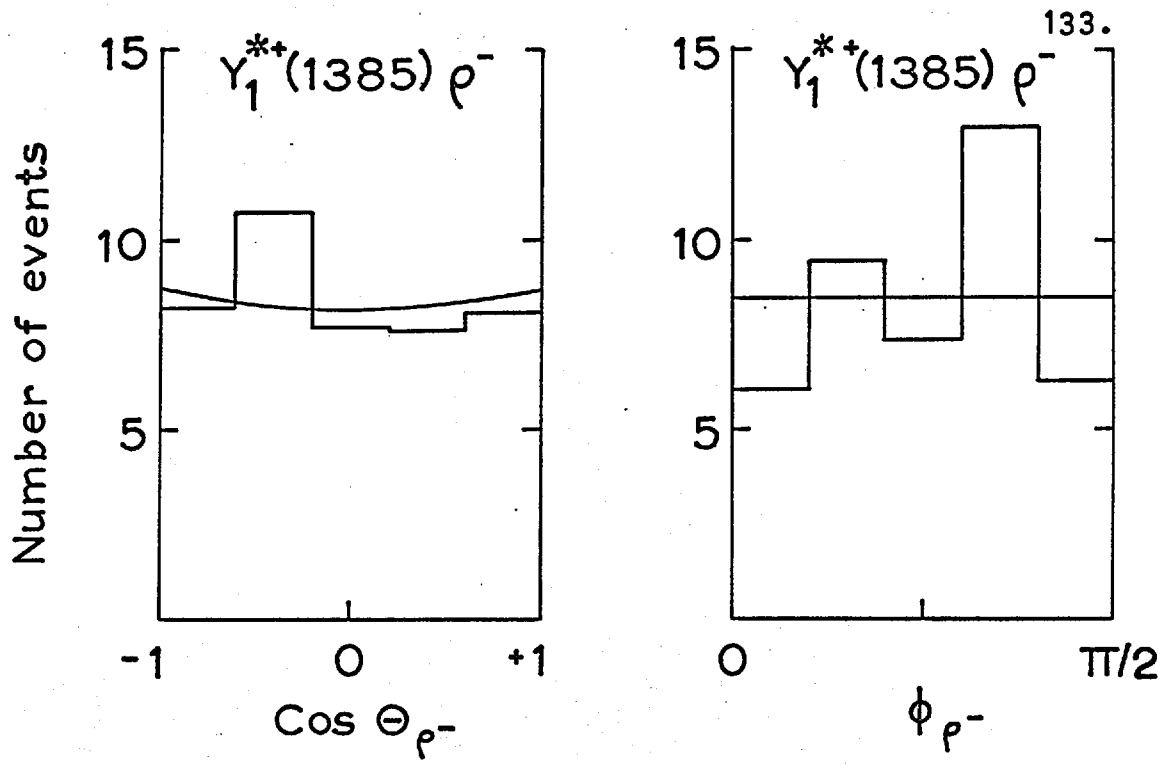


Fig. 7.4 Decay angular distributions

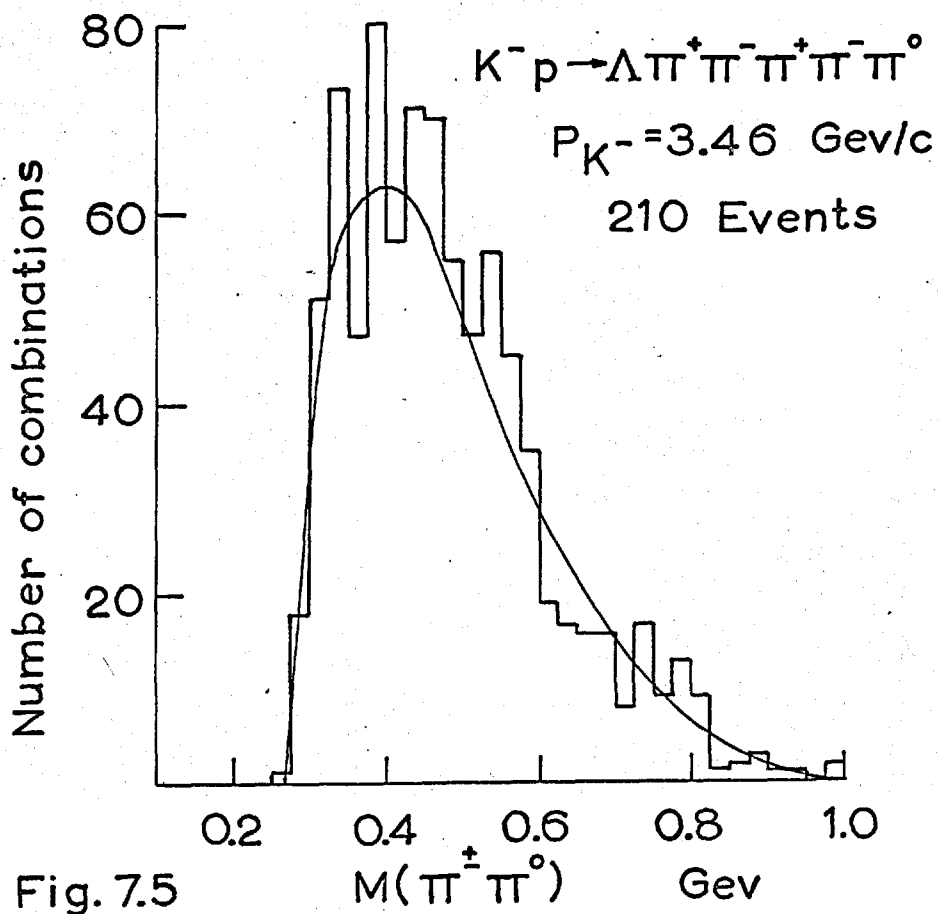
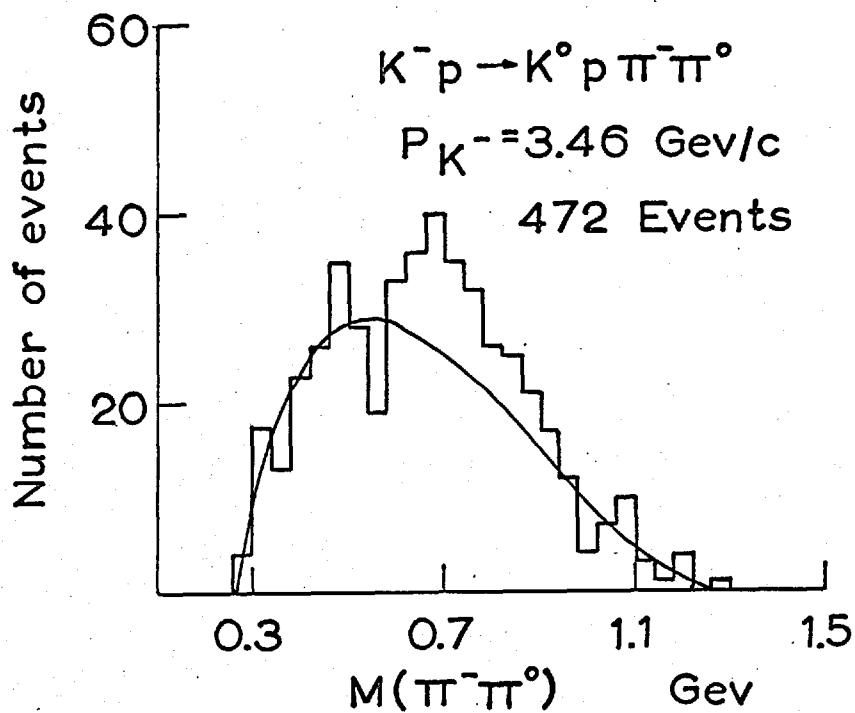


Fig. 7.5

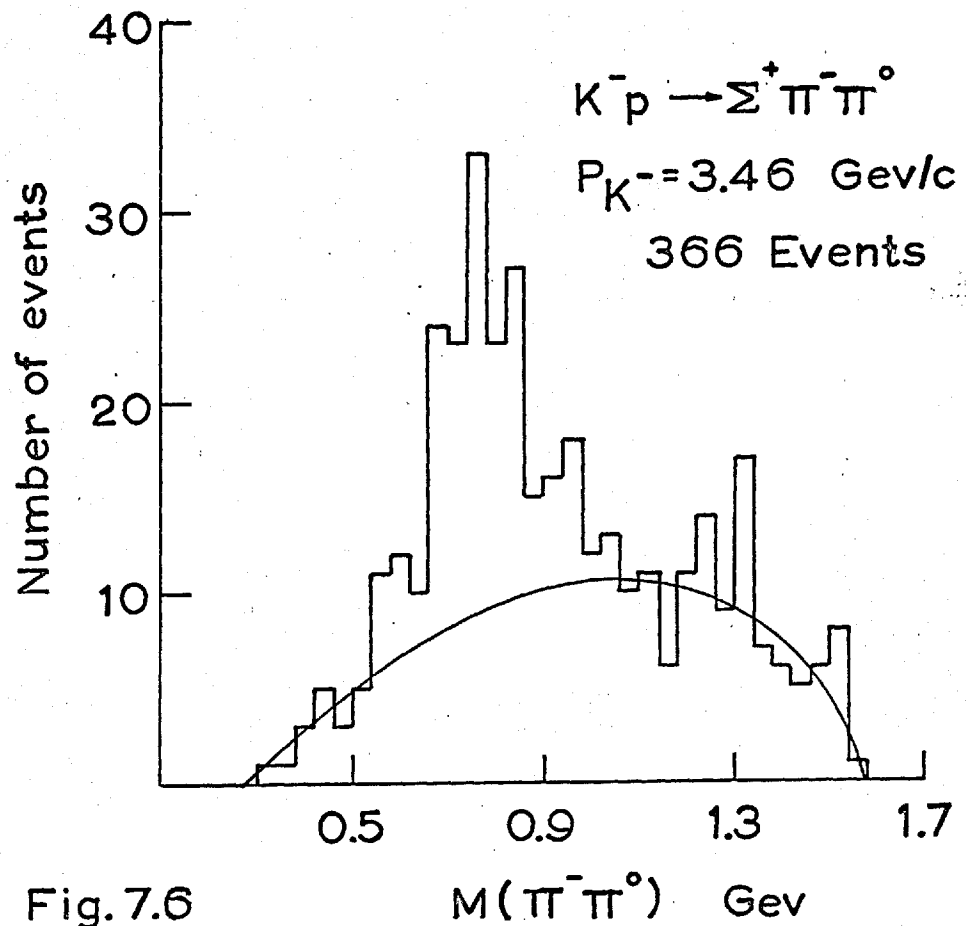
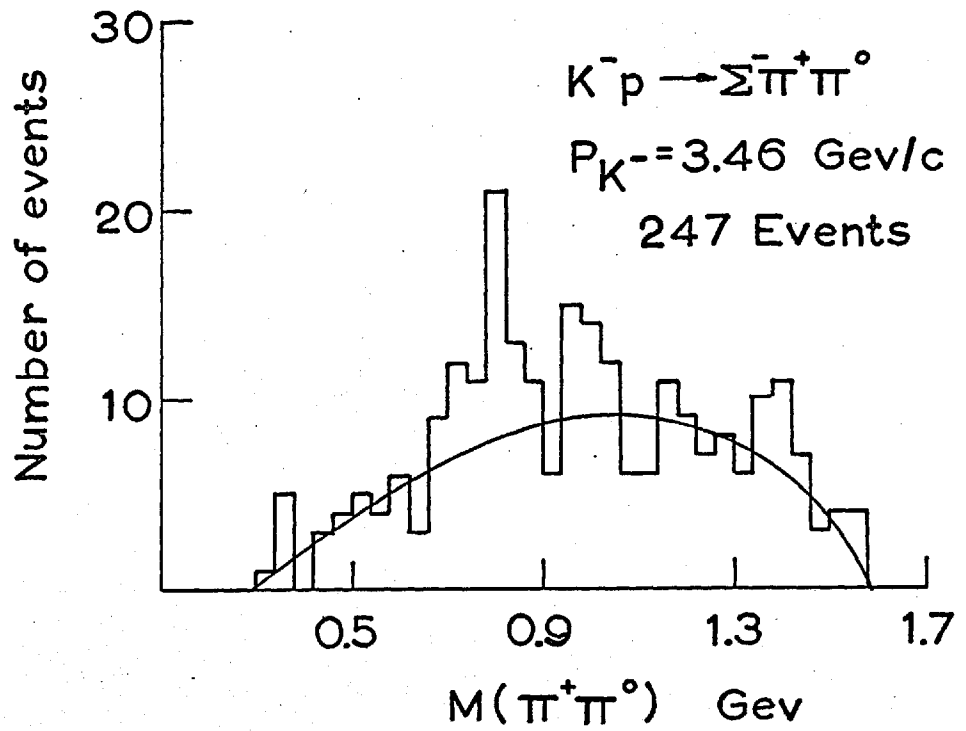


Fig. 7.6

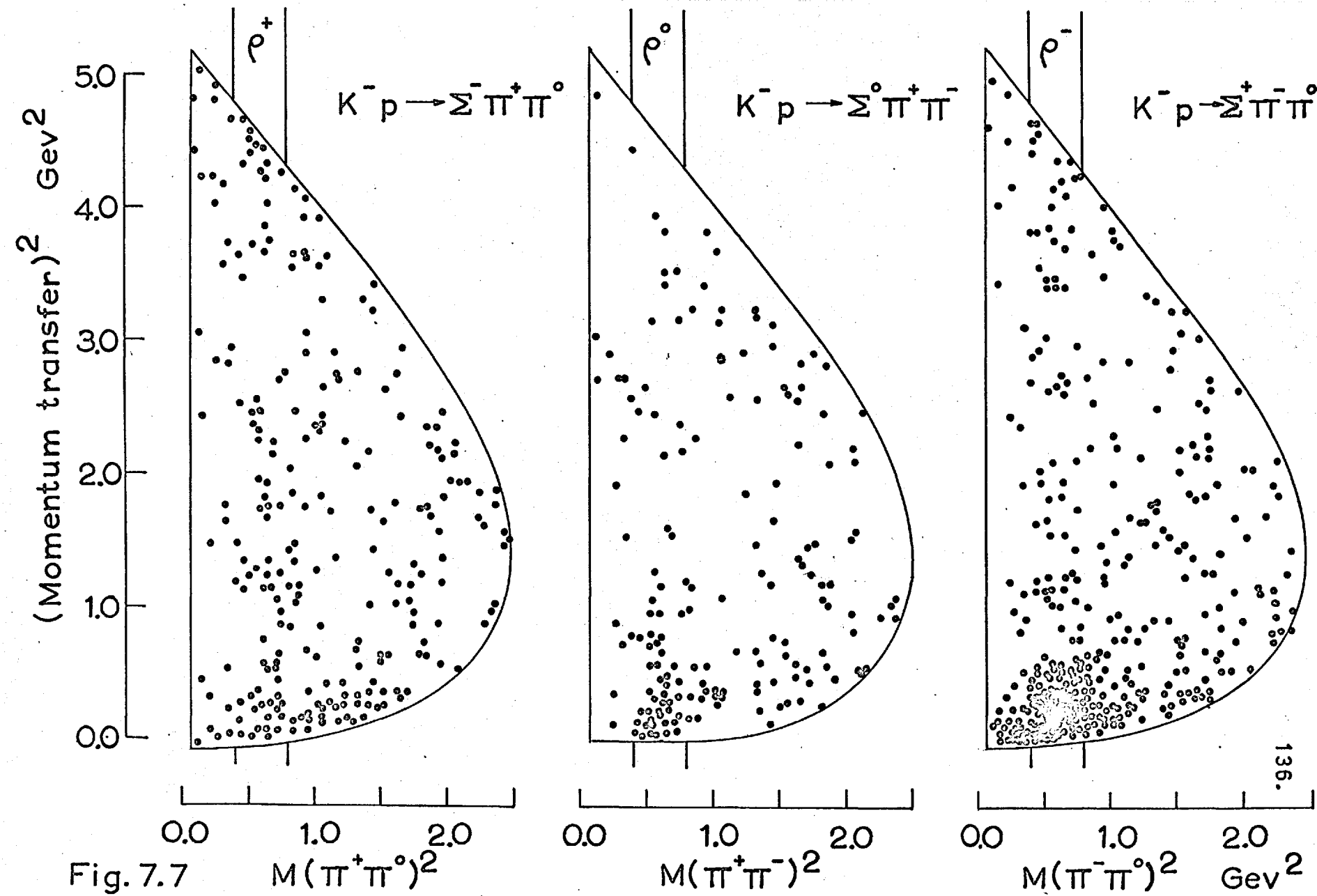
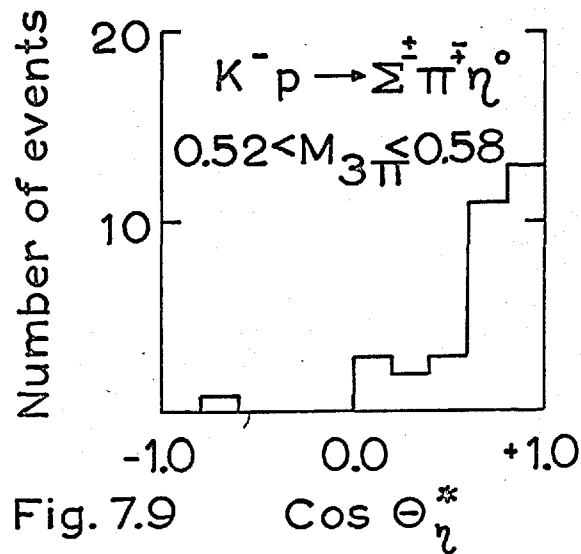
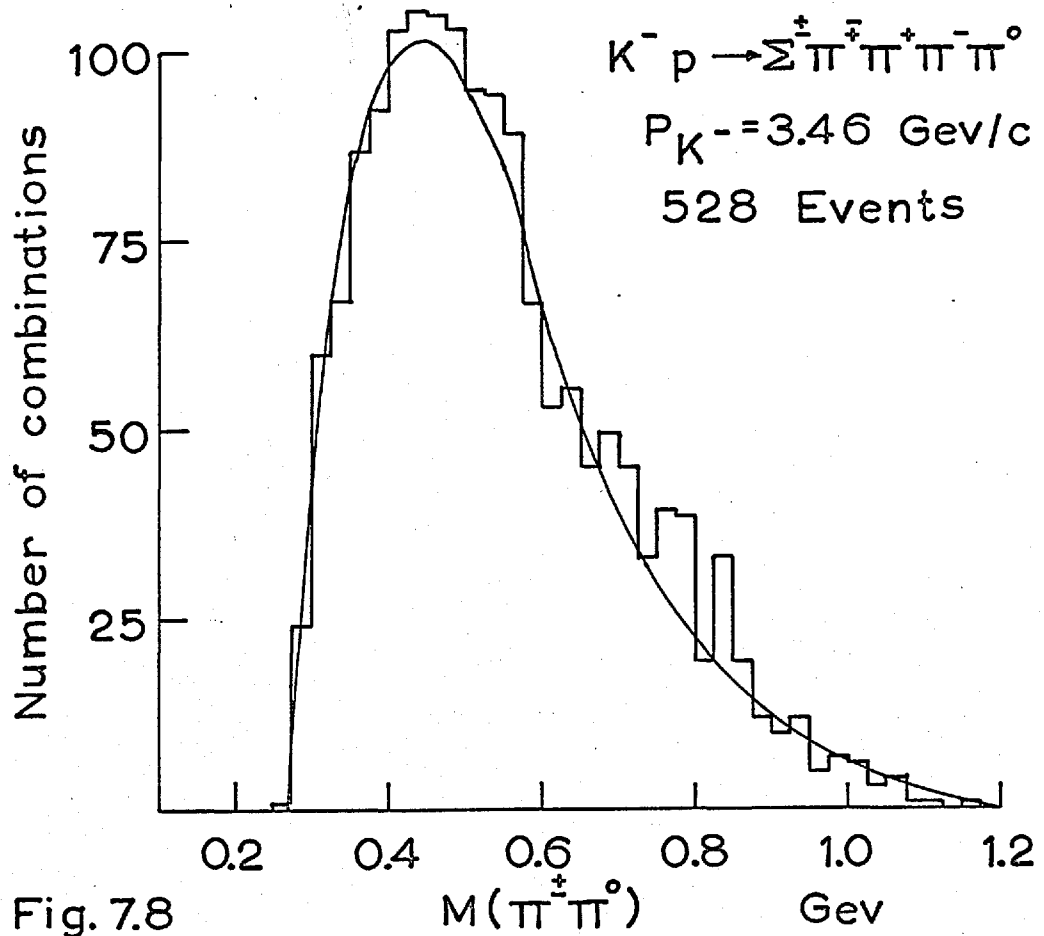


Fig. 7.7



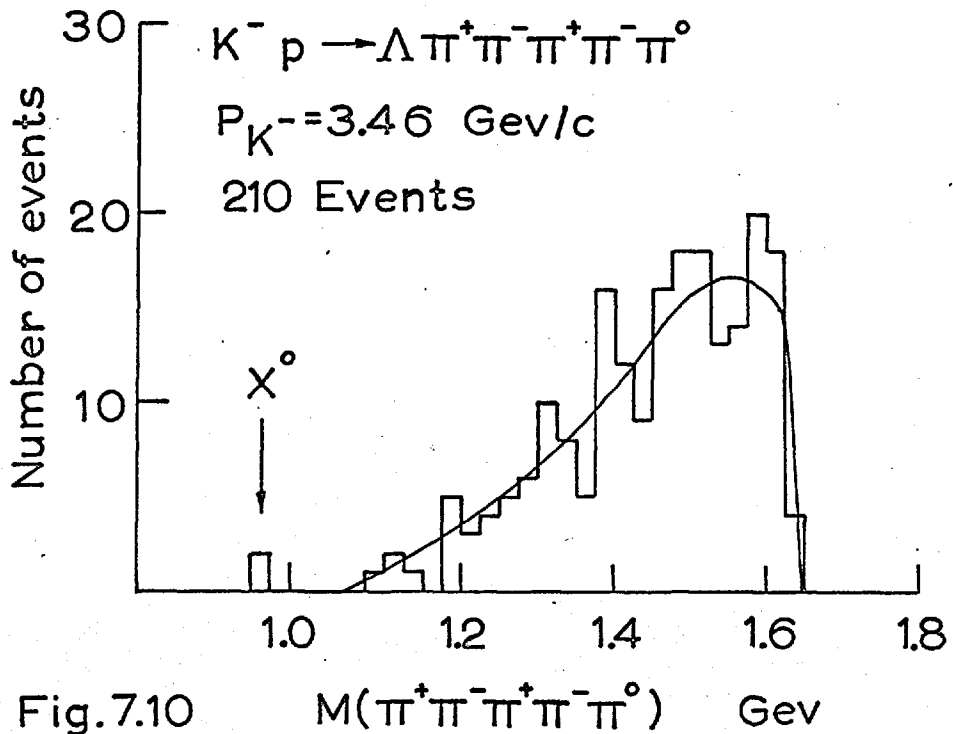


Fig.7.10

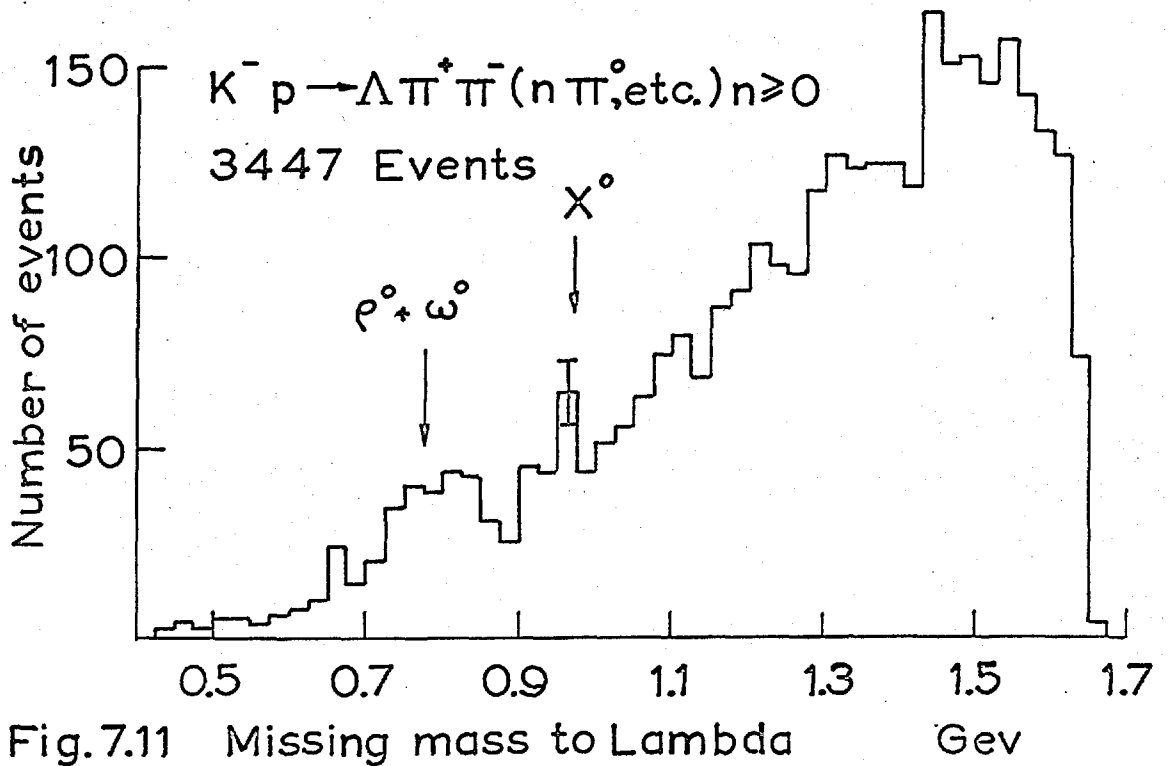
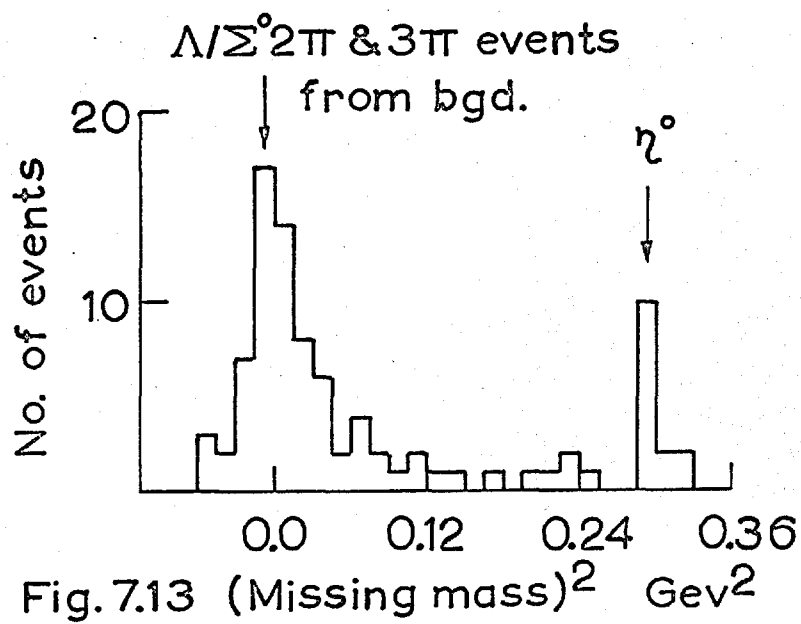
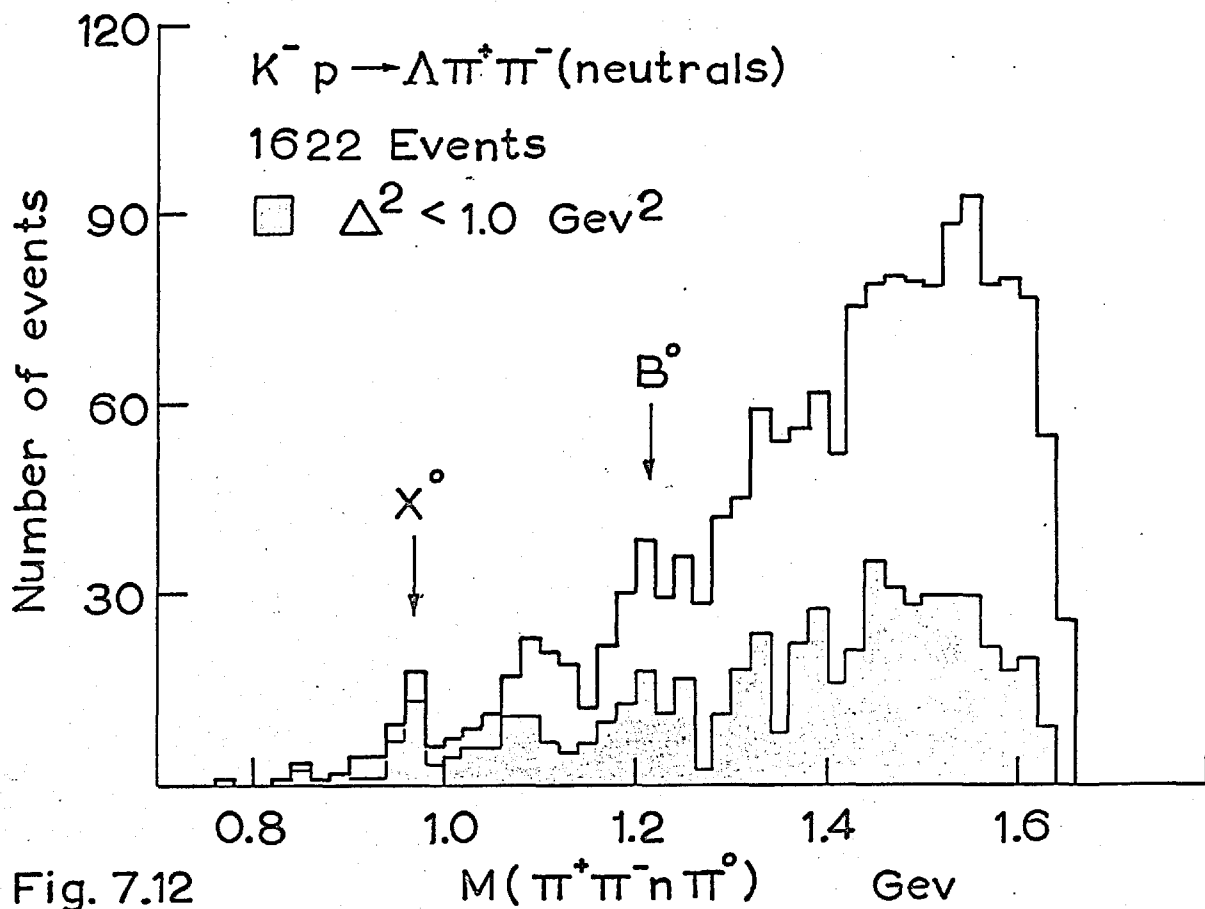


Fig.7.11



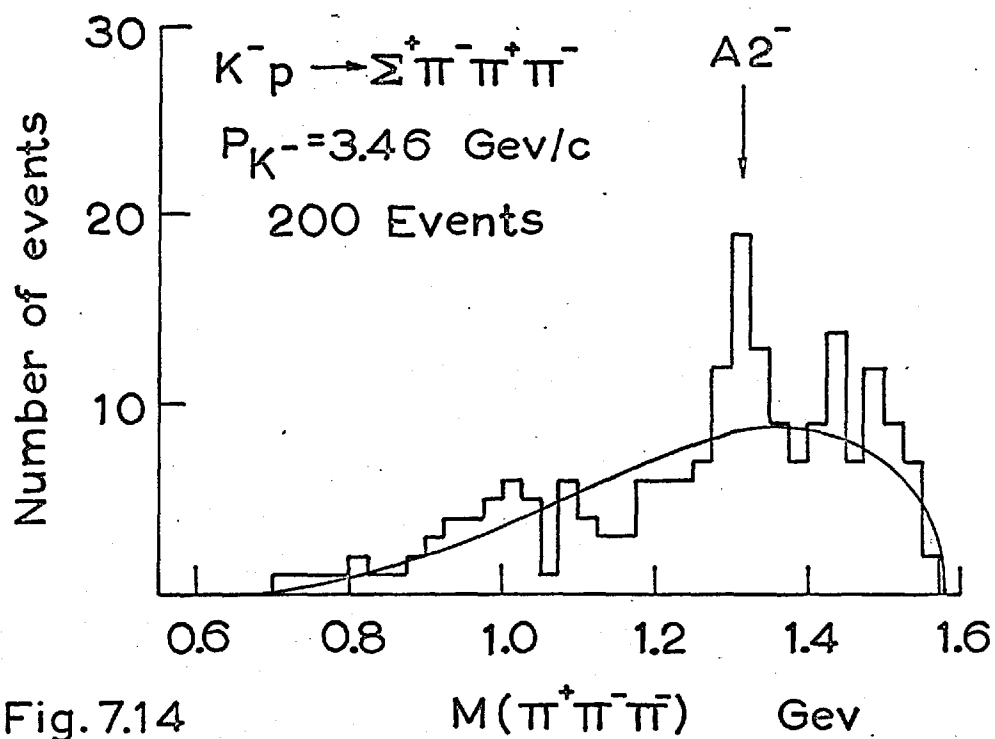


Fig. 7.14

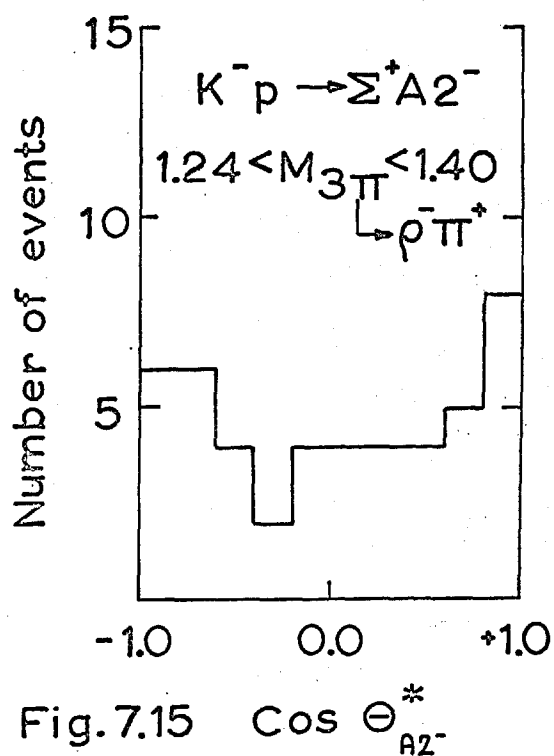


Fig. 7.15

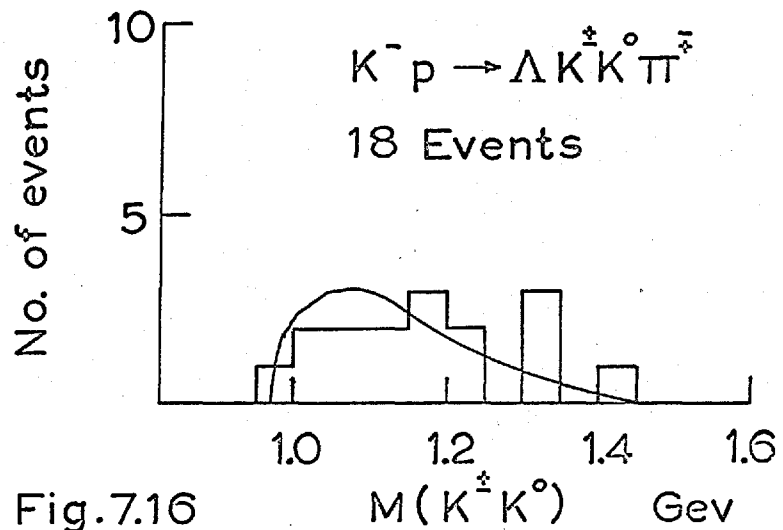
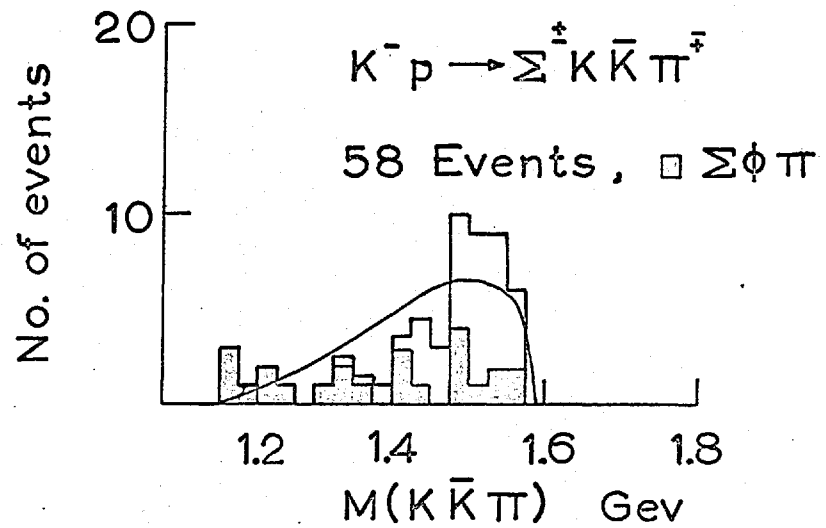
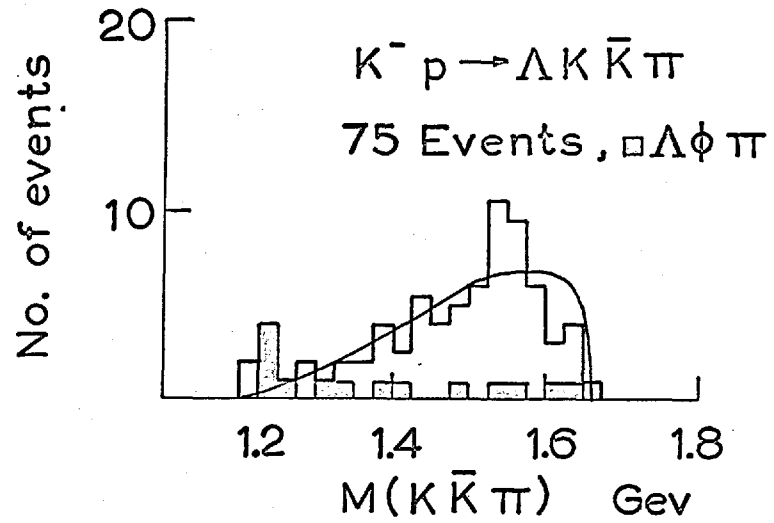


Fig.7.16

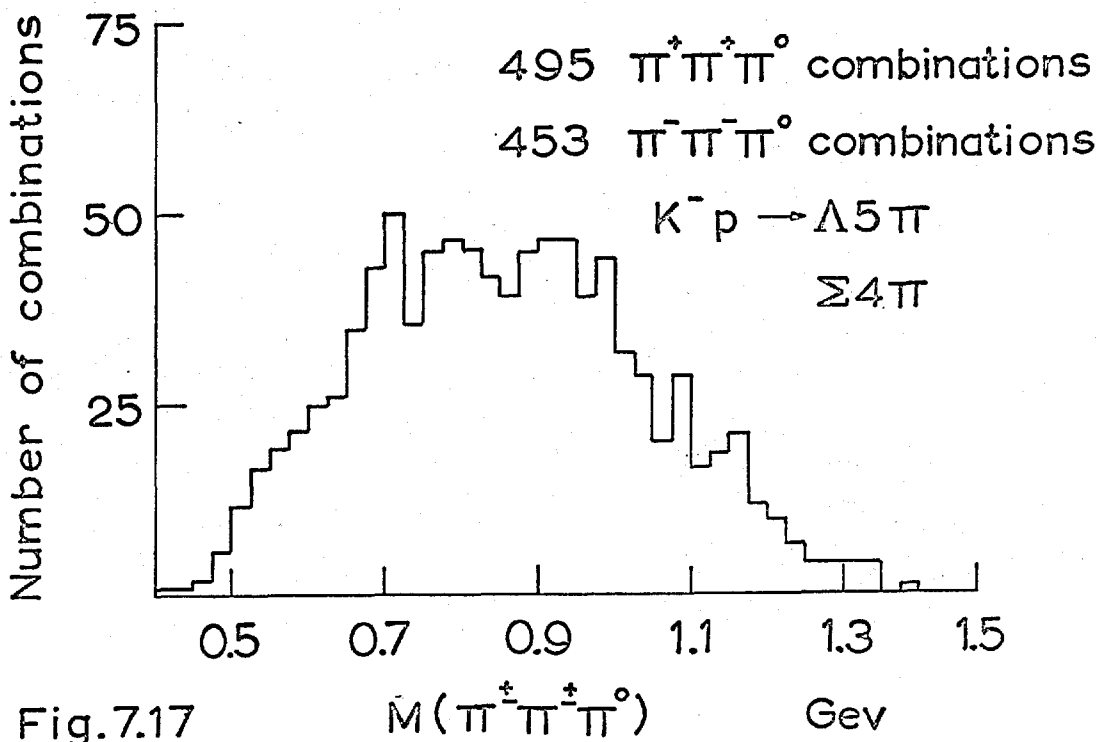
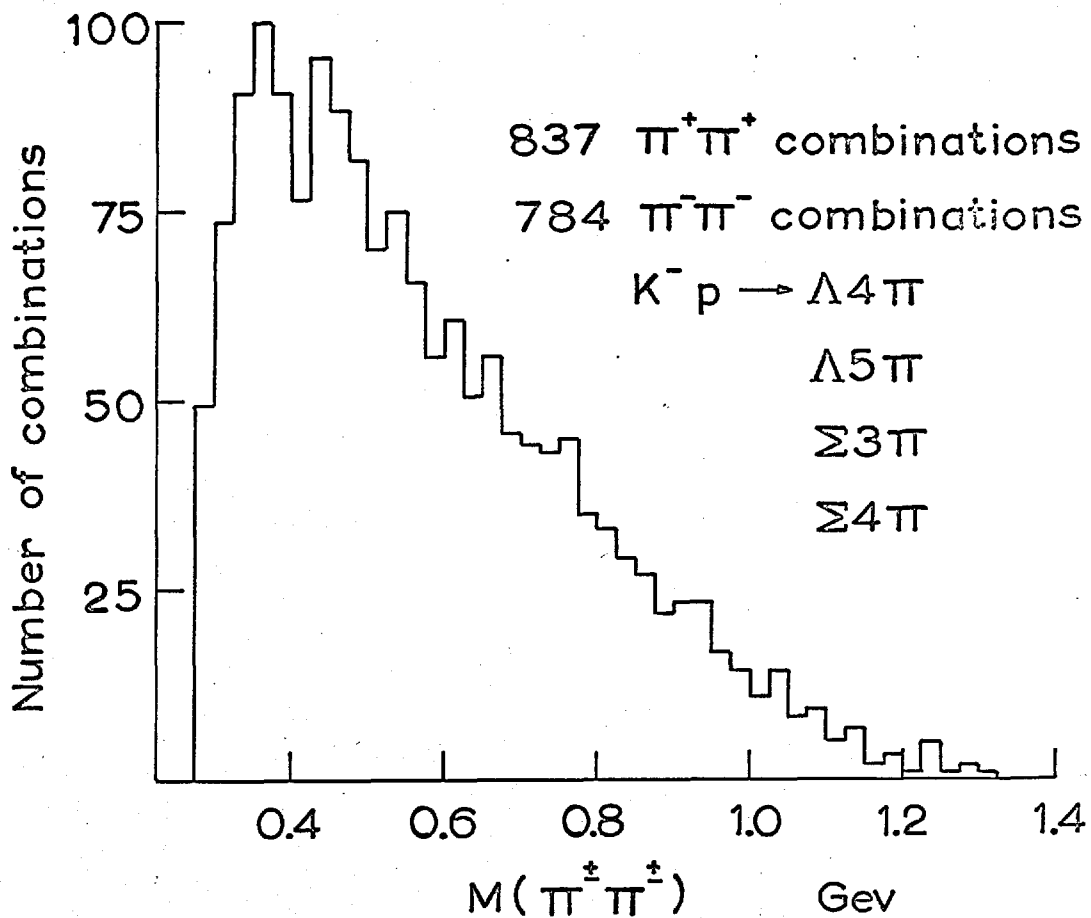


Fig.7.17

## CHAPTER 8

### SUMMARY AND COMPARISONS WITH THEORY

#### 8.1 Resonance Parameters.

The small cross sections for the production of boson resonances, other than  $K^*$ 's, in high energy  $K^-$  - proton interactions, preclude any detailed study of their intrinsic properties. For most of the non-strange boson resonances only a confirmation of the isotopic spin quantum number is possible.

Considering first the resonances for which least information is available from the present experiment, the  $\eta^0$ ,  $X^0$ ,  $f^0$  and  $A_2^-$ , all that can be said is that the first three are only seen in neutral states, in agreement with the  $I=0$  assignment, and the last is only seen in the negative state which certainly excludes  $I=0$ . Evidence from other sources now seems firmly in favour of  $I=1$  for the  $A_2$  meson. The  $G$ -parities of the  $f^0$  and  $A_2^-$  are obviously  $+1$  and  $-1$  respectively from the observed decays  $f^0 \rightarrow \pi^+\pi^-$  and  $A_2^- \rightarrow \rho^0\pi^-$ . From  $G=C(-1)^I$  the  $C$ -parities of the  $f^0$  and neutral  $A_2$  are both positive.

The  $\rho$  meson is observed in the positive, negative and neutral charge states. Since no evidence for  $\rho^{++}$  or

$\rho^{--}$  is found in the  $\pi^+\pi^+$  and  $\pi^-\pi^-$  mass distributions, the  $I=1$  assignment is highly favoured. The large observed widths are consistent with a strong decay into two pions, from which the G-parity is necessarily  $+1$  and the C-parity of the neutral state  $-1$ . An  $I=1$  two pion resonance must have odd  $J$  and negative parity. All that can be inferred about the spin is that, from the observed decay correlations,  $J=0$  is ruled out. Many groups have now shown that  $J=1$  is most likely, by studying these correlations in situations where the predominant production mechanism is pion exchange.

Less can be said about the  $\omega$  meson.  $I=0$  is consistent with the non-appearance of  $\omega^+$  and  $\omega^-$ . The width, though obviously small, is consistent with the rather poor experimental resolution in most channels. Assuming  $I$  and  $G$  are conserved in the decay (the first assumption is supported by the small,  $\sim 20\%$ , decay into all neutrals), then  $G=+1$  and  $C=-1$ . Nothing can be said concerning the spin, other than that  $J=0$  again seems to be ruled out by the decay angular distributions (cf. section 8.3).  $J^P = 1^-$  is now well established for the  $\omega^0$ , cf. Stevenson et al.<sup>50</sup>).

Finally, for the  $\phi$  meson strong support for the  $I=0$  assignment comes from the first observation of this resonance in the  $\Lambda K\bar{K}\pi$  and  $\Sigma K\bar{K}\pi$  final states. Strong  $\phi \rightarrow K_1^0 K_2^0$

and  $K^+K^-$  decays are observed in both cases. The  $K^+K^0$  effective mass distributions for the  $\Sigma^+K^+K^0$  and combined  $\Lambda K^+K^0\pi^+$  final states, Figs. 6.9 and 7.15, show no evidence for an enhancement around 1.02 Gev. Only a  $C=-1$  resonance can decay into  $K_1^0K_2^0$ . The  $G$ -parity is therefore negative from  $G=C(-1)^I$ . Since  $P$  and  $C$  are equivalent for the  $K^0\bar{K}^0$  system  $P=-1$  and the spin  $J$  is odd. The observed  $K_1^0K_2^0$ :  $(K_1^0K_2^0+K^+K^-)$  ratio is about 0.5 in all channels, this being the only evidence from the present experiment that the spin is unity. (cf. Connolly et al.<sup>51</sup>) and Schlein et al.<sup>52</sup>.)

The mean masses and widths observed in those channels most free of background are given in Table 6. Also included are the various quantum numbers. Those for which confirmatory evidence is available from the 3.5 Gev/c experiment are underlined.

## 8.2 Energy Dependence of Cross sections.

The cross sections for  $\Lambda\rho^0$ ,  $\Lambda\omega^0$  and  $\Lambda\phi^0$  are plotted as functions of the incoming  $K^-$  momentum in Fig. 8.1 and the  $\Lambda\eta^0$  and  $\Lambda X^0$  cross sections in Fig. 8.2. (Results taken from references 53 to 55.) Above 2.5 Gev/c all the cross sections fall fairly rapidly with increasing centre of mass energy and seem likely to be less than 10-20 $\mu$ b above 6.0 Gev/c.

Fig. 8.3 shows the manner in which the differential cross sections for the  $\Lambda\omega^0$  and  $\Lambda\phi^0$  states change as the  $K^-$  momentum increases from 2.24 to 3.5 Gev/c. The very different behaviour of these two cross sections is discussed in section 8.4.

### 8.3 The SU(3) Cross section Relationships.

#### i. Pseudoscalar Meson Production.

There are very few useful relationships for the two pseudoscalar resonances, the  $\eta^0$  and  $X^0$ . Nothing can be said about  $X^0$  production as there is no information available concerning the cross sections for its production in  $K^-n$  and  $\pi^-n$  interactions. The only equalities which result from SU(3) for the octet mesons are

$$\sigma(K^-p-\Sigma^-\pi^+) = \sigma(K^-p-E^0K^0)$$

$$\sigma(\pi^-p-\Sigma^-K^+) = \sigma(K^-n-E^-K^0)$$

Invariance under SU(3) provides several triangle inequalities in addition to those obtained from charge independence, none of which involve  $\eta^0$  production. To obtain relationships which can be verified easily it is necessary to make two assumptions: a) that single meson exchange dominates, b) that only the mesons belonging to the eight-dimensional representations need be considered in these exchange processes. Parity

conservation places an additional restriction on the nature of the exchanged meson, requiring that it belong to the vector meson octet only. In this approximation, the equality

$$\sigma(\pi^- p - \Lambda^0 K^0) = \frac{2}{3} \sigma(K^- p - \Lambda^0 \eta^0)$$

is expected to be obeyed to the same extent that the cross sections for  $\Sigma^- \pi^+$ ,  $\Xi^- K^+$  production in  $K^- p$  interactions, and  $\Sigma^- K^+$  production in  $\pi^- p$  interactions, are zero (exclusion of double charge exchange). The latter cross sections are all less than  $15 \mu\text{b}$  above  $3 \text{ Gev}/c$  but are certainly not zero. On the other hand the  $K^0 \Lambda^0$  and  $\eta^0 \Lambda^0$  cross sections are not much larger, being  $31^{+14} \mu\text{b}$  ( $3 \text{ Gev}/c$ ) and  $26^{+11} \mu\text{b}$  ( $3.5 \text{ Gev}/c$ ) respectively. Within the errors the equality is satisfied in the  $3-3.5 \text{ Gev}/c$  region.

#### ii Vector Meson Production.

Considering first the production of vector mesons in association with baryons belonging to the eight-dimensional representations, three triangle inequalities can be checked. The cross sections which are related via triangle inequalities, together with the experimental results at  $3-4 \text{ Gev}/c$  are as follows :

$$\begin{aligned} \sqrt{\sigma(K^- p - \Sigma^- \rho^+)} : \sqrt{\sigma(K^- p - \Xi^- K^{*+})} : \sqrt{\sigma(\pi^- p - \Sigma^- K^{*+})} \\ \Rightarrow \sqrt{(42^{+11})} : \sqrt{(8^{+2})} : \sqrt{(30^{+15})} \end{aligned}$$

$$\sqrt{\sigma(K^-p-\Sigma^+\rho^-)} : \sqrt{\sigma(K^-p-pK^{*-})} : \sqrt{\sigma(\pi^-p-p\rho^-)}$$

$$\Rightarrow \sqrt{(152 \pm 20)} : \sqrt{(790 \pm 50)} : \sqrt{(450 \pm 80)}$$

$$\sqrt{\sigma(K^-p-\Sigma^+\rho^-)} : \sqrt{4\sigma(K^-p-\Sigma^0\rho^0)} : \sqrt{\sigma(K^-p-\Sigma^-\rho^+)}$$

$$\Rightarrow \sqrt{(152 \pm 20)} : \sqrt{(220 \pm 76)} : \sqrt{(42 \pm 11)}$$

The last inequality is, of course, a direct consequence of charge independence. Although no allowance has been made for the different  $Q$  values (cf. Meshkov et al. <sup>10</sup>), all are observed to be obeyed. The only test that a triangle inequality really provides is that if one of the cross section involved is large, then at least one of the remaining two must also be large.

The assumption that vector and pseudoscalar meson exchange provide the main production mechanism requires that  $K^-p-\Sigma^-\rho^+$ ,  $\Sigma^-K^{*+}$ ,  $\Sigma^0K^{*0}$  and  $\pi^-p-\Sigma^-K^{*+}$  should all have zero cross section. Again, these reactions do not have zero cross section in the 3-4 Gev/c region, indicating that either mesons belonging to higher dimensional representations or baryons are being exchanged, or that the general approach is incorrect. The same assumption leads to

$$4\sigma(K^-p-\Sigma^0\rho^0) = \sigma(K^-p-\Sigma^+\rho^-),$$

which is satisfied within the errors. However, since the  $\Sigma^- \rho^+$  cross section is not exactly zero the single K or  $K^*$  exchange model cannot give a complete description of the  $\Sigma \rho$  production.

If the  $K^- p \rightarrow \Lambda \rho, \Lambda \omega$  and  $\Lambda \phi$  channels are dominated by K exchange the cross sections are related as follows <sup>14)</sup>:

$$\sigma(\Lambda \rho) : \sigma(\Lambda \omega) : \sigma(\Lambda \phi) = 1 : 3 \sin^2 \lambda : 3 \cos^2 \lambda$$

where  $\lambda$  is the  $\omega$ - $\phi$  mixing angle. From SU(6) we have  $\sin^2 \lambda = 1/3$  and  $\cos^2 \lambda = 2/3$ , and, even allowing for the different Q values of these reactions, the K- exchange hypothesis does not seem valid as  $\sigma(\Lambda \phi)$  is considerably smaller than either  $\sigma(\Lambda \rho)$  or  $\sigma(\Lambda \omega)$ . Apart from this there is slight evidence for vector exchange in the  $\rho$  and  $\omega$  channels from the Treiman-Yang angular distributions.

Similar remarks concerning the  $\rho, \omega$  and  $\phi$  production can be made for the  $Y_0^*(1405)$  and  $Y_0^*(1520)$  channels under the K- exchange hypothesis. In both cases the large cross sections for  $\rho$ -production seem to rule out this possibility, as is to be expected, since in these reactions a comparison is being made rather close to threshold.

When the vector meson - decuplet baryon resonance channels are examined under the hypothesis of SU(3) invariance, the

most important equalities obtained are the following,

$$\begin{aligned} \sigma(K^-p-Y_1^{*-}\rho^+) &= \sigma(K^-p-\Xi^{*-}K^{*+}) = \\ &= \sigma(\pi^-p-Y_1^{*-}K^{*+}) = \frac{1}{3} \sigma(\pi^-p-N_{3/2}^{*-}\rho^+). \end{aligned}$$

As has recently been emphasized by Meshkov<sup>56)</sup>, a study of these reactions is of particular interest, since the corresponding equalities involving pseudoscalar mesons are only obeyed in two pairs in the low energy region (<4 Gev/c). Unfortunately, it turns out that the first three reactions have cross sections which are consistent with zero on present statistics, and the fourth is a multineutral channel. In the same way, the one useful triangle inequality between  $\sigma(K^-p-Y_1^{*+}\rho^-)$ ,  $\sigma(K^-p-N_{3/2}^{*+}K^{*-})$  and  $\sigma(\pi^-p-N_{3/2}^{*+}\rho^-)$  cannot be checked as the third cross section is unmeasurable.

Charge independence relates the  $Y_1^*$  cross sections, but since the triangle inequality depends on a knowledge of  $4 \sigma(K^-p-Y_1^{*0}\rho^0)$ , and the error involved here (due to  $K^-p-Y_0^*(1405)\rho^0$  with  $Y_0^*-\Sigma^0\pi^0$ ) is very large, no useful comparison can be made.

The assumption of single meson exchange yields several additional relationships most of which do not appear to be very well satisfied below 4 Gev/c.

$$\text{e.g. } \sigma(K^+p-N_{3/2}^{*++}K^{*0}) = 3 \sigma(K^-p-Y_1^{*+}\rho^-).$$

#### 8.4 Exchange Mechanisms and the Absorption Model.

##### 1) The Backward $\omega$ peak.

A comparison of the differential cross sections for  $\omega$  and  $\phi$  production in the  $\Lambda\omega$  and  $\Lambda\phi$  channels indicates considerable differences in the production mechanisms for these two resonances. The most important difference in the C.M.S. production angular distributions is observed in the backward hemisphere where a strong peak is seen for the  $\omega$  but not for the  $\phi$ . If this peak can be attributed to a singularity in the scattering amplitude, the most interesting problem is to determine in which of the direct or crossed channels this singularity occurs.

The existence of a  $Y_0^*$  of mass 2.6 - 2.8 Gev could give rise to an angular distribution of the form exhibited by the  $\omega$ . Two questions arise if this is the true origin of the backward peak; why does the resonance not show up in other channels - particularly the  $\Lambda\phi$  channel, and is there any evidence from the total, elastic and charge exchange  $K^-$ -proton scattering cross sections for structure in the region of 3.5 Gev/c incident  $K^-$  momenta? The measurements of the elastic and charge exchange cross sections are rather poor in this region and no conclusions, one way or the other, can be drawn

from them. The total cross section, cf. W.F. Baker et al.<sup>57)</sup>, may show slight evidence for structure in the region 3.0 - 4.0 GeV/c. If the production of an intermediate  $Y_0^*$  is the cause of the backward  $\omega$  peak a further difficulty arises. In the C.M.S. the decay of the  $Y^*$  should be symmetric with respect to the plane perpendicular to the direction of the incoming kaon, unless there is interference with some other production process. The experimental distribution is almost symmetric at 3.5 GeV/c and would appear to indicate little if any  $\omega$  production via other mechanisms, in marked contrast to the  $\rho$  and  $\phi$  mesons.

The alternative solution to this problem, a singularity in the U channel, seems to provide a more reasonable explanation. The backward peak in the  $\omega$  distribution might be accounted for in terms of proton exchange in this channel, Fig. 1.2. Detailed tests of this hypothesis will have to await theoretical predictions for the decay correlations and far better statistics than are available from the present experiment. On the basis of this model smaller backward peaks are expected in the  $\rho$  distributions as well, but the background problem in the  $\Lambda/\Sigma\rho$  channels make any definite conclusions concerning such peaks rather difficult.

2) The Absorption Model.

Once the backward events have been subtracted, the total cross section for  $\omega$  production ( $\sim 50\mu\text{b}$ ) is much closer to the value expected, on the basis of SU(3), from the  $\phi$  cross section using the K-exchange hypothesis. If K-exchange is the only mechanism giving rise to the forward events the  $\theta$  distributions are expected to show cosine squared behaviour, or equivalently, the value of  $\rho_{00}$  in each case is expected to be unity. The experimental values,  $\rho_{00}(\omega) \approx 0.2$  and  $\rho_{00}(\phi) \approx 0.4$  would therefore appear to exclude this possibility. Furthermore, the C.M.S. differential cross sections, given by<sup>58)</sup>

$$\frac{d\sigma}{d\Delta^2} = \frac{\pi}{4m_v^2 m_p^2 P_{inc}^2} \frac{g^2}{4\pi} \frac{G^2}{4\pi} \times$$

$$\times \frac{[(m_p - m_\Lambda)^2 + \Delta^2] [(m_v - m_k)^2 + \Delta^2] [(m_v + m_k)^2 + \Delta^2]}{(m_k^2 + \Delta^2)^2}$$

are not peaked in the forward direction, cf. Fig. 8.4.

$m_p, m_\Lambda, m_v, m_k$  are the masses of the proton, lambda, vector meson and kaon,  $g$  and  $G$  are the coupling constants at the upper and lower vertices and  $P_{inc}$  is the incident kaon momentum in the laboratory.

Using the Goldhaber form factor<sup>65)</sup>,

$$F(\Delta^2) = \Lambda^2 - m^2 / \Lambda^2 + \Delta^2, \quad \text{with } \Lambda/m_\pi \sim 1.5$$

gives better agreement, but leaves unexplained the low values of  $\rho_{00}$ . This form factor is actually very unsatisfactory since the value of  $\Lambda$  necessary to obtain a reasonable fit is smaller than the kaon mass, and represents a singularity which is closer to the physical region than the pole due to the kaon propagator. The procedure of locating most of the  $\Delta^2$  dependence in the form factor has little if any physical significance.

A much better explanation of the strong forward peaking is provided by the absorption model of Gottfried and Jackson. Each partial wave in the expansion of the scattering amplitude is multiplied by two expressions of the form,

$$e^{2i\delta_j} = 1 - Ce^{-\gamma j^2}$$

where  $j$  is the total angular momentum, and  $C$  and  $\gamma$  are related to the constants characteristic of the diffraction scattering of the incoming or outgoing particles. For small values of  $j$  these expressions are also small ( $C \sim 1$ ), and serve to damp out the contributions from the low  $j$  partial waves. The values of  $C$  and  $\gamma$  which were used to obtain the absorption model curves of Fig. 8.4 for pure K-exchange were,

$$\begin{array}{ll} \text{incoming } K \text{ and } p & C_1 = 0.64 \quad \gamma_1 = 0.042 \\ \text{outgoing } \omega/\phi \text{ and } \Lambda & C_2 = 1.0 \quad \gamma_2 = 3/4\gamma_1 \end{array}$$

The  $\phi$  meson C.M.S. distribution is well fitted by the absorption model curve, whereas for the  $\omega$  meson the fit is not so satisfactory. The total cross sections obtained using  $g_{\Lambda KN}^2/4\pi = 4.4^{59}$ ,  $g_{\phi K\bar{K}}^2/4\pi = 1.5$  and  $g_{\omega K\bar{K}}^2/4\pi = 0.7$  are too low compared with experimental cross section obtained from the forward events.

Channel	$\sigma_{\text{forward}}$ (expt.)	$\sigma$ (abs. model) <sup>64)</sup>
$\Lambda \omega$	$50^{\pm 12}$	16.1
$\Lambda \phi$	$37^{\pm 10}$	29.8 $\mu\text{b.}$

The dependence of the  $\rho_{00}$  parameter on the momentum transfer ( $\Delta^2$ ) is shown in Fig. 8.5. The most important consequence of the high mass of the exchanged particle, when the absorption is taken into account, is the decrease in the value of  $\rho_{00}$  from the value unity expected for pure pseudo-scalar exchange. This parameter is also found to decrease as the mass of the produced vector meson decreases, being  $\sim 0.4$  at the  $\phi$  mass and  $\sim 0.2$  at the  $\omega$  mass. The predicted values of  $\rho_{1-1}$  and  $\text{Re } \rho_{10}$  are close to zero.

Fig. 8.5 shows the Treiman-Yang angular distributions

for the  $\omega$  and  $\phi$  events from the combined results of the 3.5 GeV/c and 3 GeV/c<sup>60)</sup> exposures. There is some evidence for structure in the  $\omega$  distribution which seems to indicate the presence of a small amount of vector exchange. Because of the uncertainties associated with the vector and tensor coupling constants for the  $\Lambda NK^*$  vertex no attempt was made to determine the precise amount of  $K^*$  exchange necessary to produce the observed distributions. However, the addition of vector exchange (assuming  $G_T = 0$ ) was found to result in the desired increases in both  $\rho_{1-1}$  and the total cross section .

We conclude therefore that the absorption model, on the basis of pure K-exchange, appears to provide a satisfactory account of the  $\phi\Lambda$  production, and with the addition of some  $K^*$  exchange the  $\omega\Lambda$  events produced in the forward direction can also be accounted for. K-exchange also provides satisfactory production angular distributions and decay correlations for the channel  $Y_1^{*+}(1385)\rho^-$ . The absorption model curve - normalized to the total cross section - is shown in Fig. 7.3. The coupling constant product necessary to give the correct cross section is

$$g_{\rho KK}^2 G_{Y_1^* NK}^2 / (4\pi)^2 = 0.5 \pm 0.2$$

### 8.5 Future Investigations.

Both the major theoretical contributions of recent years, the SU(3) symmetry scheme and the modified single meson exchange model, have only been tested thoroughly in  $K^+$ -proton and  $\pi^+$ -proton interactions. The restrictions imposed by charge and strangeness conservation, on reactions involving incident  $K^+$  or  $\pi^+$  mesons, severely limit the number of open channels, which, as a result, frequently have cross sections an order of magnitude larger than similar channels in  $K^-$  and  $\pi^-$  interactions. In  $K^-$ -proton interactions the only real tests of the single meson exchange model have been in the  $K^*(890)$ ,  $N_{3/2}^*(1238)$  and  $Y_1^{*+}(1385)$  channels where favourable conditions prevail as far as the exchanged mesons are concerned. In most of the channels where a mixture of K and  $K^*$  exchange is allowed, the decay angular distributions show little deviation from isotropy, and the statistics are frequently too poor for it to be certain whether the  $\Theta$  distribution shows more cosine squared than sine squared behaviour or vice versa.

There are many advantages of working in the 3-4 Gev/c region in  $K^-$ -proton interactions. Many channels show signs of being peripheral, and there is a strong possibility of being able to describe production processes in terms of a

small number of exchanged particles in crossed channels. Unitarity restricts any contributions from intermediate  $Y^*$ 's in the S channel, a fact which is reflected in the small size of humps in the elastic and charge exchange cross sections in the region above 2 Gev/c. Above 4 Gev/c many of the most interesting channels have cross sections which show signs of becoming vanishingly small.

A further  $K^-$ -proton exposure at 3.5 Gev/c would be extremely useful. A pure  $K^-$  beam providing 15 kaons/pulse directed into either the British National or Cern Hydrogen Bubble chambers would supply, in a matter of 100,000 photographs, as much information as has been obtained from the present experiment. A reasonable exposure, of say 1,000,000 photographs, would enable a much more detailed study of the  $K^*$  production to be made and would probably allow useful theoretical comparisons in the  $\rho$ ,  $\omega$  and  $\phi$  channels. Even on the basis of the very poor statistics available from the present exposure, the C.M.S. angular distributions show that there are basic differences in the production mechanisms in these channels.

TABLE 6

Resonance	Mass(Mev)	Width(Mev)	$I^C$	$J^{PG}$
$\eta^0$	$550 \pm 5$	$< 20$	$\underline{0}^+$	$0^{-+}$
$X^0$	$960 \pm 5$	$< 26$	$\underline{0}^+$	$0^{-+}$
$f^0$	$1250 \pm 30$	120	$\underline{0}^\pm$	$2^{++}$
A2	$1315 \pm 20$	100	$1^+$	$2^{+-}$
$\rho$	$760 \pm 20$	140	$\underline{1}^-$	$1^{--}$
$\omega^0$	$785 \pm 10$	$< 30$	$\underline{0}^-$	$1^{--}$
$\phi^0$	$1019 \pm 1$	$4 \pm 2$	$\underline{0}^-$	$1^{--}$

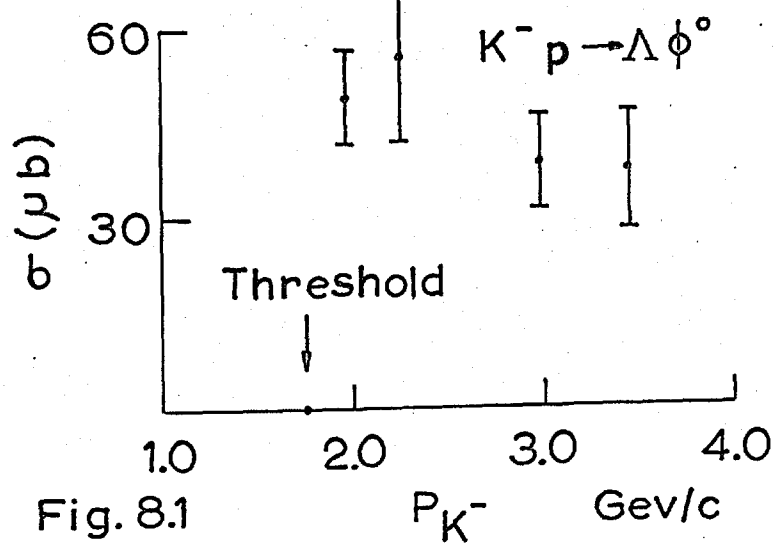
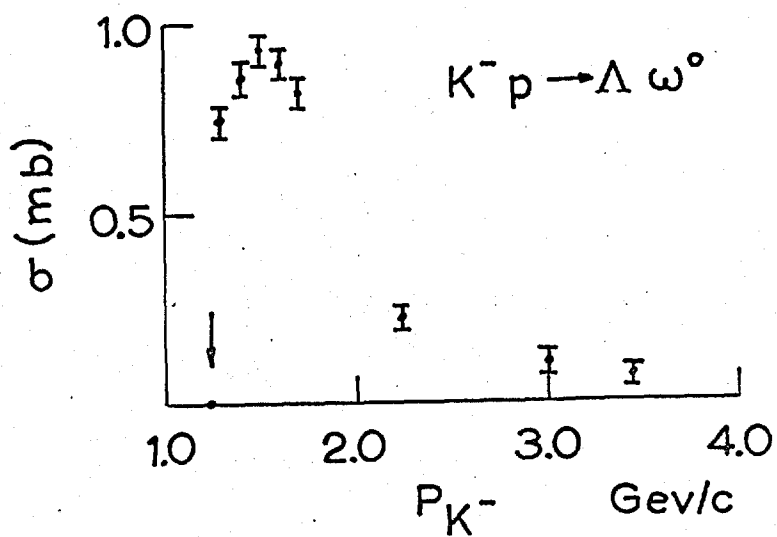
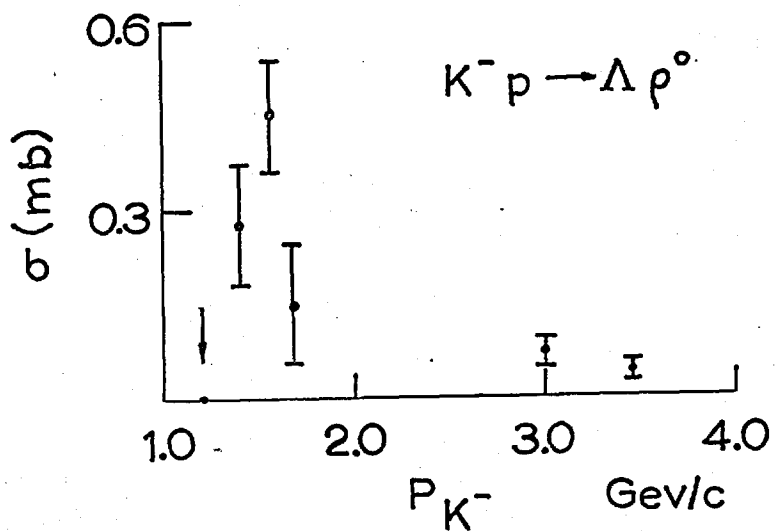


Fig. 8.1

 $P_{K^-}$  Gev/c

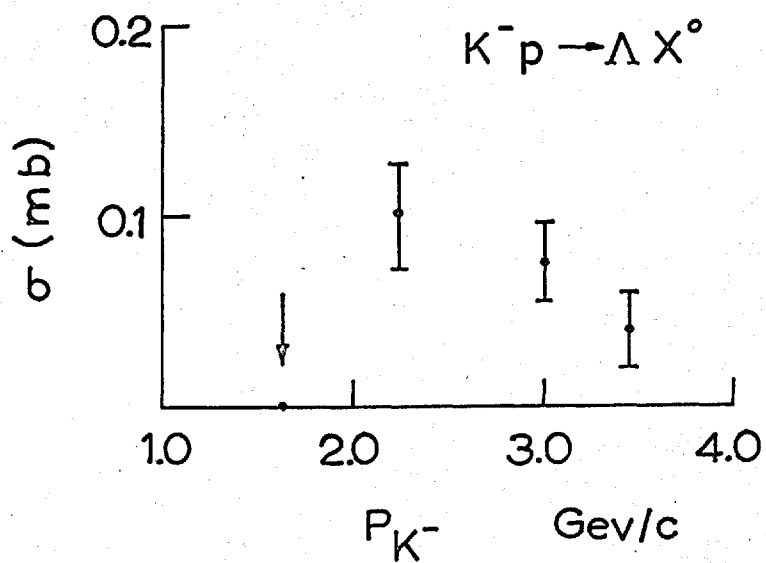
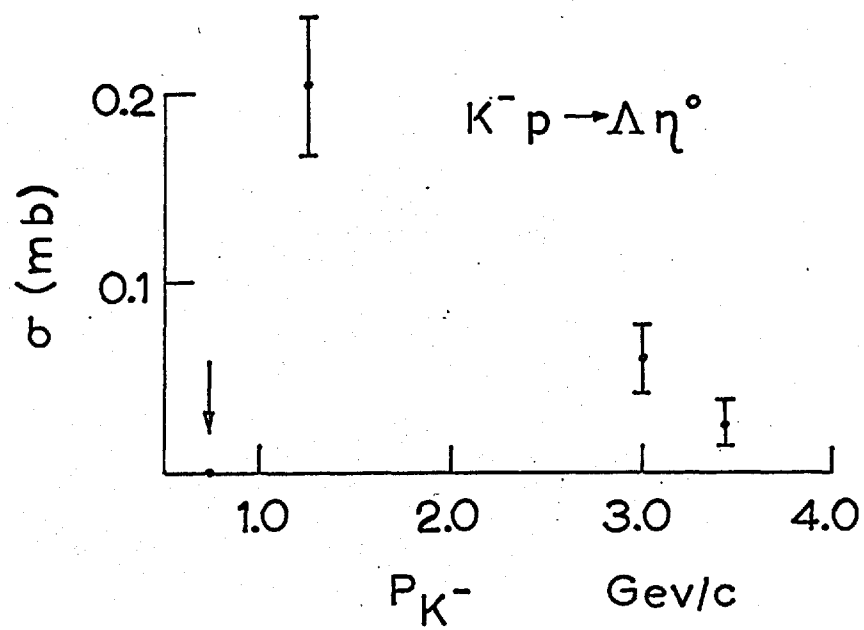


Fig. 8.2

$K^- p \rightarrow \Lambda \omega$  $K^- p \rightarrow \Lambda \phi$ 

162.

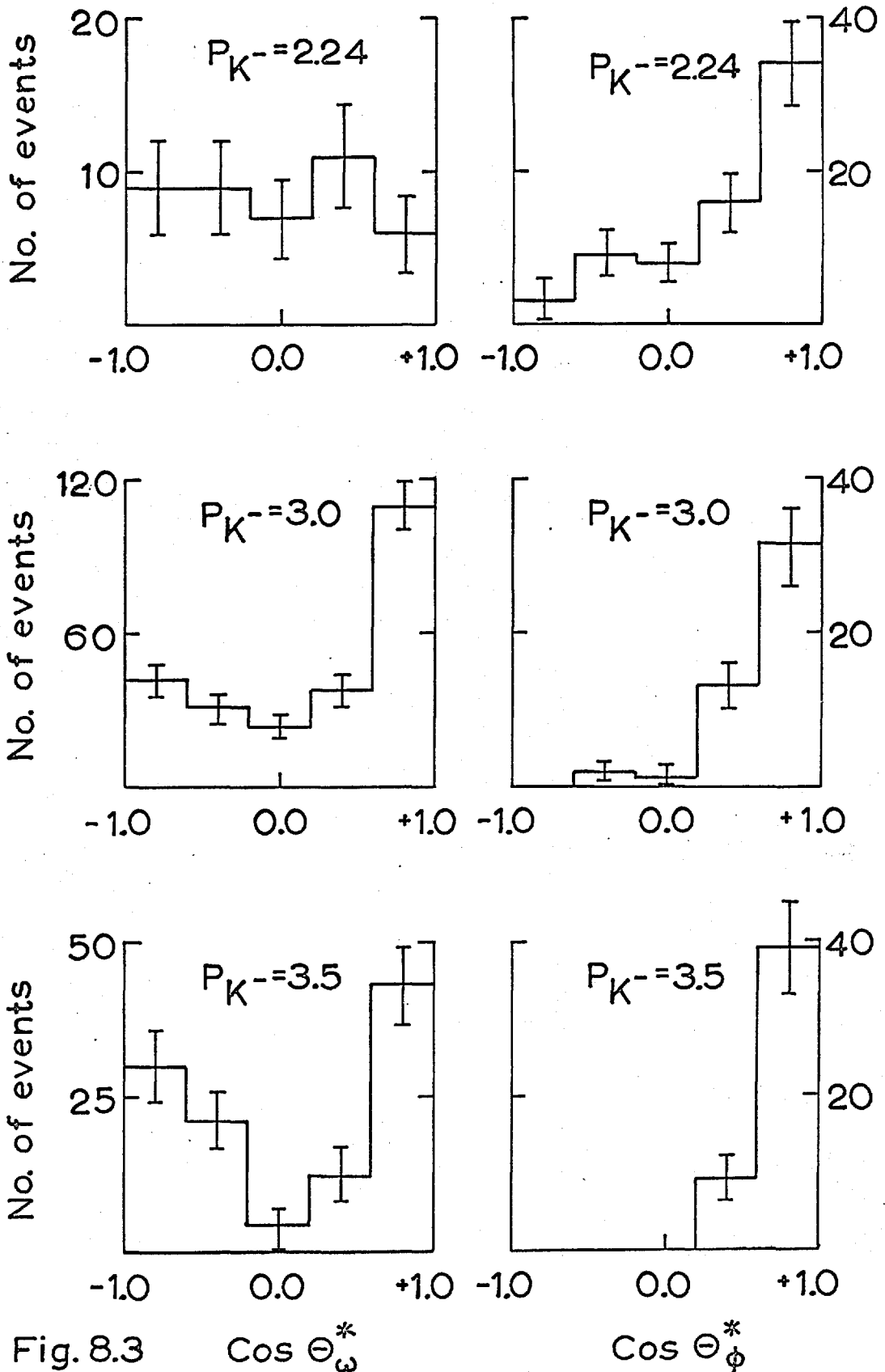


Fig. 8.3

 $\cos \Theta_{\omega}^*$  $\cos \Theta_{\phi}^*$

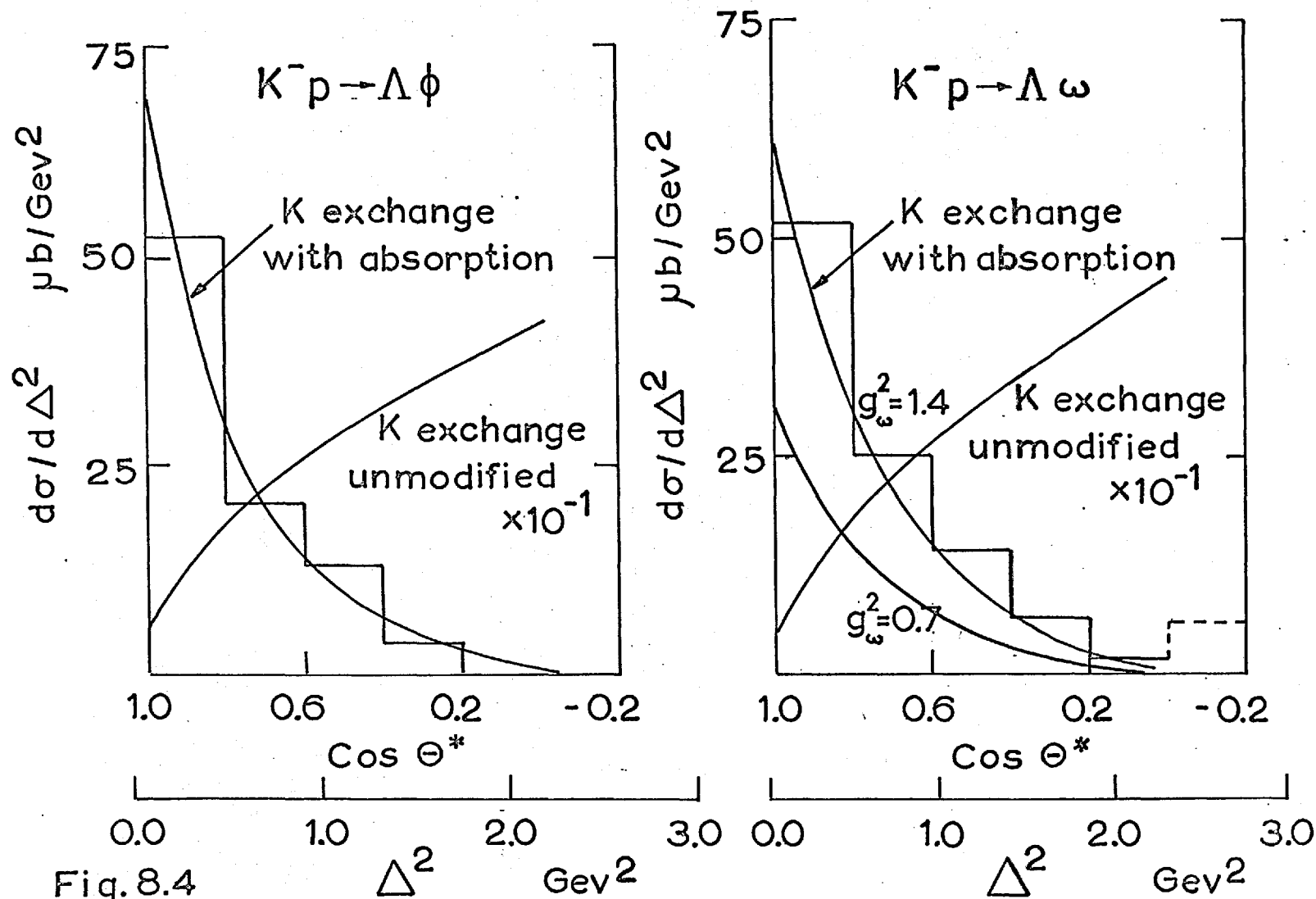


Fig. 8.4

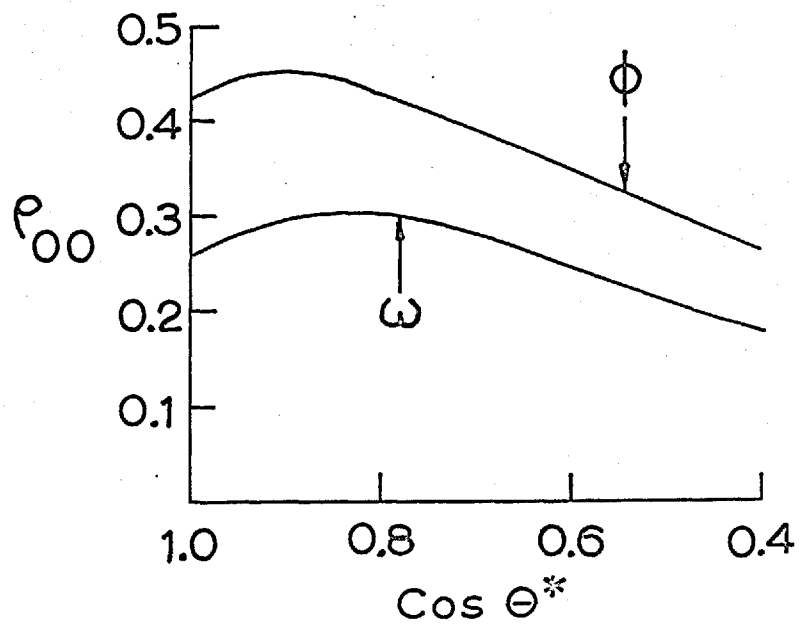
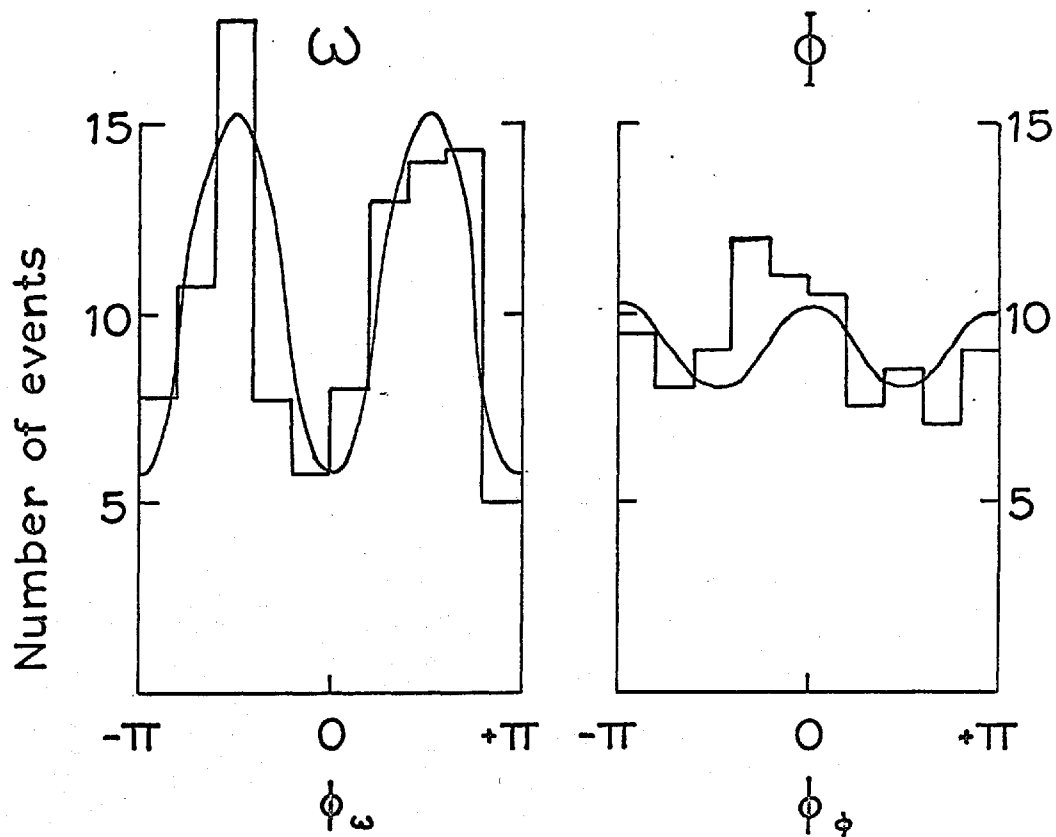


Fig. 8.5

Acknowledgements.

I wish to thank Professor C.C. Butler for the opportunity to carry out research as a member of the Imperial College High Energy Physics Group.

The invaluable guidance and assistance of my supervisor, Dr. I.O. Skillicorn, throughout all phases of the work, is most gratefully acknowledged. I thank my colleagues, especially A.A.Z. Ahmad, L.M. Celnikier and S. Misbahuddin, for providing a stimulating atmosphere for research through their frequent advice and encouragement. I would also like to thank Dr. J. Goldberg for interesting discussions during a brief but very pleasant visit to the Ecole Polytechnique, Paris.

The staffs of many laboratories have contributed in various ways to the present work. Most of the programming was the responsibility of the Rutherford High Energy Laboratory, Harwell. The computing facilities of the Deutches Rechenzentrum, Darmstadt were placed at our disposal, and did much to make the data analysis possible. I am grateful to Miss J. Nightingale, Mrs. M. Jane and Mrs. L. Yanadoss for their careful supervision of much of the scanning and book-keeping and to the technical staff in the group for their efficient maintenance of the measuring machines.

Finally, I should like to express my thanks to the D.S.I.R for the provision of a Research Studentship.

REFERENCES

1. M. Gell-Mann, Phys. Rev. 92, 833 (1953)
2. K. Nishijima, Progr. Theor. Phys. 13, 285 (1955)
3. P. Roman, Theory of Elementary Particles, North Holland (Publ.), 425 (1961)
4. S. Sakata, Progr. Theor. Phys. 16, 686 (1956)
5. M. Gell-Mann, California Institute of Technology Report, CTSL-20 (1961)
6. Y. Ne'eman, Nucl. Phys. 26, 222 (1961)
7. M. Gell-Mann, Phys. Letters 8, 214 (1964)
8. G. Zweig, CERN Report 8182/Th.401 (1964)
9. M. Gourdin, Ergebnisse der exakten Naturwissenschaften, 36 (1964)
10. S. Meshkov, G.A. Snow and G.B. Yodh, Phys. Rev. Letters 12, 87 (1964)
11. S. Okubo, Progr. Theor. Phys. 27, 949 (1962)
12. G. Zweig, International School of Physics "Ettore Majorana", Academic Press (Publ.), 192 (1964)
13. J.J. Sakurai, Phys. Rev. 132, 434 (1963)
14. H.J. Lipkin, Lie Groups for Pedestrians, North Holland (Publ.) 134 (1965)
15. K. Gottfried and J.D. Jackson, Nuovo Cimento 34, 735 (1964)
16. G.A. Smith et al., Phys. Rev. Letters 10, 138 (1963)
17. S.B. Treiman and C.N. Yang, Phys. Rev. Letters 8, 140 (1962)

18. J.D. Jackson, Nuovo Cimento 34, 1644 (1964)
19. K. Dietz and H. Pilkuhn, Nuovo Cimento 37, 1561 (1965)
20. F. Gürsey and L.A. Radicati, Phys. Rev. Letters 13, 173 (1964)
21. Les Chambres a Bulles au CERN, L'Onde Electrique, Dec. (1961)
22. S. van der Meer, CERN Yellow Report 60-22 (1960)
23. J. Goldberg, F. Muller and J.-M. Perreau, CERN/TC/HBC81 62/15 (1962)
24. J. Goldberg, CERN/TC/HBC81 62/6 (1962)
25. J.W. Burren and J. Sparrow, NIRL/R/14 (1963)
26. F.T. Solmitz, Helix fit to track images, Ecole Polytechnique, Dec. (1960)
27. F.T. Solmitz, UCRL Memo No. 220 (1960)
28. J. Badier, Theses, Université de Paris, Nov. (1964)
29. A.G. Wilson, NIRL/M/38 (1962)
30. A.G. Wilson, NIRL/R/42 (1963)
31. W.E. Humphrey et al., UCRL Memo No. 347 (1961)
32. O. Skjeggstad, CERN Yellow Report 64-13 (1964)
33. J. Orear, UCRL-8417 (1958)
34. F. Grard, UCRL-10153 (1962)
35. W.E. Humphrey, UCRL Memo P6 (1962)
36. K. Gottfried and J.D. Jackson, Nuovo Cimento 33, 309 (1964)

37. F.T. Solmitz, UCRL-11413 (1964)
38. S. Wojcicki and F.T. Solmitz, UCRL Memo No. 367 (1962)
39. J.G. Loken, Thesis, Oxford University (1964)
40. M. Goldhaber, T.D. Lee and C.N. Yang, Phys. Rev. 112, 1796 (1958)
41. G.A. Smith et al., Phys. Rev. Letters 13, 61 (1964)
42. A.A.Z. Ahmad, Thesis, London University (1965)
43. P.L. Connolly, Proc. Athens Topical Conf. on Recently Discovered Resonant Particles, 135 (1963)
44. S. Misbahuddin, Thesis, London University (1965)
45. E.S. Gelsema et al., Proc. Sienna Intern. Conf. on Elementary Particles, 134 (1963)
46. P.L. Connolly et al., Phys. Rev. Letters 13, 249 (1964)
47. G.R. Kalbfleisch et al., Phys. Rev. Letters 13, 349 (1964)
48. W. Selove et al., Phys. Rev. Letters 9, 272 (1962)
49. M. Abolins et al., Phys. Rev. Letters 11, 381 (1963)
50. M.L. Stevenson et al., Phys. Rev. 125, 2208 (1962)
51. P.L. Connolly et al., Phys. Rev. Letters 10, 371 (1963)
52. P. Schlein et al., Phys. Rev. Letters 10, 368 (1963)
53. M.L. Stevenson, Conf. on Particle Phys. Univ. of Colorado, Boulder (1964)
54. L. Bertanza et al., Proc. 1962 Intern. Conf. on High-Energy Phys., 284 (1962)

55. P.L. Connolly et al., Proc. Sienna Intern. Conf. on Elementary Particles, 130 (1963)
56. S. Meshkov, Coral Gables Conf. on Symmetry Principles at High Energy, Miami, Freeman (Publ.) 104 (1964)
57. W.F. Baker et al., Proc. Sienna Intern. Conf. on Elementary Particles, 634 (1963)
58. J.D. Jackson, Rev. Mod. Phys. 37, 484 (1965)
59. M. Rimpault, Proc. Sienna Intern. Conf. on Elementary Particles, 366 (1963)
60. J. Goldberg, private communication.
61. B. Sakita, Phys. Rev. Letters 13, 643 (1964)
62. E.P. Wigner, Phys. Rev. 51, 106 (1937)
63. A. Salam, R. Delbourgo and J. Strathdee, Proc. Roy. Soc. A284, 146 (1965)
64. R. Keyser, Programme for Absorption Model Calculations, CERN (1964)
65. G. Goldhaber, Proc. Athens Topical Conf. on Recently Discovered Elementary Particles, 80 (1963)